

Force-Detected, Single-Molecule Spectroscopy and Imaging Using
Nanoscale Mechanical Resonators

Thesis by

Bruce Michael Lambert

In Partial Fulfillment of the Requirements

for the Degree of

Doctor of Philosophy

California Institute of Technology

Pasadena, California

2005

(Defended April 28, 2005)

© 2005

Bruce Michael Lambert

All Rights Reserved

Abstract

Novel methods for spectroscopic probing of single-molecules are described that sense the optically induced, molecular dipole through the force/torque it generates on a submicron mechanical probe. The probe comprises a mechanical resonator with a high- Q mode of oscillation at frequency ν_h , to which is attached a nanoparticle with dipole moment \mathbf{p} . This dipole is either the optically induced dipole of a metal nanoparticle irradiated at plasmon resonance, or the static dipole moment of a ferroelectric nanocrystal. The electric force or torque between the probe dipole and molecular dipole drives the motion of the resonator at the resonance frequency. Three novel optical scattering mechanisms, which encode the mechanical motion into the phase, amplitude, or polarization of the light scattered by the resonator are investigated and quantified. A novel single-molecule sensor will also be described that comprises a mechanical torsional resonator with an attached ferroelectric nanoparticle. The observable quantity is the shift in the oscillation frequency of the mechanical resonator as a molecule becomes polarized by the rf near-field of the ferroelectric particle. The ferroelectric particle couples electrostatically to a nearby nanoscale capacitor which is used to electrically drive and detect the resonant mechanical motion. Due to this coupling, the electric and mechanical coordinates, which specify the state of this electromechanical device, are no longer the eigenmodes of the system. This gives rise to interesting dynamical effects that are best analyzed using the Lagrange formulation of mechanics. Finally, we discuss experimental progress toward fiber-optic interferometric detection of submicron mechanical resonators.

Table of Contents

Chapter 1. Introduction	1
Chapter 2. Engineering and Design Considerations for FDOS Experiments	19
Chapter 3. Optical Detection of Submicron Mechanical Resonators	44
Chapter 4. A Novel Nanoscale Device for Single-Molecule Sensing	64
Chapter 5. Experimental Apparatus	88
Conclusions	100
Appendix A. Derivation of Harmonic Oscillator Noise Spectral Densities from the Correlation Function	102
Appendix B. The Energy of a Polarizable Object in an External Electric Field	106
Appendix C. Ohmic Dissipation of the Induced Polarization Currents in the Electrodes of the Single-Molecule Binding Sensor Device	110

List of Figures

1.1 A typical single-molecule spectroscopy experiment	3
1.2 Single-Molecule, Force-Detected Optical Spectroscopy (FDOS)	4
1.3 A radio-frequency optical modulation technique for FDOS	9
1.4 A novel, single-molecule binding sensor	12
1.5 Block diagram of the apparatus used to excite and detect the single-molecule binding sensor	14
2.1 Resonator/probe geometry considered for FDOS experiments	27
2.2 Dielectric data for silver and gold plotted over the wavelength range from 400 nm–1600 nm	29
2.3 Plots of the aspect ratio and enhancement factor for optimized silver and gold ellipsoidal nanoparticles vs. wavelength	31
2.4 The relative enhancement factor of silver vs. gold for an optimized probe geometry	31
2.5 Plots of the excitation field and corresponding optical probe dipole that generate a 1°C rise in the temperature of the resonator	36
2.6 Force on the resonator and SNR for detecting a 0.1 debye molecular transition dipole	37
2.7 FDOS imaging of an InGaAs/GaAs quantum dot	38
2.8 EDDI imaging of a single dye molecule	40
3.1 Diagram of the fiber-optic interferometer for optical detection of submicron mechanical resonators	45
3.2 Encoding of translational mechanical motions via amplitude and/or phase modulation of the scattered light	48
3.3 Noise contributions for the phase-modulated optical detection scheme	55
3.4 Noise contributions for the amplitude-modulated optical detection scheme	56
3.5 Encoding of torsional mechanical motions via polarization modulation of the scattered light	57
3.6 Noise contributions for the polarization-modulated optical detection scheme	61
4.1 Electromechanical configuration of the single-molecule binding sensor	69
4.2 Geometry for a numerically simulated device	75
4.3 Plots of the electric current and torsional amplitude for the simulated device	77
4.4 Plots of the complex impedance for the simulated device	78
4.5 “T” matching network for efficient coupling of electric power to and from the device	79
4.6 “T” network for operation at 950.5 MHz	80
4.7 Power transfer efficiency of the “T” network to a 950.5 MHz device	82
4.8 Impedance matching to devices with resonance frequencies lying in a 30 MHz band centered at 950 MHz	84
5.1 Block diagram of the home-built fiber-optic interferometer apparatus	89
5.2 Circuit diagram of the constant-current source for the diode laser	92
5.3 Interference waveform as a function of d/λ	93
5.4 Interferometer locking circuit	94

5.5 Measured noise spectrum of the interferometer	96
5.6 Interferometric detection of a triple-paddle resonator	98
C.1 Simplified geometry of the binding sensor for estimation of polarization current losses in the electrodes	110

List of Tables

4.1 Compilation of the results of the numerical simulations for the binding sensor device	76
5.1 Characteristics of the Melles-Griot 13AMP005 transimpedance amplifier	91

Chapter 1. Introduction

In 1989 Moerner and Kador first demonstrated optically detected absorption spectroscopy of a single pentacene molecule embedded in a *p*-terphenyl host crystal cooled to 1.6 K.[1] In the time following this pioneering work, single-molecule spectroscopy has exploded into a field of intense research.[2] The crucial feature encompassing all single-molecule spectroscopy (SMS) experiments is that the *same* single molecule is spectroscopically monitored over the course of the experiment. Observation of the same molecule over the duration of the experiment allows one to infer the details of the instantaneous molecular configuration as well as the fluctuations in the local electronic environment of the molecule. These details of the state of the molecule and its local environment are encoded in the detected optical signal and cannot be revealed with conventional spectroscopic methods, which require measuring the response of an enormous number of nominally identical molecules in order to achieve an acceptable signal-to-noise ratio. Single-molecule spectroscopy experiments can therefore answer many fundamental scientific questions about the nature of the microscopic interactions between a molecule and its immediate host/solvent environment as well as detecting rare, short-lived molecular intermediates arising from chemical reactions and biochemical processes.[2]

The most sensitive optically detected single-molecule spectroscopy experiments count fluorescence photons emitted from an individual molecule. The highest signal-to-noise ratios for SMS experiments are obtained for dye molecules with high fluorescence quantum yields. In general, molecules will possess other relaxation pathways to the

ground state that do not produce fluorescence. These pathways compete with fluorescence and limit the number of photons counted in a time interval T . To understand how these pathways degrade the SNR for the single-molecule experiment we consider Figure 1.1, which shows a typical energy level diagram for a single molecule. In a typical experiment the molecule is excited from the ground state $|\phi_1\rangle$ to a higher lying state $|\phi_3\rangle$ by absorption of a single photon at wavelength $\lambda_{13} = \frac{c}{\nu_{13}}$. The molecule may then re-emit the same photon (dotted green arrow) or relax to the state $|\phi_2\rangle$. Once in the state $|\phi_2\rangle$, the molecule may reach the ground state by emitting a photon at wavelength $\lambda_{12} = \frac{c}{\nu_{12}}$, which is the spectroscopic signal of interest. This fluorescence process is represented by the straight red arrow in Figure 1.1. The molecule may also relax to the ground state by making multiple transitions within a manifold of vibrational states or by exciting phonons in the host. Both of these processes are represented by the purple squiggly arrow in Figure 1.1. These two mechanisms, however, may not be deleterious to the signal of interest, since fast relaxation to the ground state via these pathways will allow higher excitation laser powers before saturation is realized. Thus the photons lost to these mechanisms may be recovered by increasing the laser intensity at λ_{13} . Another more problematic mechanism is fast relaxation into a “dark” triplet state denoted by $|\phi_T\rangle$. For this situation the molecule makes a fast transition from $|\phi_2\rangle$ to $|\phi_T\rangle$, where it becomes “trapped”. This mechanism, termed intersystem crossing (ISC), effectively turns the molecule off to further photon absorption for a time equal to the lifetime of the triplet state, which may be much longer than any radiative lifetime. This presents a serious

limitation to the number of photons emitted by the single molecule at wavelength λ_{12} , in an observation time interval, T .

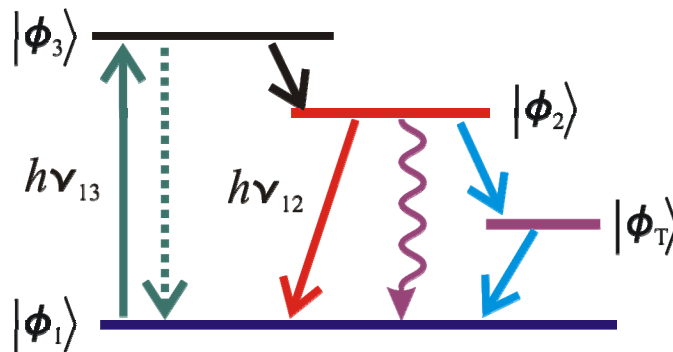


Figure 1.1: A typical single-molecule fluorescence experiment. A single molecule is resonantly excited by laser irradiation at frequency ν_{13} . Subsequently the molecule may re-emit a photon at the same frequency or make a transition to the lower lying excited state, $|\phi_2\rangle$. The molecule may then decay to the ground state, $|\phi_1\rangle$, by emitting a photon with frequency ν_{12} , which is the signal of interest. Alternatively, the molecule may reach the ground state through nonradiative decay mechanisms denoted by the squiggly arrow or may become trapped in a long-lived triplet state, $|\phi_T\rangle$.

How does intersystem crossing affect the signal-to-noise ratio for the single-molecule experiment? If we denote the rate of photon production in the presence of these various relaxation mechanisms as η , then the number of photons counted in the observation period T is ηT . Assuming Poisson statistics for the arrival time of the emitted photons, the dispersion in this number of counted photons is $\sqrt{\eta T}$, giving a signal-to-noise ratio of $\eta T / \sqrt{\eta T} = \sqrt{\eta T}$. Therefore the higher the photon production rate, the higher the single-molecule signal-to-noise ratio. Note that this is fundamentally the best that one can do for the single molecule photon counting experiment, since other noise sources originating in the photon detection and amplifier circuitry have not been included and will only further degrade the overall experimental SNR from this best value.

A goal of the methods described in this thesis is to beat this fundamental limitation on SNR, which arises from the observable being the radiation emitted by the

molecular transition. The novel methods described probe the molecule instead by sensing the force/torque that the optically induced molecular dipole produces on a nanoscale mechanical resonator. These methods will be quantitatively explored in this thesis and come under the collective name, Force-Detected Optical Spectroscopy (FDOS).[3]

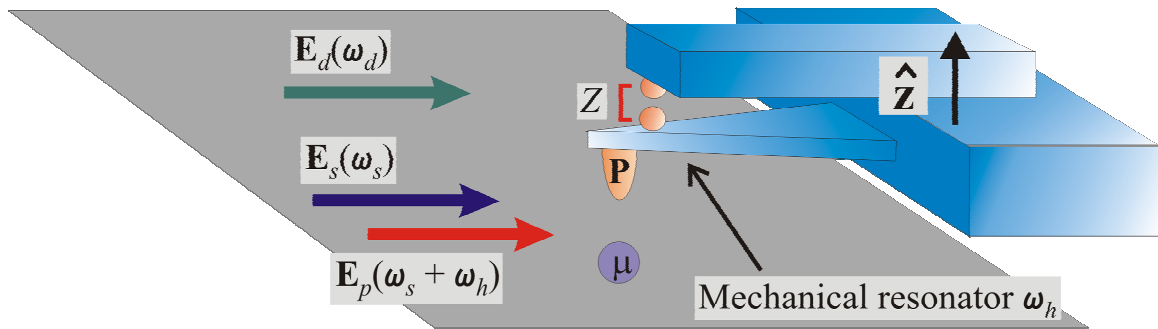


Figure 1.2: A diagram of the Force-Detected Optical Spectroscopy (FDOS) experiment. The imaging probe comprises a sharp metallic particle patterned at the end of a nanoscale mechanical resonator. The tip is positioned within a few nanometers of an isolated molecule on a surface. The linearly polarized optical fields \mathbf{E}_s and \mathbf{E}_p generate a dipole moment $\boldsymbol{\mu}$ in the molecule and a polarization \mathbf{P} in the metal tip. The electric force between $\boldsymbol{\mu}$ and \mathbf{P} has a Fourier component at the mechanical resonance frequency, which drives the mechanical motion. This motion modulates the separation Z between the two closely spaced metallic nanospheres, which results in amplitude modulated scattering of a third optical field \mathbf{E}_d at the mechanical resonance frequency ω_h , thereby allowing detection of the mechanical motion.

Figure 1.2 is a schematic of the first FDOS experiment proposed.[3] A submicron scale mechanical resonator fabricated from an optically transparent semiconductor material has a fundamental flexural mode of oscillation along the \hat{z} direction with frequency ω_h (radians/s). The entire probe assembly (blue structure) is moveable with piezoelectric positioners and active feedback electronics (not shown), so that the sharp metallic nanoparticle patterned at the end of the cantilever is positioned within a few nanometers from the surface of interest. Three linearly polarized laser fields, \mathbf{E}_s , \mathbf{E}_p , and \mathbf{E}_d , irradiate the probe/surface region. The fields, \mathbf{E}_s and \mathbf{E}_p , originate from the same laser at the optical frequency ω_s . To generate the field \mathbf{E}_p the output of the excitation laser is first split into two beams. One of the beams is sent through an acousto-optic frequency

shifter where it is mixed with an rf acoustic wave at the resonator frequency ω_h . This generates the field \mathbf{E}_p at the frequency $(\omega_s + \omega_h)$, which is then recombined with the field \mathbf{E}_s at the probe. These two excitation fields generate optical dipoles in the metallic probe at the frequencies ω_s and $(\omega_s + \omega_h)$. The laser frequency ω_s is then scanned. When it is resonant with a two-level transition in a nearby surface-bound molecule (purple circle), a dipole $\boldsymbol{\mu}$ is induced in the molecule at ω_s . The force that this induced dipole generates on the probe is $\vec{F} = \vec{\mu} \cdot (\vec{\nabla} \vec{E}_1)$, where \mathbf{E}_1 is the electric near-field generated by the probe dipoles. Since the force is in the form of a product, the time dependences of the probe dipoles and induced molecular dipole will mix to yield a dc force on the probe and an ac force at the mechanical frequency, thereby driving the harmonic motion of the resonator.

Optical interferometry is used to detect the motion of the resonator. However, since the dimensions of the mechanical resonator will generally be on the order of a few hundred nanometers, standard optical interferometry will be inefficient as the mechanical resonator will scatter light in all directions. We will now describe a novel transduction mechanism that boosts the efficiency of interferometric detection of the mechanical motion. The driven motion of the mechanical resonator is detected by scattering of a third field \mathbf{E}_d at the optical frequency ω_d . To enhance this scattering, we exploit the steep dependence of the resonant optical response on the separation between a pair of closely spaced metallic spheres. One of the spheres is attached to the resonator and the other is fixed to a rigid part of the probe assembly such that at mechanical equilibrium the spheres come within a few nanometers of touching one another. The optical frequency ω_d of the detection field \mathbf{E}_d is tuned to the plasmon resonance of the pair when at equilibrium. Motion of the resonator changes the center-to-center distance Z between the

two spheres, thereby shifting the plasmon resonance of the pair, which results in amplitude modulation of the scattered field at frequency ω_h . Homodyne mixing of the scattered field with \mathbf{E}_d at a square-law photo-detector (e.g., photodiode) results in a photocurrent at the mechanical frequency with an amplitude proportional to the amplitude of the driven mechanical motion. This is only one of several optical scattering techniques we have proposed where mechanical motion modulates the resonant plasmon scattering from nanoscopic metallic particles, allowing optical detection of high frequency mechanical resonators with sensitivity close to that set by Brownian motion noise. Later, we will quantitatively explore each of these detection schemes and evaluate the expected detection signal-to-noise.

In addition to providing spectroscopic information on the probed surface molecule, the FDOS method can determine the orientation of the single molecule on the surface, thereby providing imaging capability. To understand why this is so, we examine the Hamiltonian $\hat{H}_{int}(t)$ that describes the interaction of the molecule with the field \mathbf{E}_s :

$$\hat{H}_{int}(t) = (\vec{\mu}_{12} \cdot \vec{E}_s)(|1\rangle\langle 2| + |2\rangle\langle 1|) \cos(\omega_s t). \quad 1.1$$

In equation 1.1, \vec{E}_s is the amplitude of the optical field at ω_s , which is taken to be linearly polarized, and $\vec{\mu}_{12}$ is the (real) vector matrix element of the molecular dipole moment operator between the lower energy state $|1\rangle$ and the higher energy state $|2\rangle$ of the excited two-level transition. From this expression, we see that the magnitude of the interaction Hamiltonian depends on the angle between \vec{E}_s and $\vec{\mu}_{12}$. This interaction will be maximized when the direction of polarization of the field \mathbf{E}_s lies along the direction of the transition dipole vector and is zero when it is perpendicular. In order to image the

molecule, the mechanical amplitude is observed as a function of the direction of the laser polarization while holding the frequency ω_s of the excitation field constant. The laser frequency is then incremented and held fixed while the laser polarization is again varied. In this way, a plot is generated of the mechanical response as a function of the excitation frequency ω_s and the two polar angles of the laser polarization. The global maximum of this plot occurs when ω_s coincides with a molecular resonance and for the direction of the laser polarization that is parallel with the transition dipole.

This description of the FDOS experiment has one approximation that we address now. It is assumed that the molecular response at frequency $(\omega_s + \omega_h)$ is negligible. This will be valid if $\omega_h/2\pi > \Delta\nu$ where $\Delta\nu$ is the molecular linewidth for the two-level transition or if the polarization of the field at this frequency is orthogonal to the transition dipole. When both of these conditions are not satisfied then a molecular dipole will exist at $(\omega_s + \omega_h)$ and produce a force on the probe at ω_h due to its interaction with the probe dipole at ω_s . The phase of this force relative to that previously described becomes important and in the worst case will lead to a complete cancellation of the force on the probe at the resonance frequency ω_h .

In order to circumvent this problem, radio frequency (rf) mechanical resonators must be used, allowing only ω_s to be resonant for some transitions, since typical molecular linewidths range from hundreds of MHz to tens of GHz. Such high mechanical frequencies can only be attained when the mechanical resonator has submicron dimensions. To date, nanoscale resonators with mechanical frequencies near 1 GHz have been fabricated [4]; however, higher frequency structures may come at a cost of an increase in the mechanical damping rate due to dissipative mechanisms that become

increasingly important at the nanoscale.[5, 6] Later, we will show that the force sensitivity of the FDOS experiment is set by the mechanical damping rate and in order to measure the minute FDOS dipole forces requires as low a damping rate as possible. At this point, it is not clear if nanoscale mechanical resonators beyond about 1 GHz can be fabricated with attributes necessary for high signal-to-noise FDOS experiments.

A more elegant way to solve the problem of cancellation of the force on the probe is to use the optical modulation scheme in Figure 1.3 where the single laser field \mathbf{E}_s with frequency ω_s is sent through an acousto-optic frequency shifter. A sinusoidal voltage with angular frequency Ω is applied to the rf port of the frequency shifter to yield an output laser beam at frequency $(\omega_s + \Omega)$, which is then focused on the probe/sample region. The laser frequency is tuned so that $(\omega_s + \Omega)$ coincides with a molecular transition frequency. The top plot in Figure 1.3 shows the frequency modulation profile for the rf voltage applied to the frequency shifter. At time $t = 0$, the rf frequency is stepped up by $\delta/2$ for a duration of $T/2$ where T is the oscillation period for the mechanical resonator, changing the frequency of the excitation field to $(\omega_s + \Omega + \delta/2)$. The frequency step $\delta/2$ is chosen to be greater than half the molecular linewidth so that the excitation field is shifted out of resonance with the molecule resulting in a negligible induced molecular dipole. In the next time interval of duration $T/2$, the rf frequency is shifted back to Ω thereby bringing the excitation field into resonance with the molecule, which results in a maximum induced dipole. In the third interval of $T/2$, the excitation field is shifted by $\delta/2$ below the molecular resonance again resulting in a negligible response in the molecule. Finally in the fourth time interval, the excitation field is brought back into resonance with the molecule. This scheme results in a modulation of the amplitude of the induced molecular

dipole at the resonator frequency ω_h as depicted in the lower plot of Figure 1.3. In the time periods when the molecular dipole is present, a net force is generated on the probe due to the interaction with the probe dipole. This force is at the mechanical resonance frequency thus driving the resonator to steady state.

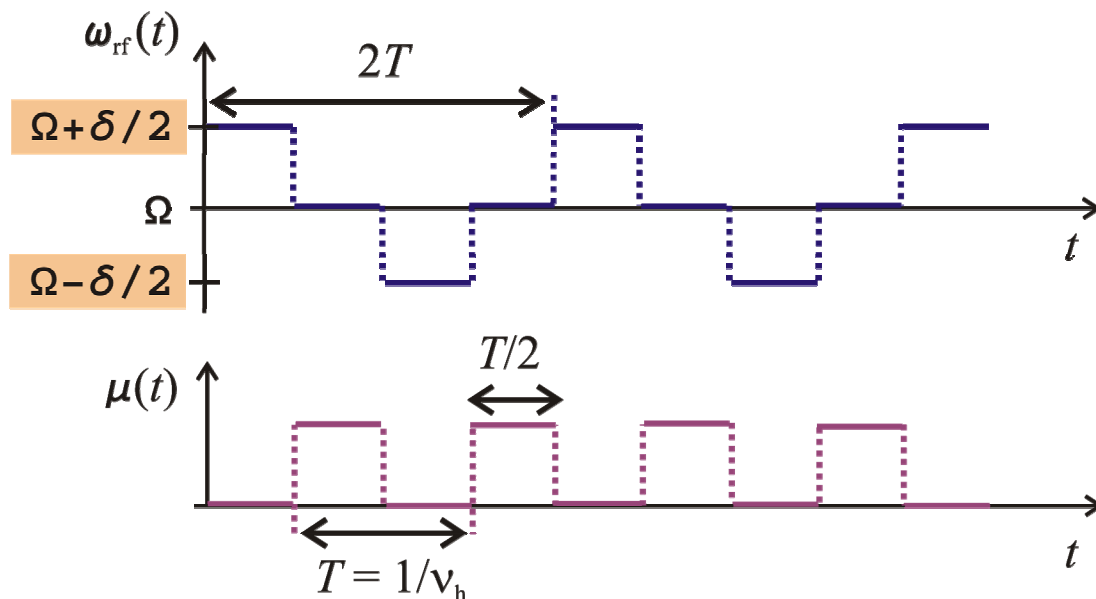


Figure 1.3: An optical modulation scheme that circumvents some experimental complications in the original FDOS experiment of Figure 1.2. The laser field \mathbf{E}_s is incident on an acousto-optic frequency shifter and a voltage at frequency Ω is applied to the rf port of the frequency shifter generating the excitation field at $(\omega_s + \Omega)$. The frequency of the rf voltage is step-modulated by $\pm \delta/2$ as illustrated in the upper plot. When the frequency $(\omega_s + \Omega)$ coincides with a molecular transition, a dipole is induced in the molecule whose amplitude is modulated as shown in the lower plot. The resulting force between the probe dipole and molecular dipole is at the mechanical resonance frequency thereby driving the mechanical resonator.

The modulation technique shown in Figure 1.3 has several advantages over the original FDOS method. First, only one excitation field is needed, which simplifies the experimental setup. Second, the period $2T$ of the modulation waveform shown in the upper plot of Figure 1.3 is arbitrary, which allows one to use low frequency mechanical resonators. Low frequency micron-scale resonators may have lower mechanical dissipation compared to high frequency nanoscale resonators since surface irregularities will become increasingly important in determining the mechanical dissipation at

nanoscale dimensions. Previously, Stowe et. al have demonstrated $5.6 \text{ aN}/\sqrt{\text{Hz}}$ force sensitivity using a micron-scale resonator with a resonance frequency of 1.7 kHz for use in magnetic resonance force microscopy (MRFM) experiments.[7] This demonstrated high force sensitivity suggests the use of such low frequency resonators in detecting the minute FDOS dipole forces. Also, because of their large size, standard fiber-optic interferometry [8] may be used to detect the motion of these micron-scale resonators. This greatly simplifies the experiment by eliminating the need for the plasmon enhanced detection mechanism. A final technical advantage of the modulation scheme in Figure 1.3 is that any driving of the mechanical motion not due to dipole forces is avoided since the time dependence of the modulation waveform is at half of the mechanical frequency.

We now introduce variants on FDOS that will be explored in more detail in the following chapters. These methods use a nanoscale ferroelectric dipole patterned on the mechanical resonator to probe single molecules dispersed on a substrate or in solution. The main advantage of using a nanoscale ferroelectric as the probe is that the electrostatic dipole moment will be many orders of magnitude larger than the optically induced dipole in a metallic probe of the same volume. This will lead to larger forces and or torques on the mechanical resonator allowing higher experimental signal-to-noise ratios. The field of the molecule needed to drive the mechanical resonator through interaction with its static dipole moment will need to have Fourier components near the fundamental of the mechanical resonator. Such components are achieved by modulating the populations of the target molecule, in contrast to the previous method where the transition dipole figures into the force. The first electret-based experiment, named Electric Dipole Difference Imaging (EDDI), employs a microscale mechanical resonator with resonance frequency

in the range from 10 kHz to 1 MHz. Fiber-optic interferometry is used to detect the motion of such resonators, eliminating the need for the exotic scattering mechanisms required for optical detection of nanoscale resonators. The mechanical probe is very similar to that in Figure 1.2 except that the metallic probe nanoparticle is replaced by a nanoscale electret particle with a static dipole moment \mathbf{p} .

Imaging and spectroscopy of single molecules on a surface is effected in the following way: Consider a molecule with diagonal matrix elements $\vec{\mu}_{11}$ and $\vec{\mu}_{22}$ of the dipole moment operator between a ground state $|1\rangle$, and excited state $|2\rangle$, respectively. Confining our attention to steady state driving of the molecule with optical excitation on resonance with the two-level transition, the dc component of the dipole induced in the molecule is $\vec{\mu}_{dc} = \rho_{11}\vec{\mu}_{11} + \rho_{22}\vec{\mu}_{22}$ where ρ_{ii} is the diagonal matrix element of the molecular density operator corresponding to the population of state $|i\rangle$. The frequency of the excitation beam is modulated exactly in the way described in Figure 1.3 so that the dipole moment of the molecule is $\vec{\mu}_{11}$ in the time intervals when the excitation is shifted off of the molecular resonance. In this way, a time-dependent difference dipole, $\Delta\vec{\mu}(t) = \rho_{11}(t)\vec{\mu}_{11} + \rho_{22}(t)\vec{\mu}_{22} - \vec{\mu}_{11}$, is generated at the mechanical resonance frequency. Using the normalization of the density operator, $\rho_{11}(t) + \rho_{22}(t) = 1$, this difference dipole may be written more simply as $\Delta\vec{\mu}(t) = \rho_{22}(t)(\vec{\mu}_{22} - \vec{\mu}_{11})$, which more clearly shows that the modulation of the excited state population is responsible for the time dependence of the difference dipole. The force between the static probe dipole \mathbf{p} and this difference dipole drives the resonant motion of the mechanical resonator.

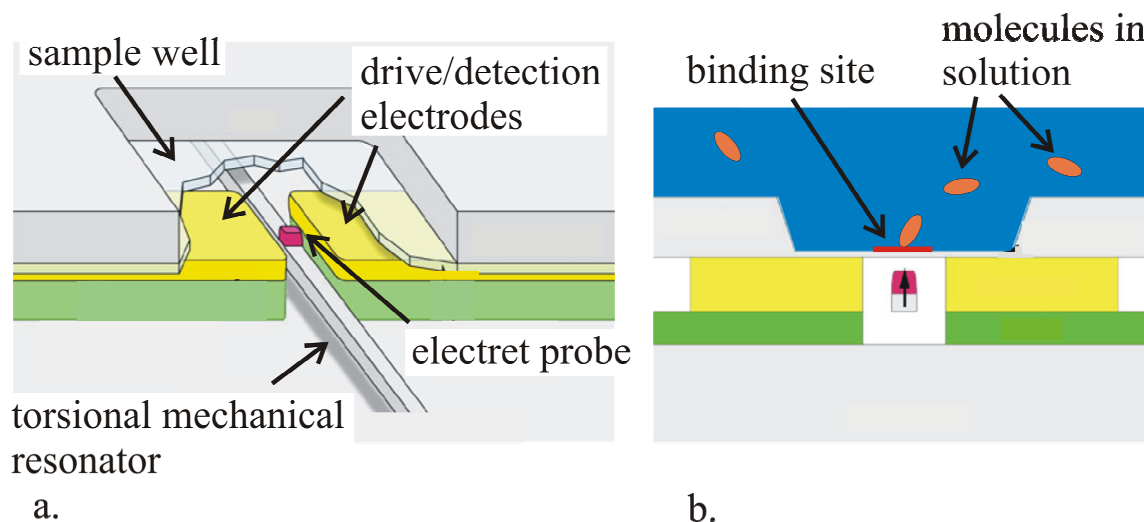


Figure 1.4: **a.** A novel nanoscale device for detecting single molecules in solution. The device (shown on the left) consists of a nanoscale semiconductor beam possessing a radio frequency torsional mode about its axis. A ferroelectric probe particle is patterned at the center of the beam and sits within the gap between two nearby electrodes. An rf voltage applied across the electrodes produces a torque on the probe dipole thereby exciting the mechanical motion. Reciprocally, the motion of the resonator may be monitored by measuring the voltage across the electrodes induced by the mechanical oscillations. This whole electromechanical assembly sits directly underneath a submicron scale sample well into which a liquid sample of interest may be analyzed for its constituents. **b.** The mechanism by which molecules are detected by this mechanical device is illustrated in the picture on the right. Molecules in solution diffuse toward a binding site that preferentially binds a specific molecular component of the complex solution. The near electric field of the probe dipole polarizes the bound molecule and the energy of interaction between these two dipoles results in a shift in the mechanical resonance frequency. Monitoring the resonance frequency with millisecond time increments allows one to observe the dynamics of binding and unbinding events as well as the orientational and configurational state of the probed molecule.

The second electret-based variant on FDOS, shown in Figure 1.4, is a device proposed to study single biologically relevant molecules in their native environment via their electrostatic interactions with the ferroelectric probe particle. A perspective view of the device is shown in Figure 1.4 a. The resonator consists of a nanoscale semiconductor beam fixed at both ends to the bulk substrate and possesses a fundamental mode of torsion about the axis of the beam with a resonance frequency in excess of 100 MHz. A nanoscale ferroelectric probe particle is patterned at the center of the beam where the torsional modeshape is at a maximum. The ferroelectric particle has a static dipole moment \mathbf{p} that points in the direction normal to the top surface of the beam and resides in the gap of two closely spaced metal electrodes. A sample well with submicron

dimensions fabricated in a second semiconductor wafer is located directly above the resonator-electrode assembly and bonded to the device wafer. The space that the resonator-electrode assembly resides in is evacuated to submillitorr pressures in order to minimize air damping of the resonator.

Figure 1.4 b is a cut-away side view of the device depicting the way in which single molecules in solution are detected by the mechanical resonator. A liquid sample containing dissolved molecules of a molecular species of interest is dispersed onto the sample wafer. A binding site (thin red line) patterned to the bottom of the well lies directly above the ferroelectric particle and consists of a molecular monolayer that preferentially binds only one particular molecular species in the multi-component solution. The wall separating the sample well and resonator-electrode assembly is a few tens of nanometers thick, which allows the probe particle to be in close proximity to any molecules that bind to the molecular monolayer. The electric field of the probe dipole polarizes a molecule bound to the monolayer and the resulting dipole-dipole interaction creates a shift in the resonance frequency of the mechanical resonator. Furthermore, the intrinsic electrostatic coupling of the probe dipole to the electrodes allows electrical driving and detection of the motion of the resonator.

The experimental apparatus of Figure 1.5 is used to electrically excite and detect the motion of the single-molecule binding sensor of Figure 1.4. A voltage pulse centered at the unperturbed mechanical resonance is generated by the rf pulse generator and travels to the electrodes via a transmission line of characteristic impedance Z_0 . A matching network is included between the line and the device so as to efficiently couple power from the low impedance transmission line to the much higher device impedance.

The electric field generated by this pulse is nominally orthogonal to the probe dipole and generates a torque on the resonator driving it to a detectably large amplitude.

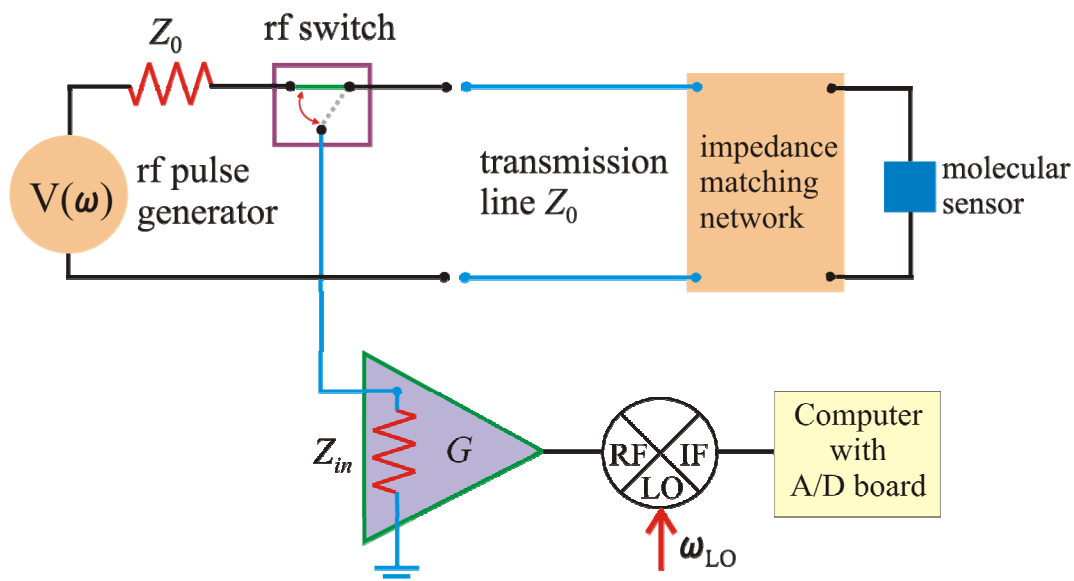


Figure 1.5: Experimental apparatus for driving and detecting the single-molecule sensor of Figure 1.4. The rf generator creates a voltage pulse centered at the unperturbed mechanical resonance frequency. The pulse travels to the device electrodes via a transmission line and impedance matching network to excite the resonant mechanical motion. Immediately afterwards, the rf switch is triggered, which connects the line to the input of a low noise voltage amplifier. The output of the amplifier is mixed down in frequency and digitized by the computer. The raw data is then Fourier transformed to yield the “instantaneous” mechanical frequency.

In the time after the voltage pulse, the rf switch is triggered and connects the transmission line to the input of a low noise rf preamplifier. The voltage induced across the electrodes resulting from the oscillatory decay of the mechanical motion is amplified with a gain of G , mixed down to a convenient frequency, and finally digitized by the computer. The raw data is then Fourier transformed thereby giving the mechanical frequency spectrum. The maximum of this spectrum corresponds to the “instantaneous” mechanical resonance frequency. This experiment is repeated many times in regular time intervals to yield a record of the mechanical resonance frequency as a function of time. The time step for this experiment is typically 2τ where τ is the “ringdown” time of the mechanical resonator. As

an example a 900 MHz resonator with a Q of 10,000 gives a time resolution of approximately $3.5 \mu\text{s}$ allowing one to probe dynamics on microsecond timescales.

The magnitude of the observed frequency shift depends on how far away the molecule is from the probe dipole and on the instantaneous orientation of the molecule relative to the probe, since the molecular polarizability is, in general, anisotropic. This experiment gives information on when binding/unbinding events occur as well as allowing one to track the trajectory and orientation of the molecule as it diffuses toward and away from the binding site. Repeating this experiment many times allows one to construct a histogram of the time an individual molecule spends at the binding site, which allows kinetic and thermodynamic parameters of the binding process to be extracted.

An important application of this novel, single-molecule binding sensor is in high-throughput, parallel-sensing of many different molecular species in a heterogeneous solution (e.g. blood). For this application, an $M \times N$ rectangular array of these devices fabricated on a single semiconductor wafer is employed. The device located in the i th row and j th column has a unique resonance frequency ω_{ij} which allows it to be distinguished from all the other members of the array. Tuning of the resonance frequency may be effected, for example, by incrementing the length of the resonator beam, holding all other dimensions fixed, as one moves along a single dimension of the array (i.e. row or column). Furthermore, the binding site associated with the i,j th resonator selectively binds a specific molecule of interest.

Impedance matching to the transmission line may be effected by using a “T” network as discussed in Chapter 4, and for the network optimized for operation at a device resonance of 950.5 MHz, we find a 40% power transfer efficiency to the device

and reasonably flat power transfer to devices with resonance frequencies spanning a 30 MHz band centered at 950.5 MHz. These results imply that many devices connected in parallel may be matched to the transmission line by the *same* network. It is important to note that switching the devices into and out of the circuit is unnecessary since the parallel impedance is dominated by the i,j th device when operating near the frequency ω_{ij} . As an example, for a typical parallel analysis the resonator array may span a total bandwidth of say, 200 MHz, thus requiring seven discrete matching networks (30 MHz bandwidth for each network). The bandwidth for the device simulated in Chapter 4 is approximately 120 kHz, which gives an array of 1,667 distinguishable devices over the 200 MHz band.

For a group of devices connected to a particular matching network, an rf pulse is applied simultaneously exciting all of the devices. In the following time period, the ringdown waveform is digitized and Fourier transformed to give the “instantaneous” frequency spectrum for this group of resonators. For this parallel array, only a single pulse generator and digitizer are required; and since the devices are addressable in the frequency domain, individual electrical connections to each device are not required. These attributes allow a dramatic reduction in the amount of hardware needed for parallel chemical analysis. To emphasize this aspect, we consider the leading, competing technology which employs a parallel array of semiconductor nanowires, where the binding molecules are covalently attached to the surface of the wire.[9, 10] The conductivity of each nanowire is monitored as molecules in solution bind and unbind to the chemically modified wires. For this method, each sensor requires separate conducting leads and its own channel on a multi-channel digitizer. The required hardware and electrical connections increase as the number of devices in the array thus making

massively-parallel chemical analysis difficult and expensive. Furthermore, nanowire sensors are restricted to detecting bound-molecules possessing a net charge whereas the sensor of Figure 1.4 is more widely applicable, since it is sensitive to both the polarizability and the net charge of the bound-molecule.

Due to the electrostatic coupling between the mechanical resonator and capacitor electrodes, the novel device of Figure 1.4 is a resonant electronic element similar in nature to a piezoelectric crystal. This device may therefore be incorporated into radio frequency communications electronics as an ultrasmall mass, low loss, resonant element that could potentially replace macroscopic components such as inductors and crystal oscillators.[11] This would result in transceivers ideal for cell phone, military, and space exploration applications, where low power consumption and small mass are critical design considerations.

References

1. Moerner, W.E. and L. Kador, *Optical-Detection and Spectroscopy of Single Molecules in a Solid*. Physical Review Letters, 1989. **62**(21): p. 2535–2538.
2. Moerner, W.E. and D.P. Fromm, *Methods of single-molecule fluorescence spectroscopy and microscopy*. Review of Scientific Instruments, 2003. **74**(8): p. 3597–3619.
3. Weitekamp, D.P. and B.M. Lambert. *Force Detected Optical Spectroscopy*. In *American Physical Society National Meeting*, 2000. Minneapolis, MN.
4. Huang, X.M.H., et al., *Nanodevice motion at microwave frequencies*. Nature, 2003. **421**(6922): p. 496–496.
5. Yasumura, K.Y., et al., *Quality factors in micron- and submicron-thick cantilevers*. Journal of Microelectromechanical Systems, 2000. **9**(1): p. 117–125.
6. Cleland, A.N. and M.L. Roukes, *Noise processes in nanomechanical resonators*. Journal of Applied Physics, 2002. **92**(5): p. 2758–2769.
7. Stowe, T.D., et al., *Attonewton force detection using ultrathin silicon cantilevers*. Applied Physics Letters, 1997. **71**(2): p. 288–290.

8. Rugar, D., H.J. Mamin, and P. Guethner, *Improved Fiber-Optic Interferometer for Atomic Force Microscopy*. Applied Physics Letters, 1989. **55**(25): p. 2588–2590.
9. Patolsky, F. and C.M. Lieber, *Nanowire nanosensors*. Materials Today, (April 2005): p. 20–28.
10. Wang, W.U., et al., *Label-free detection of small-molecule-protein interactions by using nanowire nanosensors*. Proceedings of the National Academy of Sciences. **102**(9): p. 3208–3212.
11. Weitekamp, D.P. and B.M. Lambert, *Mechanical Sensors of Electromagnetic Fields*. 2004: Patent #: US 6,835,926 B2.

Chapter 2. Engineering and Design Considerations for FDOS Experiments

In Chapter 1 we introduced two novel methods for imaging and spectroscopy of single molecules that rely on measuring the forces on a mechanical harmonic oscillator which are generated by the electric interactions between an optically induced molecular dipole and probe dipole bound to the mechanical resonator. In this chapter, we will be concerned with engineering considerations for FDOS and EDDI experiments. For FDOS we first solve for the conditions that maximize the induced transition dipole of the molecule and we then turn to geometric optimizations of the metallic probe and mechanical resonator subject to laser heating constraints and other physical restrictions. Expressions are derived for the dipole force and Brownian noise force on the resonator as functions of the geometric design parameters. We examine the scaling of these expressions with respect to the design parameters to find a geometry that gives the best signal-to-noise ratio given the various physical constraints. Finally, we will examine spectroscopy of single molecules using the EDDI technique and give realistic numerical examples for FDOS and EDDI single-molecule spectroscopy and imaging experiments.

The probed molecule is approximated as a two-level system with ground state $|1\rangle$ and excited state $|2\rangle$, that are separated in energy by an amount $\hbar\omega_0$. Choosing the zero of energy to lie halfway between the energies of the ground and excited states, the Hamiltonian describing the interaction of the molecule with the laser field is

$$\hat{H}(t) = \frac{\hbar\omega_0}{2}(|2\rangle\langle 2| - |1\rangle\langle 1|) + (\vec{\mu}_{12} \cdot \vec{E}_s)(|1\rangle\langle 2| + |2\rangle\langle 1|)\cos(\omega_s t), \quad 2.1$$

where \vec{E}_s is the amplitude of the linearly polarized laser field \mathbf{E}_s at angular frequency ω_s and the vector $\vec{\mu}_{12}$ is the real, off-diagonal matrix element of the dipole moment operator. The first term in equation 2.1 is the unperturbed molecular Hamiltonian and the second term represents the energy of coupling of the molecule to the electric field \mathbf{E}_s .

The quantum statistical state of the molecule at time t is specified by the density operator $\hat{\rho}(t)$, which is written in the two-level molecular basis as

$$\hat{\rho}(t) = \sum_{i,j=1}^2 \rho_{ij}(t) |i\rangle\langle j|, \quad 2.2$$

where $\rho_{11}(t)$ and $\rho_{22}(t)$ are, respectively, the populations of states $|1\rangle$ and $|2\rangle$ at time t and $\rho_{12}(t) = \rho_{21}(t)^*$ is the coherence between the two states. For a good discussion of the density operator the reader is referred to Chapter 2 of reference [1]. The unitary time evolution of $\hat{\rho}(t)$ is governed by the Hamiltonian $\hat{H}(t)$ in equation 2.1; however, coupling of the molecule to its environment gives rise to dissipation, which is included into the formalism through the decay rates Γ and Γ' . We define Γ to be the rate of decay of the population difference $(\rho_{22}(t) - \rho_{11}(t))$. Furthermore the coherence $\rho_{12}(t)$ decays with a rate of $\frac{\Gamma}{2} + \Gamma'$, where Γ' is the decay rate arising from “pure dephasing” mechanisms that interrupt the phase of the molecular wavefunction while conserving populations.[2] It is more convenient for our purposes to define the time constants $T_1 = \frac{1}{\Gamma}$ and $T_2 = \frac{2}{\Gamma + 2\Gamma'}$, where it is seen that T_2 satisfies the inequality $T_2 \leq 2T_1$.

Given the Hamiltonian of equation 2.1 along with the damping times T_1 and T_2 , the response of the molecule to the excitation field \mathbf{E}_s is found by solving the optical Bloch equations, which are a set of three, coupled, first-order differential equations describing the time development of the components $\rho_{ij}(t)$ of the molecular density operator. The derivation of the optical Bloch equations will not be given here; however the interested reader is referred to references [2] and [3] for a full exposition. In steady state, the expectation value of the induced molecular dipole moment is [2]

$$\langle \vec{\mu}(t) \rangle = \vec{\mu}_{12} \frac{(A(\Delta, \Omega)e^{i\omega t} + c.c.)}{2}, \quad 2.3$$

where $A(\Delta, \Omega)$ is given by [2] as

$$A(\Delta, \Omega) = 2\Omega T_2 \left(\frac{\Delta T_2 + i}{1 + 4\Omega^2 T_1 T_2 + \Delta^2 T_2^2} \right). \quad 2.4$$

In equation 2.4, $\Omega = \frac{\vec{\mu}_{12} \cdot \vec{E}_s}{2\hbar}$ is the so-called Rabi frequency, which describes the strength of interaction between the molecule and the laser field and $\Delta = \omega_s - \omega_0$ is the frequency detuning of the laser field from the molecular resonance frequency.

To achieve the highest signal-to-noise ratio in an FDOS experiment, it is crucial that one maximize the optically induced molecular dipole moment. The only experimental parameters at our disposal are the amplitude and polarization direction of the excitation field. Clearly we want the direction of the laser polarization to be parallel with the direction of the transition dipole moment $\vec{\mu}_{12}$. Saturation of the molecular transition is a direct consequence of the damping time constants T_1 and T_2 and results in an optimum laser intensity above which the amplitude of the induced dipole decreases.

To find this optimum laser intensity we solve for the value of the Rabi frequency that maximizes the magnitude of the complex function $A(\Delta, \Omega)$. From equation 2.4 we find

$$|A(\Delta, \Omega)| = \frac{2\Omega T_2 \sqrt{1 + \Delta^2 T_2^2}}{1 + 4\Omega^2 T_1 T_2 + \Delta^2 T_2^2} \quad 2.5$$

and setting $\frac{\partial |A(\Delta, \Omega)|}{\partial \Omega} = 0$ we find the optimum value of the Rabi frequency to be

$\Omega_{opt}(\Delta, T_1, T_2)$:

$$\Omega_{opt}(\Delta, T_1, T_2) = \sqrt{\frac{1 + \Delta^2 T_2^2}{4T_1 T_2}}. \quad 2.6$$

Using this result in equations 2.5 and 2.3 we find the optimized amplitude of the dipole moment to be

$$\bar{\mu}_{max} = \bar{\mu}_{12} \sqrt{\frac{T_2}{4T_1}}. \quad 2.7$$

The force \mathbf{F} between the probe dipole \mathbf{P} and molecular dipole $\boldsymbol{\mu}$ is

$$\vec{F} = \bar{\mu} \cdot (\vec{\nabla} \vec{E}_1), \quad 2.8$$

where $\vec{\nabla} \vec{E}_1$ is the gradient tensor of the electric field \vec{E}_1 of the probe dipole evaluated at the position of the surface-bound molecule. The expression for \vec{E}_1 , given in SI units with $\epsilon_0 = 8.85 \times 10^{-12} \text{ (C}^2/\text{N}\cdot\text{m}^2)$, is [4]

$$\vec{E}_1(\vec{r}) = \frac{1}{4\pi\epsilon_0 r^3} \left(3(\vec{P} \cdot \hat{r}) \hat{r} - \vec{P} \right). \quad 2.9$$

In equation 2.9, the origin of the coordinate system is taken to be at the location of the probe dipole and the position vector $\vec{r} = r\hat{r}$ from the probe dipole to the molecule is expressed in Cartesian coordinates as $\vec{r} = x_i \hat{e}_i$ where $x_1 = x$, $x_2 = y$, $x_3 = z$ and \hat{e}_i are the

Cartesian unit vectors. The summation convention for expressions with repeated indices will be used throughout. In Cartesian coordinates, the electric field gradient tensor is

$$\vec{\nabla} \vec{E}_1 = \hat{e}_j \hat{e}_k \frac{\partial E_{1k}}{\partial x_j} \text{ where}$$

$$\frac{\partial E_{1k}}{\partial x_j} = \frac{3}{4\pi\epsilon_0 r^5} \left[-\frac{5P_m x_m x_k x_j}{r^2} + P_j x_k + P_k x_j + P_m x_m \delta_{kj} \right]. \quad 2.10$$

To solve for the force between the molecule and the metallic probe in an FDOS experiment requires finding the optically induced probe dipole and molecular dipole for a given set of experimental conditions and using these in equation 2.8. We have found the conditions under which the molecular dipole is maximized and now consider optimizations of the probe/resonator assembly to maximize the force on the mechanical resonator.

The metallic probe is modeled as a prolate (cigar shaped) ellipsoid of revolution with a semi-major axis of length a and a semi-minor axis of length b . The linearly polarized excitation field \mathbf{E}_p at optical frequency ω_p is approximated as a uniform plane wave over the volume of the probe. The problem of electromagnetic scattering from small metallic particles was first investigated by Mie [5] and the exact solution involves a complicated expansion in vector normal modes (see [6, 7]). If the dimensions of the particle are much smaller than the wavelength of the excitation light, the electrostatic approximation may be used in which only the first term of the normal mode expansion is retained. In this approximation, the component of the dipole moment along the j th principal axis of the particle generated by the incident field \mathbf{E}_p is [7]

$$P_j(\omega_p) = \alpha_j(\omega_p) E_{pj}(\omega_p), \quad 2.11$$

where $E_{pj}(\omega_p)$ is the component of the field \mathbf{E}_p along the j th principal axis and $\alpha_j(\omega_p)$ is the polarizability of the particle along the j th axis in the electrostatic approximation, which is given in MKS units by [7]

$$\alpha_j(\omega_p) = \varepsilon_0 V \kappa_m(\omega_p) \frac{\kappa(\omega_p) - \kappa_m(\omega_p)}{\kappa_m(\omega_p) + L_j(\kappa(\omega_p) - \kappa_m(\omega_p))} \equiv \varepsilon_0 V f(\omega_p, L_j). \quad 2.12$$

In equation 2.12, $\kappa(\omega_p)$ and $\kappa_m(\omega_p)$ are, respectively, the dimensionless bulk dielectric constant for the metal particle and the medium surrounding the particle at the optical frequency ω_p , and $V = \frac{4\pi}{3} ab^2$ is the volume of the ellipsoidal probe. Furthermore, we have defined the dimensionless function $f(\omega_p, L_j)$ as the factor in the polarizability in equation 2.12 that depends on the excitation frequency through the dielectric constants and the dimensionless depolarization factor L_j associated with the j th axis. The depolarization factor is given by [7]

$$L_j = \frac{ab^2}{2} \int_0^\infty \frac{dq}{(\xi_j^2 + q) \sqrt{(a^2 + q)(b^2 + q)^2}}, \quad 2.13$$

where $\xi_j = a$ or b . In what follows, we will be interested in the geometry where the polarization vector of the excitation field is aligned along the major axis of the particle. Performing the integration in equation 2.13 we find the analytical expression for L_a to be

$$L_a = \frac{-2\sqrt{1 - \frac{1}{\eta^2}} + \ln \left[\frac{\left(\sqrt{1 - \frac{1}{\eta^2}} + 1 \right)}{\left(1 - \sqrt{1 - \frac{1}{\eta^2}} \right)} \right]}{2\eta^2 \left(1 - \frac{1}{\eta^2} \right)^{3/2}}, \quad 2.14$$

where the aspect ratio η of the particle is equal to a/b .

We will show in the following paragraphs that dissipation of electromagnetic energy as heat is governed by the imaginary part of α , which is seen in equation 2.12 to arise from the complex nature of the dielectric constants. In addition to intrinsic losses of the probe material, another loss mechanism, known as radiation damping, is considered. This is the damping due to the fact that the optically induced probe dipole radiates electromagnetic energy. Taking radiation damping into account, the polarizability of the particle, denoted $\alpha_j^{R.D.}(\omega_p)$ becomes [8]

$$\alpha_j^{R.D.}(\omega_p) = \frac{\alpha_j(\omega_p)}{\left(1 - i \frac{\omega_p^3 \alpha_j(\omega_p)}{6\pi\epsilon_0 c^3}\right)}. \quad 2.15$$

The magnitude of the induced probe dipole in equation 2.11 will be limited by laser heating of the probe, which will create undesirable temperature dependent shifts in the mechanical resonance frequency. Therefore, a thermal conductivity analysis is needed in order to assess the maximum allowable excitation intensity. For the case where the field E_p lies along the major axis of the particle, the power W dissipated as heat in the metallic probe is given by [2]

$$W = -\frac{\omega_p}{2} \text{Re} \left[i E_a^* P_a \right], \quad 2.16$$

where the subscript a denotes the long axis of the particle and E_a , the total electric field inside the particle, is the vector sum of the incident field and the field due to the induced dipole. Expressed in terms of the incident field we have [7]

$$E_a = E_p - \left(\frac{L_a \alpha_a^{R.D.}}{\epsilon_0 \kappa_m V} \right) E_p. \quad 2.17$$

Assuming that κ_m is real (negligible optical absorption in the beam material) we use equation 2.17 and the fact that $P_a = \alpha_a^{R.D.} E_p$ to arrive at the expression for the power dissipated as heat:

$$W = \frac{\omega_p}{2} \text{Im}[\alpha_a^{R.D.}] (E_p)^2. \quad 2.18$$

The probe-resonator design used in the rest of this chapter is shown in Figure 2.1. The mechanical resonator comprises a semiconductor beam of length L with a rectangular cross-section of area A . Using standard MEMS and NEMS fabrication techniques [9-11], the resonator structure is defined and chemically etched from the bulk substrate. Two modes of mechanical oscillation are of interest, the “diving board mode”, where the free end oscillates in the \hat{z} direction and the “wiper mode”, where the end oscillates along the \hat{x} direction. The metallic probe is patterned at the end of the beam such that a large fraction of the surface area of the probe is in intimate contact with the beam. This allows for efficient transport of heat from the metal particle to the beam so that the temperature gradient between the two may be neglected. Furthermore, we assume that only the metal probe particle absorbs the incident radiation and that the surface delineating the resonator from the substrate is at the ambient temperature T_a , which will usually be taken to be 300 K.

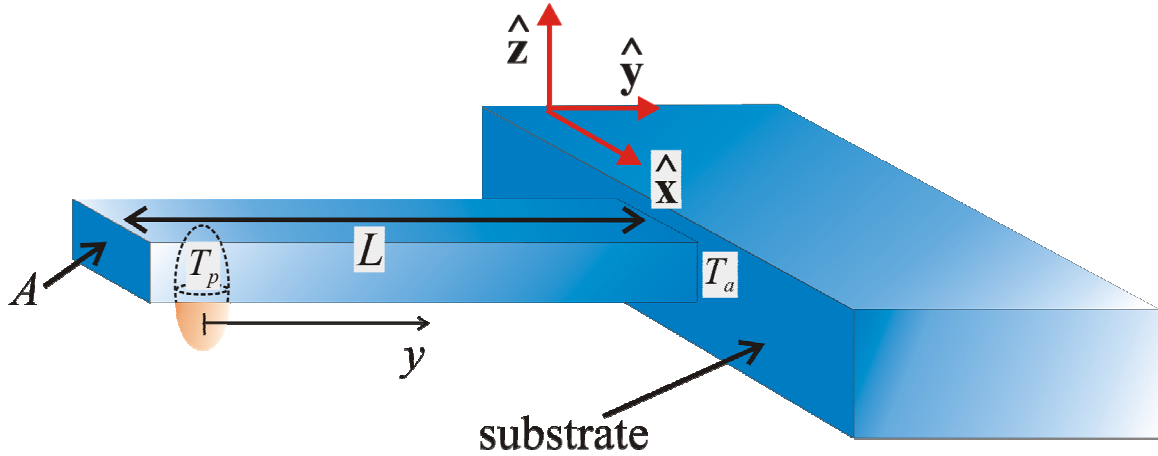


Figure 2.1: Probe-resonator geometry considered for FDOS imaging and spectroscopy of single molecules on a surface. The resonator is a beam of length L and cross-sectional area A fabricated from the semiconductor substrate with modes of linear oscillation in the z and x direction. The metallic probe particle is patterned at the end of the beam and is partially embedded in the beam so as to ensure good thermal contact with the mechanical resonator. It is assumed that the temperature of the beam at the dividing surface between the resonator and substrate is at the ambient temperature T_a .

The thermal current density $J(y,t)$ (watts/m²) and absolute temperature $T(y,t)$ of the beam at position y and time t obey the energy continuity equation, which in one dimension is [12]

$$\frac{\partial[J(y,t)]}{\partial y} + \bar{C}_v \frac{\partial[T(y,t)]}{\partial t} = 0, \quad 2.19$$

where \bar{C}_v is the heat capacity per unit volume of the beam material and the position coordinate y is measured from the center of the metallic probe as shown in Figure 2.1.

The relation between the thermal current density and the temperature is given by [12]

$$J(y,t) = -\gamma \frac{\partial[T(y,t)]}{\partial y}, \quad 2.20$$

where γ is the thermal conductivity of the beam material in watts/(m·K). In steady state (denoted by the subscript *s.s.*), $\frac{\partial T(y,t)}{\partial t} = 0$, which implies that at any point along the

length of the beam the absorbed power W is equal to the power flow $J_{s.s.}(y)A$ of

thermal energy past the cross-sectional area A . This condition along with equation 2.20 gives a first-order differential equation for the steady state temperature along the beam:

$$W = -\gamma A \frac{\partial [T_{s.s.}(y)]}{\partial y}. \quad 2.21$$

The solution of equation 2.21, given the boundary condition $T_{s.s.}(y=L) \equiv T_a$, is

$$T_{s.s.}(y) = \frac{W}{\gamma A} (L-y) + T_a. \quad 2.22$$

At the beam center, defining $T_{s.s.}(0) \equiv T_p$, we have

$$T_p = \frac{WL}{\gamma A} + T_a. \quad 2.23$$

Using equation 2.18 we arrive at the value of the excitation field that results in a temperature rise $\Delta T = T_p - T_a$ of the probe:

$$E_p(\Delta T) = \sqrt{\frac{2\gamma A \Delta T}{L\omega_p \text{Im}[\alpha_a^{R.D.}]}}. \quad 2.24$$

For a fixed optical frequency, there exists an optimum aspect ratio for the probe particle such that $|\alpha_a|$ in equation 2.12 is maximized. This condition is known as the plasmon resonance. In the following we will optimize the shape of the probe so as to satisfy the plasmon resonance condition for the two cases where the probe is fabricated from silver or gold.

Figure 2.2 plots the real and imaginary parts of the bulk dielectric constant $\kappa = \kappa_1 + i\kappa_2$ for silver and gold versus the excitation wavelength from 400 nm to 1600 nm. These data were generated from the experimentally recorded values of the complex index of refraction $\tilde{n} = n + ik$ of reference [13], where $\kappa_1 = n^2 - k^2$ and $\kappa_2 = 2nk$.

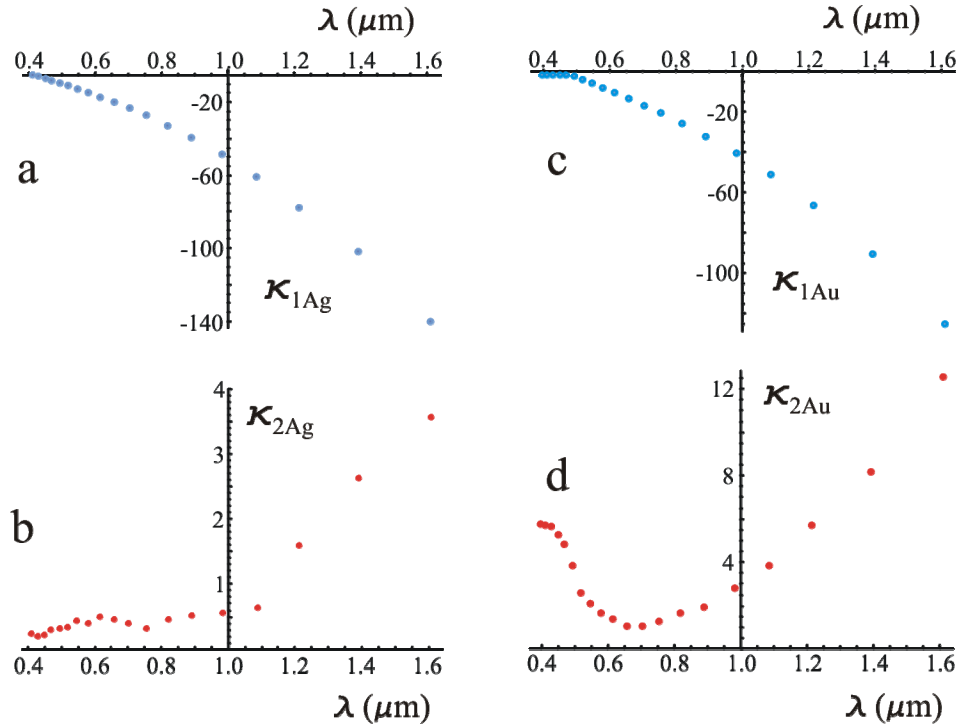


Figure 2.2: Plots of the real part κ_1 and imaginary part κ_2 of the complex dielectric constant for silver (plots a and b) and gold (plots c and d). These plots were derived from the experimentally measured data of the complex index of refraction $\tilde{n} = n + ik$ of reference [13] with $\kappa_1 = n^2 - k^2$ and $\kappa_2 = 2nk$.

To find the maximum value of $|\alpha_a|$ at each wavelength requires maximizing the magnitude of the function $f(\omega_p, L_a)$ of equation 2.12 with respect to variations in L_a . Equivalently, we may minimize the magnitude squared of the denominator of $f(\omega_p, L_a)$ since the numerator is a complex number that is independent of L_a . Characterizing the external medium by $\kappa_m = 1$, then for the k th wavelength data point λ_k of Figure 2.2 we have

$$f(\omega_k, L_a) = \frac{\kappa_1(\omega_k) - 1 + i\kappa_2(\omega_k)}{1 + L_a(\kappa_1(\omega_k) - 1) + iL_a\kappa_2(\omega_k)}, \quad 2.25$$

where $\omega_k = 2\pi c/\lambda_k$ and $c = 3.0 \times 10^8$ (m/s) is the speed of light. Taking the derivative with respect to L_a of the magnitude squared of the denominator of equation 2.25 and setting this equal to zero, we solve for the optimum value of the depolarization factor as

$$L_a^{opt} = \frac{1 - \kappa_1}{|\kappa|^2 - 2\kappa_1 + 1}. \quad 2.26$$

We find the optimized aspect ratio η^{opt} of the probe particle at each wavelength by substitution of L_a^{opt} into equation 2.14 and numerically solving the resulting transcendental equation. Also when L_a^{opt} is substituted into equation 2.25, the optimized function $f^{opt}(\omega_k, L_a^{opt})$ is purely imaginary and given by

$$f^{opt}(\omega_k, L_a^{opt}) = i \frac{(\kappa_1 - 1)^2 + \kappa_2^2}{\kappa_2}. \quad 2.27$$

The optimized aspect ratio η^{opt} and the magnitude of the function $f^{opt}(\omega_k, L_a^{opt})$ are plotted in Figure 2.3 for silver and gold at each wavelength data point of Figure 2.2.

At first thought, it may seem unnecessary to optimize the aspect ratio of the probe so as to be at plasmon resonance since one may just increase the excitation field to obtain a larger probe dipole. However, the heating analysis assumes that only the probe particle absorbs the radiation. Since the field \mathbf{E}_p can be focused at best to a diffraction-limited spot size, the volume of the substrate irradiated by the laser spot will be many orders of magnitude larger than the volume of the probe particle. Thus at some power of the excitation field, absorption by the resonator and surrounding substrate will be a non-negligible contribution to the heating. To minimize this effect it is therefore crucial to optimize the shape of the probe such that it has a plasmon resonance at the frequency of operation.

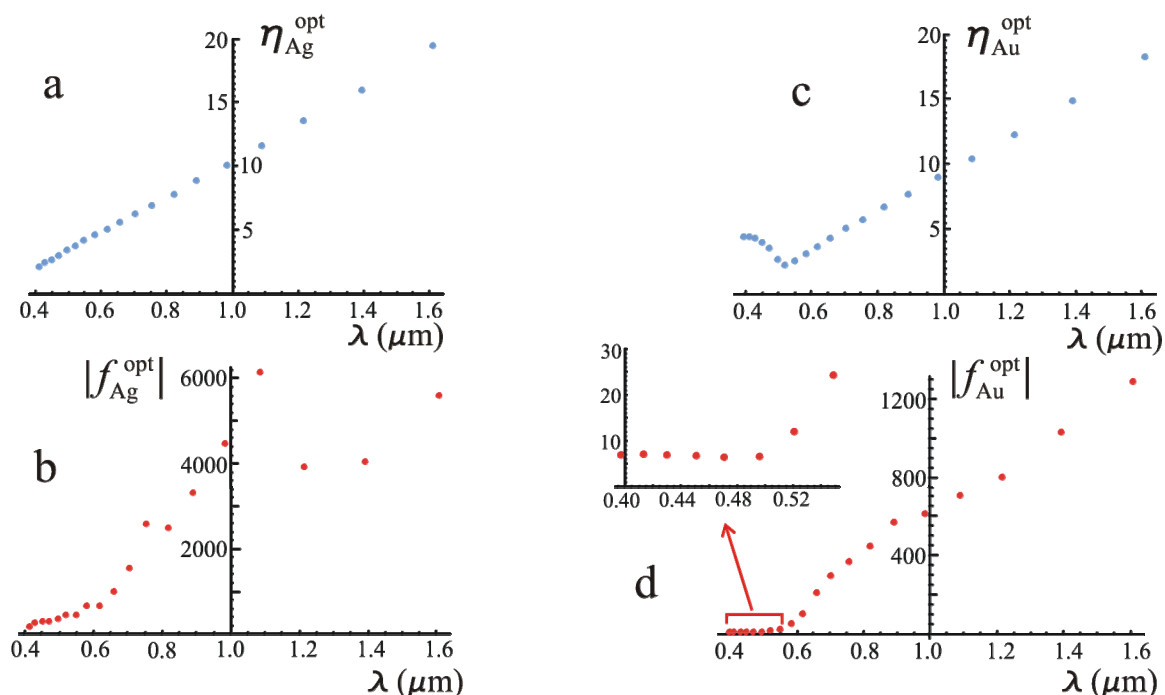


Figure 2.3: Plots of the optimized aspect ratio and the corresponding dimensionless function f for a silver (plots a and b) and gold (plots c and d) ellipsoidal probe using the dielectric data in Figure 2.2. In the visible to near I.R. wavelength range, a silver probe has a much larger resonant polarizability compared to a probe fabricated from gold.

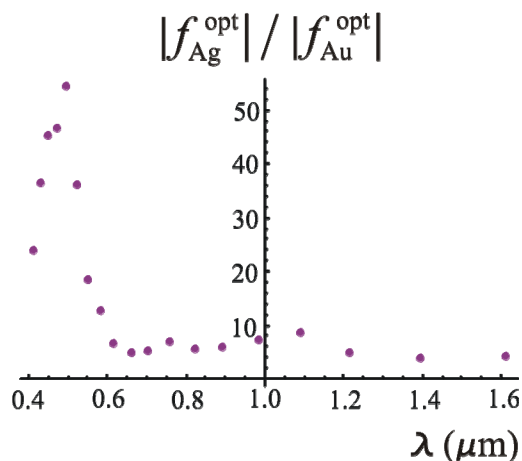


Figure 2.4: Relative enhancement factor of the resonant polarizability for an optimized silver probe versus an optimized gold probe of the same volume. Over the wavelength range shown, the enhancement factor has a minimum value of approximately four at a wavelength of 1400 nm and peaks to approximately 54 at a wavelength of 500 nm.

In Figure 2.4 the ratio $|f_{Ag}^{opt}|/|f_{Au}^{opt}|$ is plotted, providing a quantitative measure of the relative enhancement in the resonant polarizability for a shape-optimized silver probe

versus an optimized gold probe with the same volume. From this we conclude that silver is the better material of choice over gold for the metallic probe, giving a factor of four enhancement in the near I.R. region and peaking to approximately 54 in the visible region.

Although silver has a greater polarizability enhancement over gold a major drawback to using silver as the probe material is that it oxidizes easily in air to form Ag_2O whose dielectric properties are very different from those of silver. If one is to use silver as the probe material, it is prudent to always keep the probe in an inert environment (e.g., vacuum, N_2 atmosphere). If the probe is to be used in air, surface modification of the silver probe with organic ligands may be necessary to stabilize the probe against oxidation.[14, 15] However, chemical surface modifications in general will change the plasmon resonance properties, therefore, additional measurements are required to determine the shift of the resonance and the change in the dissipation relative to an unmodified silver particle.

We now examine the dependence of the coherent FDOS force and noise force on the dimensions of the mechanical resonator to arrive at a practical resonator design that maximizes the signal-to-noise ratio. We consider the geometry of Figure 2.1 and take the mechanical resonator to be fabricated from aluminum nitride. Aluminum nitride has one of the largest thermal conductivities (140 watts/(m·K)) of the known semiconductor substances and is therefore an ideal substance for efficient heat transport along the length of the resonator.[16] In addition, laser heating due to absorption by the resonator material is minimized over the wavelength range considered in figures 2.2–2.4 since the bandgap of this material occurs at 6.2 eV ($\lambda = 200$ nm).[17]

To obtain numerical values for the dipole force on the probe we consider the geometry where \mathbf{P} is induced along the \hat{z} direction and $\boldsymbol{\mu}$ is along the \hat{x} direction. From equations 2.8 and 2.10, the x-component of the dipole force, which drives the “wiper mode” of mechanical motion, is

$$F_x = \mu \frac{\partial E_{1x}}{\partial x} = \frac{3\mu P}{4\pi\epsilon_0 r^5} \left[-\frac{5zx^2}{r^2} + z \right] \quad 2.28$$

and taking the probe to be directly above the molecule this force simplifies to

$$F_x = \frac{3\mu P}{4\pi\epsilon_0 z^4}. \quad 2.29$$

For a shape-optimized probe at a particular wavelength substitution of equations 2.12 and 2.27 into 2.15 gives the radiation damped polarizability of the particle denoted, $\alpha_{opt}^{R.D.}$:

$$\alpha_{opt}^{R.D.}(\omega_k) = i \frac{\epsilon_0 V |f^{opt}(\omega_k, L_a^{opt})|}{\left(1 + \frac{\omega_k^3 V |f^{opt}(\omega_k, L_a^{opt})|}{6\pi c^3} \right)}, \quad 2.30$$

where $V = \frac{4\pi}{3} \eta^{opt} b^3$. Using equation 2.24 we find the induced probe dipole $P_a = \alpha_{opt}^{R.D.} E_p(\Delta T)$:

$$|P^{opt}(\omega_k)| = \sqrt{\frac{2\gamma |\alpha_{opt}^{R.D.}(\omega_k)| \Delta T}{\omega_k} \frac{A}{L}}. \quad 2.31$$

The closest distance of approach between the end of the ellipsoidal probe and the surface-bound molecule is denoted R_0 . This distance is taken large enough so that the damping of the mechanical motion due to interactions with the surface is negligible compared to the intrinsic mechanical damping of the resonator. Therefore, the distance of the probe dipole

from the molecular dipole is $z = a + R_0 = \eta^{opt} b + R_0$, so that the dipole force in equation 2.29 is

$$F_x = \frac{3\mu}{4\pi\epsilon_0} \sqrt{\frac{2\gamma |\alpha_{opt}^{R.D.}(\omega_k)| \Delta T}{\omega_k} \frac{A}{L(\eta^{opt} b + R_0)^8}}. \quad 2.32$$

For the resonator geometry of Figure 2.1, the mechanical resonance frequency of the “wiper mode” (linear oscillation along \hat{x}) is given by [18]

$$\nu_h = \frac{1}{2\pi} \sqrt{\frac{3E_{AIN}I}{0.23mL^3}} \quad 2.33$$

where $E_{AIN} = 330$ GPa [16] is the elastic modulus of AlN, $I = \frac{1}{12} w^4$ is the area moment of inertia of the square cross section of the beam with side length w , and $m = \rho_{AIN} L w^2$ is the mass of the beam with $\rho_{AIN} = 3260$ (kg/m³) [16] the density of AlN.

Ideally, the noise in the FDOS experiment is set by Brownian motion of the mechanical resonator. At absolute temperature T and in a measurement bandwidth $\Delta\nu$ centered at the mechanical resonance frequency ω_h the root-mean-square noise force on the resonator is

$$\bar{F}_x = \sqrt{\frac{4m_{eff}\omega_h k_B T}{Q} \Delta\nu}, \quad 2.34$$

where m_{eff} , the effective motional mass of the resonator, is $0.23m$ for the wiper mode, $k_B = 1.38 \times 10^{-23}$ (J/K) is Boltzmann’s constant and Q is the quality factor of the mechanical resonance. For a derivation of equation 2.34 see Appendix A. Using equation 2.33, the noise force may be written

$$\bar{F}_x = (0.23\rho_{AIN}E_{AIN})^{1/4} \sqrt{\frac{2k_B T \Delta\nu}{Q} \frac{A^{3/2}}{L}}. \quad 2.35$$

For the driving scheme illustrated in Figure 1.3, the dipole force is a square wave with average value $F_x/2$ and a peak-to-peak value of F_x . The Fourier component of this force at the resonator frequency, $\nu_h = \omega_h/2\pi$, is $2F_x/\pi$, giving a signal-to-noise ratio of

$$SNR_F = \frac{2F_x}{\pi \bar{F}_x} = \frac{6\mu}{4\pi^2 \varepsilon_0 (0.23 \rho_{AIN} E_{AIN})^{1/4}} \sqrt{\frac{\gamma |\alpha_{opt}^{R.D.}(\omega_k)| Q \Delta T}{k_B T \omega_k \Delta \nu} \frac{1}{A^{1/2} (\eta^{opt} b + R_0)^8}}. \quad 2.36$$

The dipole force and SNR decrease steeply as the width b of the particle gets larger. Therefore it is critical to make the probe particle as small as possible. However, there are physical limits to how small we can make the probe. If the dimensions of the probe are too small (i.e., b less than ~ 10 nm) [19], then scattering of the conduction electrons off of the surface of the probe will become a non-negligible source of damping, which must then be included along with the intrinsic loss and radiation loss already considered.[19] Furthermore, trapping of conduction electrons by surface states is another damping mechanism that becomes increasingly important as the size of the particle decreases. The dependence on the cross-sectional area of the beam is less critical since the coherent force depends on the cross-sectional area as $A^{1/2}$ and the noise force goes as $A^{3/4}$ thereby partially canceling out in the SNR. The coherent force and noise force scale in the same way on the length of the resonator beam so that the SNR is independent of the length L . This fact allows one the freedom of varying the length of the beam so as to tune the mechanical resonance frequency to a convenient value.

As a numerical example, we consider a 7 micron long AlN beam with a 40 nm side length. Using equation 2.33 we find the mechanical resonance frequency to be 1.4 MHz. If we assume $Q = 1000$ then using equation 2.35 the noise force on the resonator at

$T = 300 \text{ K}$ is $3.5 \times 10^{-17} \sqrt{\Delta\nu}$ (Newtons). The probe is taken to be a 20 nm wide ($b = 10$ nm) silver ellipsoid with an aspect ratio that is optimized at each wavelength for plasmon resonance as shown in Figure 2.3. Using the data in Figure 2.3 and equation 2.24 we may find the value of the excitation field at each wavelength that generates a temperature rise $\Delta T = 1^\circ \text{ C}$ in the probe, and the corresponding dipole (equation 2.31) induced in the shape-optimized probe. These results are plotted in Figure 2.5 where the induced plasmon dipole has a maximum value of $9.5 \times 10^{-27} \text{ C}\cdot\text{m}$ at $\lambda = 1.6$ microns and a minimum value of $3.8 \times 10^{-28} \text{ C}\cdot\text{m}$ at $\lambda = 400 \text{ nm}$.

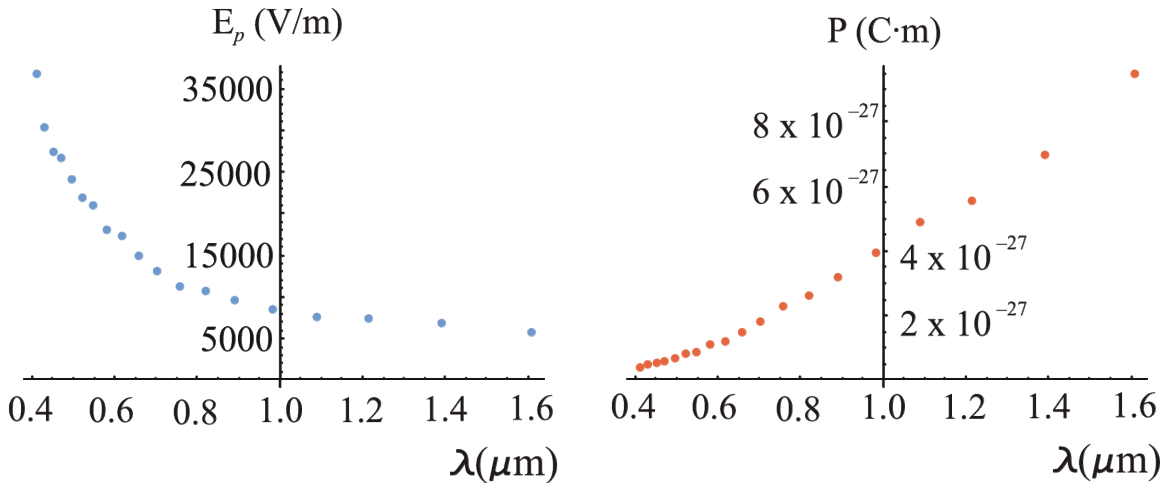


Figure 2.5: Plots of the excitation field that produces a 1° C temperature rise in the Ag probe and the corresponding optical dipole induced in the shape-optimized probe as a function of the excitation wavelength.

Let us consider detecting a chromophore with a transition dipole matrix element $\vec{\mu}_{12} = 0.1 \text{ Debye}$ in the \hat{x} direction. We consider the scheme of Figure 1.3 where there is only one excitation field. Since the probe dipole and molecular dipole are orthogonal to one another we may simultaneously optimize the probe and molecular responses by adjusting the amplitude and the polarization direction of the single excitation field \mathbf{E} so that the projection along \hat{z} equals $E_p (\Delta T = 1^\circ \text{ C})$ and the projection along \hat{x} corresponds

to the optimum Rabi frequency of equation 2.6. Furthermore, the optical response of the probe along \hat{x} will be negligible compared to the response along \hat{z} since the probe is not at plasmon resonance along its short dimension. We will take the limit where pure dephasing mechanisms are absent, i.e., $T_2 = 2T_1$, which represents a best case scenario. For the optimum value of the Rabi frequency, the magnitude of the induced molecular dipole is $|\vec{\mu}_{12}|/\sqrt{2} = 0.071$ Debye. For a shape-optimized silver probe located directly above the molecule and taking $R_0 = 20$ nm, the force at the 1.4 MHz mechanical resonance and SNR in a 1 Hz bandwidth are plotted in Figure 2.6 vs. the excitation wavelength.

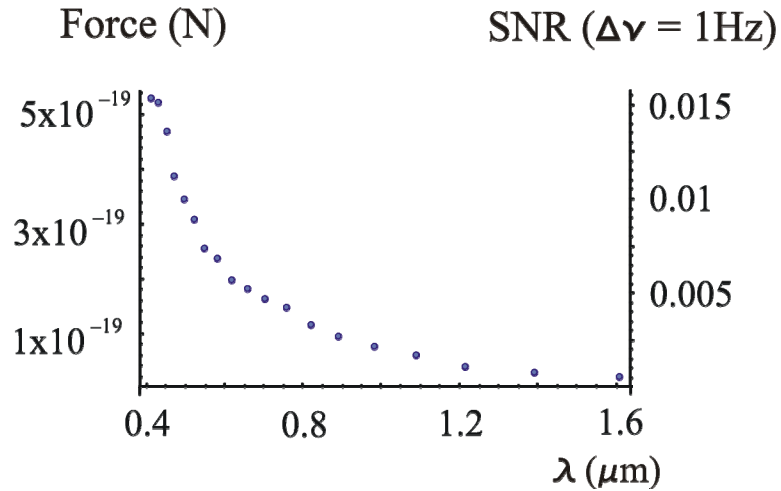


Figure 2.6: Plots of the dipole force on the resonator at the mechanical resonance generated by a 0.071 Debye induced molecular dipole and the SNR in a 1 Hz bandwidth. The Brownian noise force only depends on the parameters of the mechanical resonator and has a value of 3.5×10^{-17} (N) in the 1 Hz measurement bandwidth.

Recently, the transition dipole moment of ~ 30 nm diameter InGaAs/GaAs quantum dots was measured with cavity ringdown optical absorption and found to be 8.8×10^{-29} C·m = 26.3 D at $\lambda = 1.151$ microns.[20] We now would like to evaluate the SNR for imaging and spectroscopy of these quantum dots by FDOS. We take $R_0 = 35$ nm, which is the sum of a 20 nm distance of closest approach and the 15 nm radius of the dot.

The peak force is 7.05×10^{-18} N and occurs at $x = 0$ giving a SNR of 0.20 in a 1 Hz bandwidth. Plotted in Figure 2.7 is a constant-height line scan along the x-direction with $y = 0$ of the force due to the transition dipole of the quantum dot. The imaging resolution for this experiment is seen to be 100 nm FWHM.

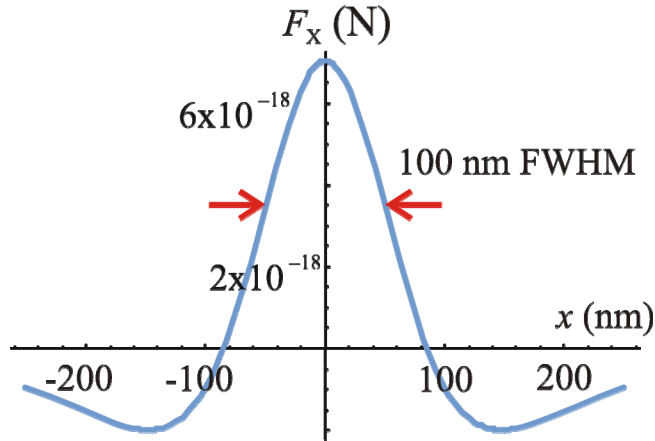


Figure 2.7: A plot of the resonant force on the probe generated by the optically induced transition dipole of a single InGaAs/GaAs quantum dot. The probe is scanned at constant height ($R_0 = 35$ nm) in the x-direction holding $y = 0$. At $x = 0$, the force has a maximum value of 7.05×10^{-18} N, which gives a peak SNR of 0.20 in a 1 Hz measurement bandwidth. The imaging resolution is defined as the full width at half maximum (FWHM) of the force profile plotted above and is 100 nm.

We now turn to the case of EDDI imaging and spectroscopy of a single molecule with a ground state dipole $\vec{\mu}_{11}$ and excited state dipole $\vec{\mu}_{22}$ in interaction with a static electret moment on the probe. The force at the resonator frequency is generated by modulating the excited state population $\rho_{22}(t)$ as in the scheme of Figure 1.3. The total force on the resonator is therefore given by

$$\vec{F}_{EDDI}(t) = \rho_{22}(t)(\vec{\mu}_{22} - \vec{\mu}_{11}) \cdot (\vec{\nabla} \vec{E}_1), \quad 2.37$$

where $\vec{\nabla} \vec{E}_1$ is the gradient tensor of the electric field of the electret dipole. We will again consider the probe dipole to be oriented along \hat{z} and take $\vec{\mu}_{22}$ and $\vec{\mu}_{11}$ to both be along \hat{x} so that the x-component of the EDDI force at the resonator frequency ω_h is

$$F_{EDDI\ X} = \left(\frac{2}{\pi}\right) \frac{3\rho_{22}^{ss}(\mu_{22} - \mu_{11})P}{4\pi\epsilon_0} \left[-\frac{5zx^2}{r^7} + \frac{z}{r^5}\right], \quad 2.38$$

where μ_{ii} is the magnitude of the corresponding dipole moment and ρ_{22}^{ss} is the optically induced, steady state population of the excited state.

We use the optical Bloch equations to evaluate the excited state population in steady state ρ_{22}^{ss} , which is [2]

$$\rho_{22}^{ss} = \frac{1}{2} \left(\frac{4\Omega^2 T_1 T_2}{1 + \Delta^2 T_2^2 + 4\Omega^2 T_1 T_2} \right). \quad 2.39$$

As a function of the Rabi frequency, ρ_{22}^{ss} does not have a local maximum and simply asymptotes to the value 0.5 as $\Omega \rightarrow \infty$. In the following, we will take ρ_{22}^{ss} to be 0.05. This conservative value ensures that a low enough laser power is used so as to avoid photo-degradation of the molecule and/or probe.

As an example of difference dipole detection, we take the data of El-Kamary and Rettig [21] who studied three different coumarin laser dyes (labeled **I**, **II**, and **III**) and found the difference dipole $\Delta\mu$ between the ground and excited states for each molecule to be 5.61 D, 8.11 D, and 13.40 D, respectively.[21]

Consider imaging an isolated molecule of coumarin **I** since this has the smallest difference dipole. Given R_0 , the distance of closest approach of the spherical probe, the maximum force on the resonator occurs when the radius of the probe is $3R_0$. We will take $R_0 = 20$ nm which sets the radius of the probe to be 60 nm. We will use the 1.4 MHz resonator from before with the ferroelectric sphere patterned at the end of the resonator beam. The probe is made of the material lead zirconate titanate (PZT) and has a polarization of 0.35 C/m². Recall that for this resonator, the Brownian noise force in a 1

Hz bandwidth centered at the resonance frequency is 3.5×10^{-17} N. In Figure 2.8 a constant-height, one-dimensional line scan of the force is plotted along the x-direction with $y = 0$. The peak dipole force of 1.24×10^{-13} N occurs at $x = 0$, which gives a peak SNR of 3543 in a 1 Hz measurement bandwidth. Also, it can be seen that the imaging resolution for this experiment is 46 nm FWHM.

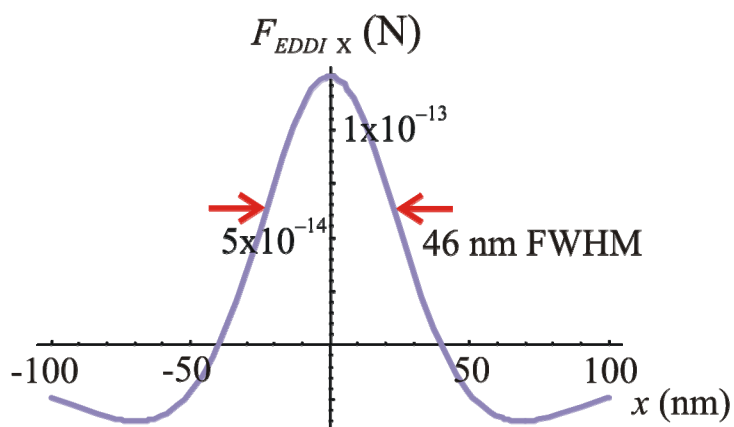


Figure 2.8: A plot of the resonant force on the probe for EDDI imaging of the 5.61 D difference dipole of coumarin **I** of reference [21]. The probe is scanned at constant height ($R_0 = 20$ nm) in the x-direction holding $y = 0$. The peak force is 1.24×10^{-13} N giving a SNR of 3543 in a 1 Hz bandwidth. An imaging resolution of 46 nm FWHM is predicted for this experiment.

Vibrational spectroscopy using EDDI is an important application for determining the chemical identity of the single, surface-bound molecule. For many organic molecules a difference dipole of 0.01 debye between the ground state and an excited vibrational state is typical.[22] For detecting this 0.01 debye difference dipole, we use the same experimental arrangement as for imaging of the coumarin **I** molecule. For the probe located directly above the molecule, we calculate a SNR of 6.32 in a 1 Hz measurement bandwidth.

Since the probe dipole is static, there is less laser heating concern with EDDI than with FDOS. The absorption of the incident light by the electret is potentially limiting at some wavelengths, but is not pursued here. In Chapter 1 we considered a micron scale

resonator with a 1.7 kHz resonance frequency possessing a force sensitivity of $5.6 \text{ aN}/\sqrt{\text{Hz}}$. [23] Such a resonator would be advantageous for EDDI detection of molecules with very small difference dipoles. Additionally, standard fiber-optic interferometry may be used to detect the mechanical motion since the dimensions of the resonator are larger than the focused laser spot size. [24]

In summary, we have explored the design details for single-molecule FDOS spectroscopy and imaging experiments. We have discussed optimizing the molecular response so that the induced dipole moment is maximized. Also, we have used the electrostatic approximation to obtain analytical formulas for the plasmon resonance condition of a metallic ellipsoidal probe particle allowing us to find the optimum aspect ratio for a specified probe material at a particular wavelength. Laser heating due to absorption in the probe is a concern and influences the design of the resonator in order to obtain as high a signal-to-noise ratio as possible. As a cautionary note, the electrostatic approximation underlies our SNR estimates of single-molecule FDOS spectroscopy and imaging experiments. To make more accurate predictions, one could simulate the optical response of the probe with finite element methods or measure the optical scattering from a single particle to determine the plasmon resonance frequency and linewidth.

Spectroscopy and imaging of a typical molecular dipole by FDOS yields quite low signal-to-noise ratios (see Figure 2.6) and thus a large amount of signal averaging is required for these experiments. However, FDOS imaging and spectroscopy of quantum dots seems promising, where a peak SNR of 0.2 in a 1 Hz measurement bandwidth and an imaging resolution of 100 nm is predicted. This suggests the use of FDOS to probe quantum confined structures such as quantum dots and quantum wells, which are finding

important technological applications. Greater generality of the method would follow from improvements in force sensitivity and heat dissipation that may come about with the development of smaller resonators.

Finally we discussed imaging and spectroscopy of single molecules that possess a difference dipole between the ground and excited state with the EDDI method. In this method, an electret probe dipole is used to sense the modulated difference dipole of the molecule. Due to the fact that the electret probe dipole is many orders of magnitude larger than the optically induced probe dipole in FDOS experiments, the EDDI method gives much larger forces on the resonator allowing faster single-molecule detection. As an example we consider detecting a single coumarin molecule with a difference dipole of 5.61 D. For this experiment, a peak signal-to-noise ratio of 3,543 in a 1 Hz bandwidth and an imaging resolution of 46 nm is predicted. Single-molecule vibrational spectroscopy seems practical at lower sensitivity.

References

1. Weissbluth, M., *Photon-Atom Interactions*. 1989, San Diego: Harcourt Brace Jovanovich.
2. Yariv, A., *Quantum Electronics*. 3rd ed. 1989, New York: John Wiley and Sons.
3. Cohen-Tannoudji, C., J. Dupont-Roc, and G. Grynberg, *Atom-Photon Interactions (Basic Processes and Applications)*. 1992, New York: John Wiley and Sons.
4. Griffiths, D.J., *Introduction to Electrodynamics*. 2nd ed. 1989, Englewood Cliffs, NJ: Prentice Hall.
5. Mie, G., *Ann Phys.*, 1908. **25**: p. 377–445.
6. Born, M. and E. Wolf, *Principles of Optics*. 7th ed. 1999, New York: Cambridge University Press.
7. Bohren, C.F. and D.R. Huffman, *Absorption and Scattering of Light by Small Particles*. 1983, New York: John Wiley and Sons.
8. Wokaun, A., J. Gordon, and P. Liao, *Radiation Damping in Surface-Enhanced Raman-Scattering*. *Physical Review Letters*, 1982. **48**(14): p. 957–960.

9. Roukes, M., *Nanoelectromechanical systems face the future*. Physics World, 2001. **14**(2): p. 25–31.
10. Craighead, H.G., *Nanoelectromechanical systems*. Science, 2000. **290**: p. 1532–1535.
11. Cleland, A.N., M. Pophristic, and I. Ferguson, *Single-crystal aluminum nitride nanomechanical resonators*. Applied Physics Letters, 2001. **79**(13): p. 2070–2072.
12. Kittel, C. and H. Kroemer, *Thermal Physics*. 1980, New York: W.H. Freeman and Co.
13. Johnson, P.B. and R.W. Christy, *Optical Constants of the Noble Metals*. Physical Review B, 1972. **6**(12): p. 4370–4379.
14. Cliffel, D.E., et al., *Mercaptoammonium-Monolayer-Protected, Water-Soluble Gold, Silver and Palladium Clusters*. Langmuir, 2000. **16**(25): p. 9699–9702.
15. Pham, T., et al., *Preparation and Characterization of Gold Nanoshells Coated with Self-Assembled Monolayers*. Langmuir, 2002. **18**(12): p. 4915–4920.
16. *Accuratus Corporation* www accuratus.com: Phillipsburg, NJ 08865.
17. Jones, D.J., et al., *Optical properties of AlN determined by vacuum ultraviolet spectroscopy and spectroscopic ellipsometry data*. Journal of Materials Research, 1999. **14**(11): p. 4337–4344.
18. Pilkey, W.D., *Formulas for Stress, Strain and Structural Matrices*. 1994, New York: John Wiley and Sons.
19. Mills, D.L., *Nonlinear optics: basic concepts*. 2nd ed. 1998, New York: Springer.
20. Silverman, K.L., et al., *Direct measurement of polarization resolved transition dipole moment in InGaAs/GaAs quantum dots*. Applied Physics Letters, 2003. **82**(25): p. 4552–4554.
21. El-Kemary, M. and W. Rettig, *Multiple emission in coumarins with heterocyclic substituents*. Phys. Chem. Chem. Phys., 2003. **5**(23): p. 5221–5228.
22. <http://physics.nist.gov/PhysRefData>.
23. Stowe, T.D., et al., *Attonewton force detection using ultrathin silicon cantilevers*. Applied Physics Letters, 1997. **71**(2): p. 288–290.
24. Rugar, D., H.J. Mamin, and P. Guethner, *Improved Fiber-Optic Interferometer for Atomic Force Microscopy*. Applied Physics Letters, 1989. **55**(25): p. 2588–2590.

Chapter 3. Optical Detection of Submicron Mechanical Resonators

In Chapter 2 we evaluated the force sensitivity for FDOS and EDDI single-molecule imaging and spectroscopy. To obtain any information from these experiments requires observation of the motion of the resonator and in this chapter we will consider optical detection via fiber-optic interferometry. Fiber-optic interferometry has been used to observe the motion of AFM cantilevers providing an unprecedented displacement sensitivity of $5.5 \times 10^{-4} \text{ \AA} / \sqrt{\text{Hz}}$ [1]. The effectiveness of this method relies on achieving a high collection efficiency of the light reflected by the resonator so that it may coherently interfere with the reference beam at the photo-detector. This method is well suited for resonators with dimensions greater than or equal to the mode diameter of the fiber-optic, which is typically a few microns. However, submicron-sized resonators will scatter light in all directions thereby diminishing the light that gets collected by the fiber. To extend the applicability of fiber-optic interferometry to submicron-scale resonators requires a scheme to enhance the scattered signal from the resonator. In this chapter we will explore plasmon enhanced fiber-optic detection of the submicron-scale resonators proposed for FDOS and EDDI imaging and spectroscopy. This method exploits the light scattering at plasmon resonance from a metallic nanoparticle attached to the mechanical resonator. Motion of the resonator modulates the phase, amplitude, or polarization of the scattered light resulting in an interference signal with a Fourier component at the mechanical resonance frequency. We will consider detecting resonators with linear and torsional modes of oscillation and compare the intrinsic Brownian noise that is encoded

into the optical signal to the shot noise of the reference field and current noise in the transimpedance amplifier.

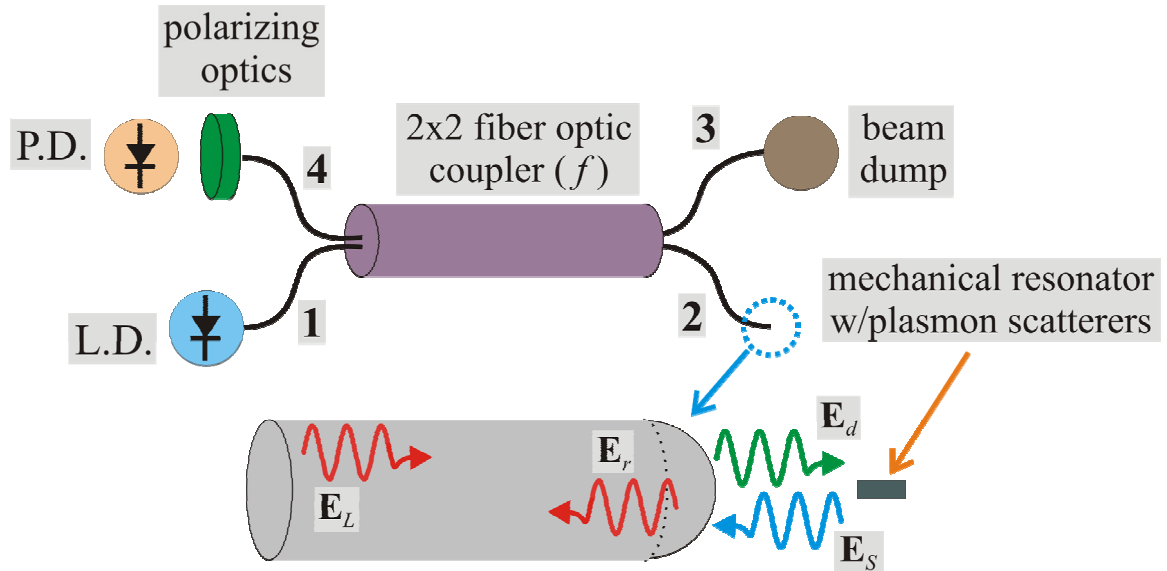


Figure 3.1: Schematic of a fiber-optic interferometer used to optically detect the motion of submicron mechanical resonators. The laser diode (L.D.) generates the detection light with power P_L at frequency ω_d , which is launched into fiber #1 of the 2x2 fiber-optic coupler. A fraction f of the initial power propagates down fiber #2 and the rest is absorbed by the beam dump. At the end of fiber #2, a reflected wave E_r is generated at the glass-air interface, which serves as the reference field of the interferometer. The transmitted field E_d is focused at the mechanical resonator by the lensed face and excites the plasmon resonance of the metallic nanoparticle attached to the resonator. The motion of the resonator results in phase, amplitude, or polarization modulation of the electric field E_s scattered by the metallic nanoparticle. The scattered field is collected by the lensed face and interferes with the reference wave at the photodiode (P.D.) to yield a photocurrent at the mechanical resonance frequency proportional to the amplitude of the mechanical motion. Inclusion of optics before optical mixing at the photodiode allows for manipulation of the polarization of the reference and scattered fields.

Figure 3.1 is a schematic of a typical fiber-optic interferometer. A diode laser launches light at frequency ω_d and with power P_L into fiber #1 of a 2x2 fiber optic coupler. A fraction f of this power is sent to fiber #2 and the other fraction $(1-f)$ is coupled to fiber #3 and absorbed by the beam dump. Fiber #2 is terminated in a lensed face where part of the incident laser field E_L is reflected back into the fiber and serves as the reference field E_r of the interferometer. The transmitted field E_d is focused by the lensed face onto the submicron mechanical resonator exciting the plasmon resonance of

the metallic nanoparticle attached to the resonator. The motion of the resonator is encoded into the phase, amplitude, or polarization of the field \mathbf{E}_s scattered by the metallic nanoparticle. A fraction of this scattered light is collected by the lensed face and travels to fiber #4 along with the reference field. Before interfering, the reference and scattered fields are transmitted through polarizing optics and then focused onto the photodiode. The Fourier component of the photocurrent at frequency ω_h is proportional to the amplitude of mechanical oscillation.

In what follows, all optical powers will be given in terms of the laser power P_L . The power P_d transmitted out of fiber #2 is

$$P_d = f(1-r)P_L, \quad 3.1$$

where r is the power reflection coefficient for the lensed face, which is taken to be 0.04.

The amplitude $|\vec{E}_d|$ of the linearly polarized detection field \mathbf{E}_d is related to this power by [2]

$$|\vec{E}_d| = \sqrt{\frac{2}{c\epsilon_0 A_d} P_d}, \quad 3.2$$

where A_d is the cross-sectional area of the beam at the focal point of the lensed face. The reference power P_r' that reaches fiber #4 is

$$P_r' = rf(1-f)P_L. \quad 3.3$$

To evaluate the scattered power collected by the lensed face, we consider the Poynting vector $\vec{S}(\vec{r})$ for the electromagnetic power radiated by the induced optical dipole of the metal nanoparticle [2]

$$\vec{S}(\vec{r}) = \frac{\omega_d^4}{32\pi^2 \epsilon_0 c^3} \frac{|\hat{r} \times \vec{p}|^2}{r^2} \hat{r}, \quad 3.4$$

where the position vector \vec{r} is measured relative to the location of the plasmon dipole and \vec{p} is its vector amplitude. The electromagnetic power crossing a differential area ΔA with normal vector \hat{n} is then given by

$$\Delta P = [\vec{S}(\vec{r}) \cdot \hat{n}] \Delta A. \quad 3.5$$

We will consider the axis of the lensed fiber to be oriented orthogonally to the dipole axis since for this geometry, the Poynting vector (and power flow) is maximized at the lensed face. Integrating equation 3.5 over a cone of angle $2\theta_a$ where θ_a is the angle of acceptance of the lensed fiber, gives the total power collected by the lensed fiber:

$$P(\theta_a) = \sigma(\theta_a) \frac{\omega_d^4 |\vec{p}|^2}{32\pi^2 \epsilon_0 c^3} \quad 3.6$$

with

$$\sigma(\theta_a) = \pi \left(\frac{4}{3} - \frac{5}{4} \cos \theta_a - \frac{1}{12} \cos 3\theta_a \right). \quad 3.7$$

Finally, the scattered power $P'(\theta_a)$ directed to fiber #4 is

$$P'(\theta_a) = (1-f)P(\theta_a). \quad 3.8$$

Detection of Linear Oscillations

We will now consider two different scattering mechanisms to detect the motion of submicron resonators possessing a linear mode of oscillation.

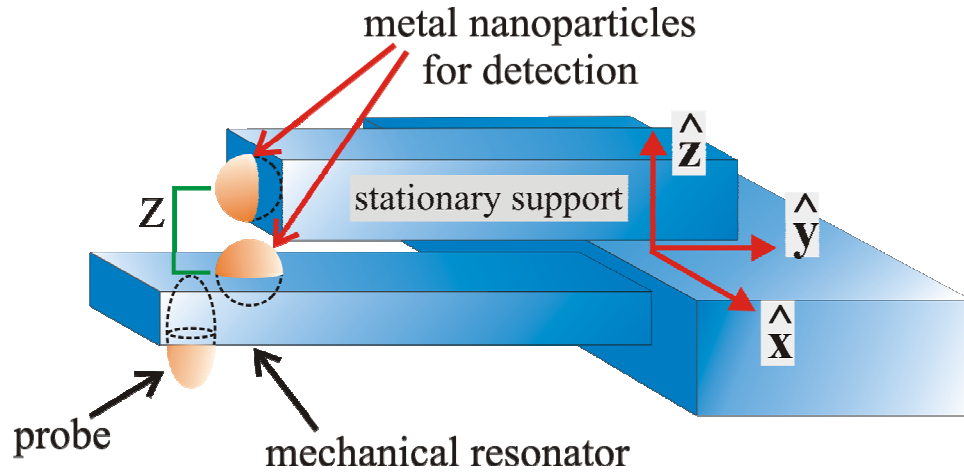


Figure 3.2: Encoding of linear mechanical oscillations through amplitude- or phase-modulated optical scattering. Two metallic spheres, both of radius R come within a few nanometers of touching. One is patterned to the top face of the resonator and the other to a stationary support above the resonator beam. The mechanical motion changes the center-to-center distance Z between the spheres, thereby modulating the amplitude of the optically induced dipole of the pair and resulting in amplitude modulation of the scattered field. A simpler scheme involves only the single sphere attached to the resonator, which simplifies the fabrication. For this case, the motion of the resonator changes the position of the sphere relative to the plane wave detection field \mathbf{E}_d , thereby modulating the phase of the induced dipole and the resulting scattered light.

Figure 3.2 shows a picture of the type of resonator considered in Chapter 2 for FDOS and EDDI. To detect the mechanical motion a metallic sphere is patterned and partially embedded in the top surface of the resonator near the free end of the beam. Directly above this, an identical sphere is embedded in a stationary support beam such that the spheres come within a few nanometers of touching. The motion of the resonator changes the center-to-center distance Z between the spheres thereby modulating the polarizability of the aggregate resulting in amplitude modulation of the scattered field.

Additionally, for the case where the top sphere and support structure are absent, a modulated signal will still exist since motion of the resonator will change the position of the sphere leading to phase modulation of the scattering, which we will discuss first.

a.) *Phase-Modulated Scattering*

For the phase modulation mechanism denoted by a subscript ϕ the dipole induced in the single metal sphere on the resonator is

$$\vec{p}_\phi(t) = \alpha_s^{R.D.} \vec{E}_d [z(t)], \quad 3.9$$

where the plane wave detection field \mathbf{E}_d is evaluated at the instantaneous position $z(t)$ of the sphere. The radiation damped polarizability $\alpha_s^{R.D.}$ of the sphere is given by [3]

$$\alpha_s^{R.D.} = \frac{\alpha_s}{\left(1 - i \frac{\omega_d^3 \alpha_s}{6\pi\epsilon_0 c^3}\right)}, \quad 3.10$$

with α_s the polarizability of the metallic sphere in the electrostatic approximation [4]

$$\alpha_s = 4\pi\epsilon_0 R^3 \left(\frac{\epsilon(\omega_d) - 1}{\epsilon(\omega_d) + 2} \right), \quad 3.11$$

where R is the radius of the sphere. Note that the plasmon resonance condition occurs when $\text{Re}[\epsilon] = -2$, which depends only on the type of metal used to fabricate the sphere.

To detect mechanical oscillations along \hat{z} we must orient the lensed fiber along this direction, therefore the functional form for the detection field is

$$\vec{E}_d(z, t) = \vec{E}_d \left(\frac{e^{i(k_d z - \omega_d t)} + e^{-i(k_d z - \omega_d t)}}{2} \right), \quad 3.12$$

where the real vector amplitude \vec{E}_d lies in the x-y plane and $k_d = 2\pi/\lambda_d = \omega_d/c$. For driving of the resonator at the resonance frequency ν_h the coordinate of the sphere is

$$z_s(t) = D + \Delta z \left(\frac{e^{i\omega_h t} + e^{-i\omega_h t}}{2} \right), \quad 3.13$$

where Δz is the amplitude of oscillation and D is the equilibrium position of the sphere measured from the face of the lensed fiber. Inserting this into equation 3.12 and assuming that $\Delta z \ll \lambda_d/2\pi$, the optically induced dipole may be written as a sum of three frequency components, $\vec{p}_\phi(t) = \vec{p}_{\phi d}(t) + \vec{p}_{\phi+}(t) + \vec{p}_{\phi-}(t)$, where

$$\vec{p}_{\phi d}(t) = \alpha_s^{R.D.} \vec{E}_d \left(\frac{e^{i(k_d D - \omega_d t)} + c.c.}{2} \right)$$

and

$$\vec{p}_{\phi\pm}(t) = \frac{\alpha_s^{R.D.} k_d \Delta z}{2} \vec{E}_d \left(i \frac{e^{i(k_d D - (\omega_d \pm \omega_h) t)} - c.c.}{2} \right). \quad 3.14$$

b.) Amplitude-Modulated Scattering

For the amplitude-modulation mechanism the axis of the lensed fiber must be oriented in the x-y plane so that the electric field vector \vec{E}_d is along \hat{z} . For this arrangement, the total dipole induced in the pair of spheres is

$$\vec{p}_A(t) = \alpha_{pair}^{R.D.} [Z(t)] \vec{E}_d(t), \quad 3.15$$

where the subscript A denotes the amplitude modulation mechanism. The electrostatic polarizability of the pair of spheres in a local field approximation is [5]

$$\alpha_{pair}(Z) = \frac{2\alpha_s [1 + \alpha_s G(Z)]}{1 - [\alpha_s G(Z)]^2}, \quad 3.16$$

where Z is the center-to-center distance between the spheres and

$$G(Z) = \frac{2}{4\pi\epsilon_0 Z^3}. \quad 3.17$$

For the time dependence given in equation 3.13, we again find that the optically induced dipole has frequency components at ω_d and $\omega_d \pm \omega_h$

$$\vec{p}_{Ad}(t) = \alpha_{pair}^{R.D.} [Z_0] \vec{E}_d \left(\frac{e^{i(k_d D - \omega_d t)} + c.c.}{2} \right)$$

and

$$\vec{p}_{A\pm}(t) = \frac{\Delta Z}{2} \frac{\partial \alpha_{pair}^{R.D.}}{\partial Z} \frac{\vec{E}_d}{Z_0} \left(\frac{e^{i(k_d D - (\omega_d \pm \omega_h) t)} + c.c.}{2} \right), \quad 3.18$$

where Z_0 is the equilibrium distance between the centers of the spheres and D is the distance from the face of the lensed fiber to the symmetry axis of the pair.

For the phase- and amplitude-modulation mechanisms, the strength of the detection field is limited by heating of the resonator. From the thermal analysis of Chapter 2 an expression was derived for the amplitude of the electric field that generates a temperature rise ΔT of the resonator:

$$|\vec{E}_d(\Delta T)| = \sqrt{\frac{2\gamma A \Delta T}{L\omega_d \text{Im}[\alpha_j^{R.D.}]}}. \quad 3.19$$

Using equations 3.2 and 3.1 we find the corresponding laser power $P_L(\Delta T)$:

$$P_L(\Delta T) = \frac{c\epsilon_0 A_d}{f(1-r)} \frac{\gamma A \Delta T}{L\omega_d \text{Im}[\alpha_j^{R.D.}]}. \quad 3.20$$

For detection of linear oscillations, the polarization of the scattered field is parallel to the reference field therefore no polarizing optics are needed after fiber # 4. The photocurrent is proportional to the square of the total electric at the photodiode, which is the sum of the signal and reference electric fields. These two fields are mixed at the photodiode to yield a dc photocurrent, which depends on the phase difference between

the two fields, and an ac photocurrent at the resonator frequency ω_h . In practice, the reference field generated by the reflection from the end of the lensed fiber will be much larger in magnitude than the scattered fields. Therefore, the main contribution to the photocurrent involves products of the form $\vec{E}_r \cdot \vec{E}_s$, where \vec{E}_r is the amplitude of the reference field at the photodiode and \vec{E}_s is the amplitude of one of the frequency components of the scattered field. After some lengthy algebra and keeping terms only of the form $\vec{E}_r \cdot \vec{E}_s$, the photocurrent $i(t)$ is expressed in terms of the reference power P_r' and the sideband power P_+' at the photodiode as [6]

$$i(t) = \frac{e\eta}{\hbar\omega_d} \left(P_r' + 2\sqrt{P_r'P_d'} \cos(\phi_d) + 4\sqrt{P_r'P_+'} \cos \omega_h t \right). \quad 3.21$$

In equation 3.21, $e = 1.61 \times 10^{-19}$ (C), is the electron charge, and η is the quantum efficiency of the photodiode, which is the probability that an absorbed photon generates a free conduction electron. Also, we have used the fact that $P_+ = P_-'$. The phase difference ϕ_d between the reference and scattered waves at frequency ω_d is

$$\phi_d = \frac{4\pi D}{\lambda_d} + \text{ArcTan} \left(\frac{\text{Im}[\alpha^{R.D.}]}{\text{Re}[\alpha^{R.D.}]} \right). \quad 3.22$$

From the second term in equation 3.21, ϕ_d is seen to modulate the dc level of the photocurrent. This interference term may therefore be used in a feedback loop to stabilize the gap between the fiber and resonator against long term drifts.

In addition to the coherently driven motion, the random thermal motion of the resonator becomes encoded as noise in the optical signal. To calculate the root-mean-square noise dipole at the ‘‘sideband’’ frequencies ($\omega_d \pm \omega_h$) we simply replace Δz and ΔZ

in equations 3.14 and 3.18 with the rms value of the amplitude fluctuations \bar{Z} . In Appendix A we derived the spectral density $\tilde{G}_z(\nu_h)$ of amplitude fluctuations at resonance. Multiplying the spectral density by the measurement bandwidth $\Delta\nu$ and taking the square root we obtain \bar{Z} :

$$\bar{Z} = \sqrt{\frac{4k_B T Q}{M \omega_h^3} \Delta\nu}. \quad 3.23$$

From the form of equation 3.21 we find the rms noise \bar{i}_B in the photocurrent due to Brownian motion of the resonator to be

$$\bar{i}_B = \frac{4e\eta}{\hbar\omega_d} \sqrt{P'_r \bar{P}'_+}, \quad 3.24$$

where \bar{P}'_+ is the rms noise power at the photodiode scattered into a single sideband.

Using equations 3.3, 3.6, and 3.8 we evaluate this noise for modulation mechanism j as

$$\bar{i}_{B,j} = \frac{4e\eta}{\hbar} \sqrt{\frac{rf(1-f)^2 \sigma(\theta_a)}{32\pi^2 \epsilon_0 c^3} P_L \omega_d |\vec{\mathcal{P}}_j|}, \quad 3.25$$

where $|\vec{\mathcal{P}}_j|$ is the rms amplitude of the induced noise dipole for the phase- ($j = \phi$) and amplitude- ($j = A$) modulation mechanisms. From equations 3.14 and 3.18 we see that this amplitude depends linearly on the magnitude of the detection field, which may be expressed in terms of the laser power using equations 3.1 and 3.2. Finally, using 3.20 and 3.23 we find the explicit expressions for the photocurrent noise due to Brownian motion for the two detection mechanisms:

$$\bar{i}_{B,\phi} = \frac{e\eta}{\pi\hbar c^2} \sqrt{\frac{r(1-f)^2 \sigma(\theta_a) A_d k_B T Q}{(1-r) M \omega_h^3} \Delta\nu} \frac{\omega_d |\alpha_s^{R.D.}| \gamma A \Delta T}{L \text{Im}[\alpha_s^{R.D.}]} \quad 3.26$$

and

$$\bar{i}_{B,A} = \frac{e\eta}{\pi\hbar c} \sqrt{\frac{r(1-f)^2 \sigma(\theta_a) A_d k_B T Q}{(1-r) M \omega_h^3}} \Delta\nu \frac{\gamma A \Delta T}{L \operatorname{Im}[\alpha_{pair}^{R.D.}]} \left| \frac{\partial \alpha_{pair}^{R.D.}}{\partial Z} \right|_{z_0}. \quad 3.27$$

Photocurrent noise due to Brownian motion of the resonator is not the only noise source in the detection scheme. We must also include shot noise (dominated by that of the reference field) and current noise in the photodiode transimpedance amplifier. In a measurement bandwidth $\Delta\nu$ the contribution of shot noise to the total noise in the photocurrent is [6]

$$\bar{i}_{shot} = \sqrt{\frac{2e^2 \eta P_r'}{\hbar \omega_d}} \Delta\nu. \quad 3.28$$

c.) Numerical Examples for Detecting Linear Oscillations

For phase-modulation detection of linear oscillations, we will use a 40 nm diameter Ag sphere irradiated at the plasmon resonance of 354 nm. For both the phase- and amplitude-modulation mechanisms, the laser power corresponding to a 1° temperature rise of the plasmon particle(s) is found from equation 3.20. The fiber-optic coupler has $r = 0.04$, $f = 0.5$, $\theta_a = 20^\circ$ [7] and the mode diameter of the laser beam at the focus is 2.5 microns.[7] The New Focus model 1801 photoreceiver with a 125 MHz bandwidth, quantum efficiency of 0.7 at 354 nm, and a noise current of 0.66 pA in a 1 Hz measurement bandwidth is assumed for detection of the reference and scattered fields.[8] In Figure 3.3a the Brownian, shot, and amplifier noise currents in a 1 Hz measurement bandwidth are plotted versus the width w of a 5 micron long AlN resonator beam of square cross-section, where a Q of 1000 is assumed at 300 K. It can be seen that

Brownian noise of the resonator is the largest component of the photocurrent noise for the range of widths plotted. The total photocurrent noise is $\bar{i}_{tot} = \sqrt{i_{B,\phi}^2 + i_{shot}^2 + i_{amp}^2}$ and for $w = 150$ nm is 1.15 pA/(Hz) $^{1/2}$, which is a factor of 1.5 times larger than the Brownian contribution at mechanical resonance. In Figure 3.3b the resonator frequency is plotted versus the width of the AlN beam and is 10 MHz for $w = 150$ nm.

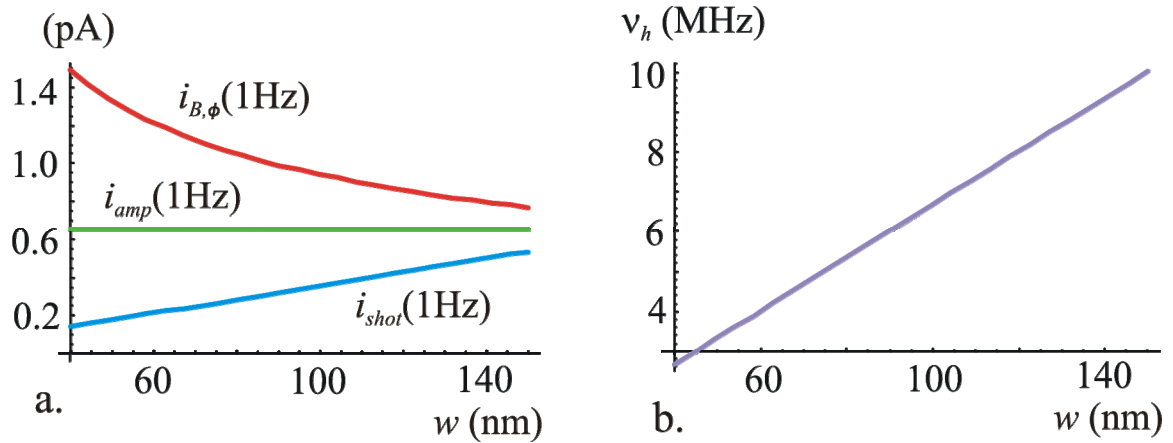


Figure 3.3: Noise contributions and resonator frequency for detection of the linear mode of mechanical oscillation of a submicron resonator via phase-modulated scattering from a 40 nm diameter silver sphere irradiated at plasmon resonance, $\lambda_d = 354$ nm. **a.** Brownian, shot, and amplifier contributions to the photocurrent noise in a 1 Hz detection bandwidth plotted versus the width w of a 5 micron long AlN resonator beam of square cross-section ($Q = 1000$ @ 300 K). **b.** The mechanical resonance frequency plotted versus the width of the beam.

For the amplitude-modulation mechanism, we consider two Ag spheres 20 nm in diameter that are separated by 2 nm at mechanical equilibrium. The plasmon resonance for this aggregate is at $\lambda_d = 368$ nm, which is also the wavelength at which the derivative $|\partial\alpha/\partial Z|_{Z_0}$ is maximized. The parameters characterizing the fiber-optic interferometer are the same as in the phase-modulation example above and the model 1801 photoreceiver [8] is again assumed for detection of the optical fields. The Brownian shot and amplifier contributions to the photocurrent in a 1 Hz measurement bandwidth are plotted in Figure 3.4a versus the beam width for a 4 micron long AlN resonator with $Q = 1000$ at 300 K.

The amplifier noise increases for higher optical modulation frequencies and has a maximum value of 4 pA [8] in a 1 Hz measurement bandwidth over the range of mechanical frequencies plotted in Figure 3.4b. For a beam width of 400 nm, the corresponding resonance frequency is 41 MHz and the total noise current is 9.8 pA which is a factor of 1.14 times larger than the Brownian contribution.

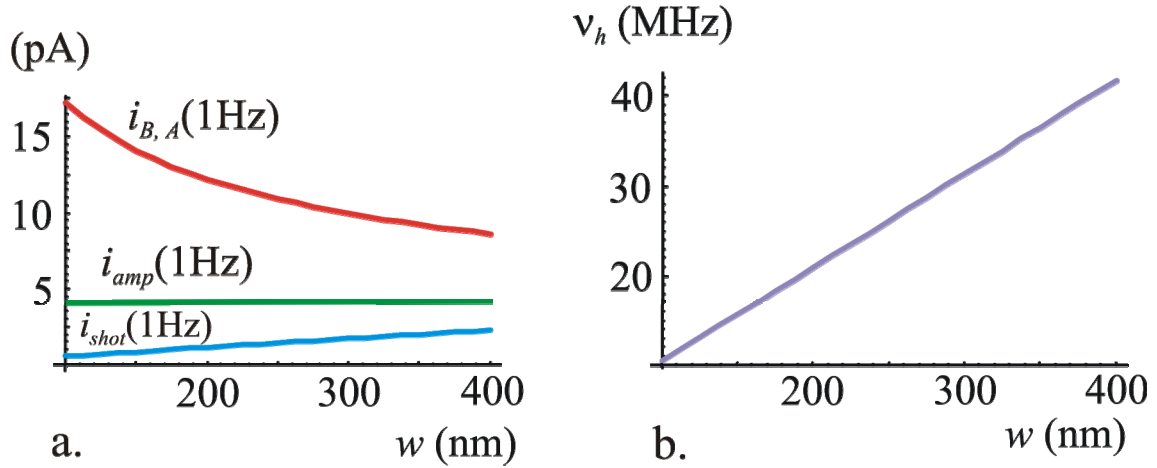


Figure 3.4: Noise contributions and resonator frequency for detection of the linear mode of mechanical oscillation of a submicron resonator via amplitude-modulated scattering from a pair of 20 nm diameter silver spheres irradiated at plasmon resonance, $\lambda_d = 368$ nm. **a.** Brownian, shot, and amplifier contributions to the photocurrent noise in a 1 Hz detection bandwidth plotted versus the width w of a 4 micron long AlN resonator beam of square cross-section ($Q = 1000$ @ 300 K). **b.** The mechanical resonance frequency plotted versus the width of the beam.

Detection of Torsional Oscillations

Shown in Figure 3.5 is a nanoscale beam of length L width w and height h possessing a fundamental mode of angular displacement $\theta(y, t)$ measured relative to the \hat{z} axis:

$$\theta(y, t) = \Delta\theta \cos(\omega_h t) \sin\left(\frac{\pi}{L} y\right). \quad 3.29$$

The amplitude of the angular displacement at the center of the beam is $\Delta\theta$ and the oscillation frequency ω_h is given by [9]

$$\omega_h = \frac{\pi}{L} \sqrt{\frac{GJ}{I_p}}, \quad 3.30$$

where G is the shear modulus (N/m^2) for the beam material and J , the torsional constant (m^4) is given by [9]

$$J = \frac{wh^3}{3} \left(1 - 0.63 \left(\frac{h}{w} \right) + 0.052 \left(\frac{h}{w} \right)^5 \right), \quad 3.31$$

where $w \geq h$. Furthermore, I_p , the polar moment of inertia per unit length ($\text{kg}\cdot\text{m}$) is

$$I_p = \frac{1}{12} \rho wh (w^2 + h^2), \quad 3.32$$

where ρ is the mass density of the material (kg/m^3).

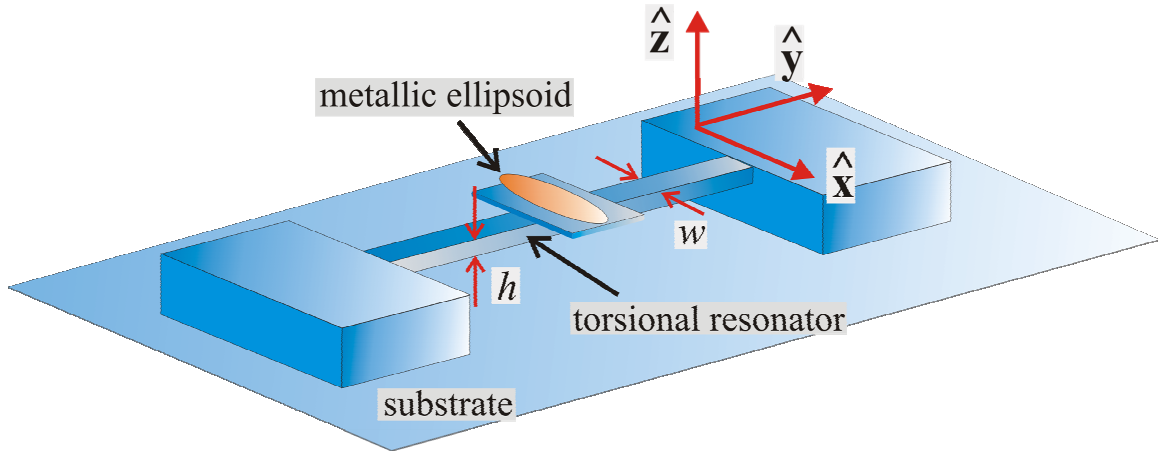


Figure 3.5: Optical detection of the torsional mode of oscillation of a submicron mechanical resonator. The wavelength λ_d of the detection field is tuned to the plasmon resonance for the long axis of the metallic nanoparticle patterned at the center of the resonator beam. The polarization of the incident field \mathbf{E}_d is oriented along the nonresonant, short axis of the particle, thereby minimizing laser heating. Torsion of the beam about \hat{y} changes the orientation of the particle relative to the polarization of the detection field, thereby inducing a dipole along the long axis of the particle with an amplitude proportional to the angle of torsion.

At the center of the beam, where the mode shape is maximum, a metallic ellipsoid is patterned on a platform with its long axis perpendicular to the beam axis. The detection light propagates along the length of the beam (\hat{y} direction) with the polarization vector oriented along the short axis of the particle (\hat{z} direction). The polarizability tensor for the metallic particle is expressed as

$$\vec{\alpha}(\theta) = \alpha_a^{R.D.} \hat{x}'\hat{x}' + \alpha_b^{R.D.} \hat{z}'\hat{z}', \quad 3.33$$

where $\alpha_a^{R.D.}$ and $\alpha_b^{R.D.}$ are the components of the polarizability tensor along the long axis and short axis, respectively. The unit vectors \hat{x}' and \hat{z}' define the principal axis system and are related to the lab frame unit vectors by

$$\begin{aligned} \hat{x}' &= \hat{x} \cos \theta - \hat{z} \sin \theta \\ \hat{z}' &= \hat{x} \sin \theta + \hat{z} \cos \theta \end{aligned} \quad 3.34$$

Using equation 3.34 we find the polarizability tensor expressed in the lab frame

$$\vec{\alpha}(\theta) \approx \alpha_a^{R.D.} (\hat{x}\hat{x} - \hat{x}\hat{z}\theta - \hat{z}\hat{x}\theta) + \alpha_b^{R.D.} (\hat{z}\hat{z} + \hat{x}\hat{z}\theta + \hat{z}\hat{x}\theta), \quad 3.35$$

where the small angle approximation has been made and terms of order θ^2 and higher are dropped. For the detection field aligned along \hat{z} we find the induced dipole to be the sum of dipoles at ω_d and $(\omega_d \pm \omega_h)$:

$$\vec{p}_{Pd}(t) = \alpha_b^{R.D.} |\vec{E}_d| \left(\frac{e^{i(k_d D - \omega_d t)} + c.c.}{2} \right) \hat{z}$$

and

$$\vec{p}_{P\pm}(t) = \frac{\Delta\alpha \Delta\theta}{2} |\vec{E}_d| \left(\frac{e^{i(k_d D - (\omega_d \pm \omega_h) t)} + c.c.}{2} \right) \hat{x}, \quad 3.36$$

where the subscript P denotes the polarization-modulation mechanism and $\Delta\alpha = \alpha_b^{R.D.} - \alpha_a^{R.D.}$. The root-mean-square noise dipole is found from equation 3.36 by replacing the driven angular amplitude $\Delta\theta$ by the rms value

$$\bar{\theta} = \sqrt{\frac{4k_B T Q}{I \omega_h^3} \Delta\nu} \quad 3.37$$

of thermal fluctuations in the angular coordinate, where $I = I_p L/2$ is the moment of inertia of the torsional resonator.

Since the scattered field is orthogonal to the reference field, it is necessary to project both fields onto a single axis so that interference may occur at the photodiode. Therefore, a linear polarizer is placed in front of the photodiode with transmission axis oriented at angle ψ with respect to the polarization direction of the reference field. With the polarizer in line, the reference power at the photodiode will be $\cos^2 \psi P_r'$ and the scattered power will be $\sin^2 \psi P'(\theta_a)$, where P_r' and $P'(\theta_a)$ were given by equations 3.3 and 3.8, respectively. Following the same steps as above and taking into account that the heat dissipation is improved by the attachment of the beam to the substrate at both ends, we arrive at the Brownian photocurrent noise for the polarization-modulation mechanism:

$$\bar{i}_{B,P} = \frac{4e\eta}{\pi\hbar c} \sqrt{\frac{r(1-f)^2 \sigma(\theta_a) \cos^2 \psi \sin^2 \psi A_d k_B T Q}{(1-r) I \omega_h^3} \Delta\nu} \frac{\gamma A \Delta T}{L \operatorname{Im}[\alpha_b^{R.D.}]} |\Delta\alpha|. \quad 3.38$$

To approach Brownian motion-limited optical detection, it is necessary to maximize the Brownian contribution to the photocurrent. From equation 3.38 we see that

the polarizer angle must be set to 45° , since this maximizes the function $\cos\psi \sin\psi$.

Finally, the shot noise contribution is found from equation 3.28 to be

$$\bar{i}_{shot} = \sqrt{\frac{2e^2 \eta r f (1-f) \cos^2 \psi P_L}{\hbar \omega_d} \Delta \nu}. \quad 3.39$$

Numerical examples for detection of torsional motion

As an example of detecting torsional motion, we consider a 5 micron long x 100 nm wide AlN beam and assume a Q of 1000 at 300 K for the torsional mode. At the center of the beam is a 20 nm wide x 83 nm long silver ellipsoid with plasmon resonance along the long axis at $\lambda_d = 549$ nm. The parameters characterizing the fiber-optic interferometer are the same as above, however the photodetector is taken to be the model 1601 by New Focus with a 1 GHz bandwidth, quantum efficiency of 0.7 at 549 nm, and current noise of 9.3 pA in a 1 Hz bandwidth.[8] The polarizer angle ψ is set to 45° , so as to maximize the Brownian photocurrent. In Figure 3.6a the Brownian and shot contributions to the photocurrent noise in a 1 Hz measurement bandwidth are plotted versus the height h of the AlN beam. For each value of the height, the laser power is adjusted so as to produce a 1° temperature rise of the resonator. For $h = 35$ nm the Brownian and shot contributions are equal with a value of 20 pA giving a total photocurrent noise of $\sqrt{2(20)^2 + (9.3)^2} = 29.8$ pA, which is a factor of 1.49 times larger than the Brownian contribution. The mechanical resonance frequency is plotted in Figure 3.6b versus the height of the beam. For $h = 35$ nm where the Brownian and shot noises are equal, the corresponding resonance frequency is 587 MHz.

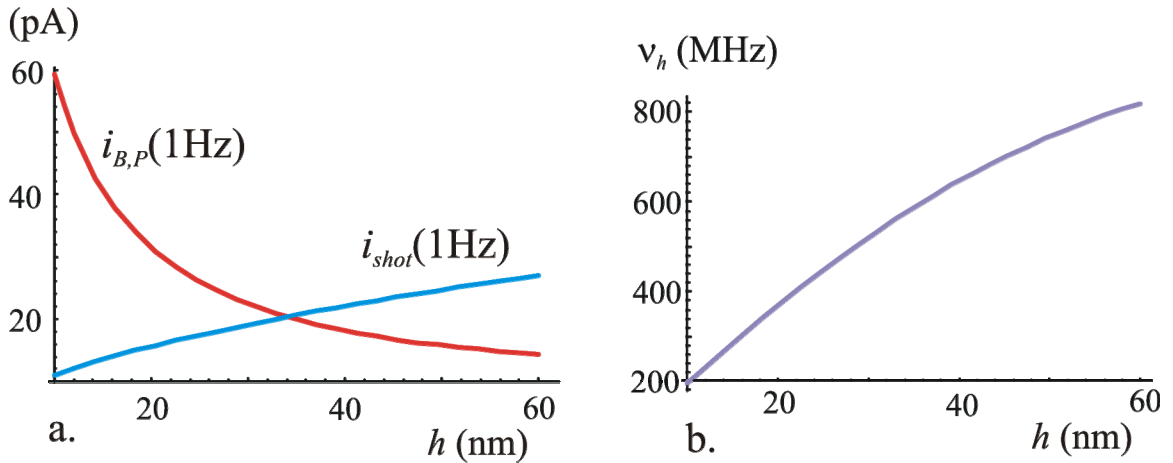


Figure 3.6: Noise contributions and resonator frequency for detection of the torsional mode of mechanical oscillation of a submicron resonator via polarization-modulated scattering from a 20 nm wide x 83 nm long silver ellipsoid irradiated at plasmon resonance, $\lambda_d = 549$ nm. **a.** The Brownian and shot contributions to the photocurrent noise in a 1 Hz bandwidth plotted against the height h of a 5 micron long x 100 nm wide AlN resonator beam ($Q = 1000$ @ 300 K). The amplifier noise of 9.3 pA is not shown since it is well below the other noise levels. **b.** The mechanical resonance frequency plotted versus the beam height h .

In conclusion, three optical scattering mechanisms have been investigated for use in enhancing interferometric detection of the motion of submicron mechanical resonators. In all of these, a metallic nanoparticle attached to the resonator is irradiated at plasmon resonance. Motion of the resonator modulates the phase, amplitude, or polarization of the plasmon dipole resulting in optical scattering at the “sideband” frequencies ($\omega_d \pm \omega_h$). A fiber-optic interferometer is used to excite the plasmon resonance and to efficiently collect the scattered light. The reference and scattered fields mix at the photodiode resulting in a photocurrent with a frequency component at the mechanical resonator frequency.

We have seen in Chapter 2 that Brownian (thermal) motion of the mechanical resonator sets a fundamental limit on how small a driven amplitude we may practically detect. In the plasmon detection schemes discussed, Brownian motion becomes encoded as an optical noise source at the sideband frequencies appearing as a source of

photocurrent noise. If the optical detection scheme were noiseless, then we would only record the optically encoded Brownian motion of the resonator. However shot noise of the reference field and electronic amplifier noise are also present and degrade the sensitivity of the optical detection scheme. Here, we have plotted the photocurrent noise versus a single geometric parameter of the mechanical resonator so as to find a range of designs for which the optical detection scheme approaches the ideal of being Brownian motion-limited. For detection of resonators with a linear mode of oscillation the phase-modulation scheme allows detection of mechanical frequencies up to 10 MHz, at which point the total photocurrent noise is a factor of 1.5 times larger than the Brownian contribution. The amplitude-modulation mechanism allows extension of this range to mechanical frequencies of about 40 MHz with the total noise at this frequency being a factor of 1.14 times larger than the Brownian noise. Finally, the polarization-modulation mechanism is quantified for detection of torsional oscillations up to approximately 600 MHz. At this upper limit, the total photocurrent noise is a factor of 1.5 times larger than the Brownian contribution.

Amplifier noise tends to get worse the higher the mechanical frequency to be detected. For example, the current noise spectral density for the New Focus model 1801 amplifier is $0.66 \text{ pA}/\sqrt{\text{Hz}}$ for frequencies below about 15 MHz and increases by about a factor of 10 at 80 MHz.[8] One way to minimize the amplifier noise is now outlined, which will allow even higher frequency detection without this noise mechanism dominating. The initial laser beam is split into two beams before launching into the fiber-optic coupler. The reference beam goes through an electro-optic modulator driven by an rf voltage at frequency δ before it impinges on the photodiode. The other beam is

launched into the coupler in the usual way and excites the plasmon resonance of the metallic nanoparticle. Interference of the scattered field and reference field will result in a Fourier component of the photocurrent at frequency $(\nu_h - \delta)$, where δ is chosen such that this difference frequency lies in a frequency range where amplifier noise is minimized. As an example, the New Focus model 2151 Femtowatt photoreceiver has a current noise of $8 \text{ fA}/\sqrt{\text{Hz}}$ and a 750 Hz bandwidth.[8] Therefore, δ is chosen to be, at most, 750 Hz away from ν_h . Another advantage of this scheme is that the strength of the reference field is not limited by laser heating therefore, a much stronger reference field may be used, which will boost the size of the Brownian contribution to the photocurrent noise.

References

1. Rugar, D., H.J. Mamin, and P. Guethner, *Improved Fiber-Optic Interferometer for Atomic Force Microscopy*. Applied Physics Letters, 1989. **55**(25): p. 2588–2590.
2. Griffiths, D.J., *Introduction to Electrodynamics*. 2nd ed. 1989, Englewood Cliffs, NJ: Prentice Hall.
3. Wokaun, A., J. Gordon, and P. Liao, *Radiation Damping in Surface-Enhanced Raman-Scattering*. Physical Review Letters, 1982. **48**(14): p. 957–960.
4. Bohren, C.F. and D.R. Huffman, *Absorption and Scattering of Light by Small Particles*. 1983, New York: John Wiley and Sons.
5. Averbukh, I.S., et al., *Coherent near field optical microscopy*. Optics Communications, 2000. **174**: p. 33–41.
6. Yariv, A., *Optical Electronics in Modern Communications*. 5th ed. 1997, New York: Oxford University Press. 744.
7. *Oz Optics Limited* www.ozoptics.com.
8. *New Focus Corp.* www.newfocus.com.
9. Pilkey, W.D., *Formulas for Stress, Strain and Structural Matrices*. 1994, New York: John Wiley and Sons.

Chapter 4. A Novel Nanoscale Device for Single-Molecule Sensing

For many biologically relevant molecules, such as proteins, the nature of the solvent environment can have dramatic effects on the three-dimensional structure of the molecule, drastically altering its biochemical functionality.[1, 2] To draw conclusions about the function of such molecules requires studying them in their native environment. In Figure 1.4 of Chapter 1, we introduced a novel electromechanical device that can non-invasively probe the structure and dynamics of single biological molecules in solution. Briefly, the device consists of a semiconductor beam with a torsional mode of oscillation about its axis at frequency ν_h . At the center of the beam a nanoscale ferroelectric particle with static dipole moment \mathbf{p} is patterned. The ferroelectric particle resides in the gap of two nearby electrodes that are used to excite the motion of the mechanical resonator, as well as to detect the decaying mechanical oscillations via the voltage induced across the electrodes. The electrostatic interaction energy between the ferroelectric dipole and a nearby molecule in solution gives rise to a shift in the frequency of the mechanical resonator. This frequency observable is dependent upon the position and orientation of the molecule with respect to the probe dipole.

In Chapter 1 we discussed how this device could be used as a single-molecule binding sensor and detailed the experimental apparatus and procedure for monitoring the shift in the mechanical resonance frequency with submillisecond resolution. In this chapter, we quantify the physics that underlies the interaction between the probe dipole and molecule. Numerical examples of the frequency shift will be given for typical

biological molecules in an aqueous environment and will be compared to the minimum detectable frequency shift that arises from the Brownian motion of the mechanical resonator. Furthermore, the electrostatic interaction between the probe dipole and the electrodes couples the electric and mechanical degrees of freedom of this device. To derive the dynamics of this device, we use Lagrange's equations for θ , the angle of torsion at the center of the beam and q , the charge on one electrode of the nanoscale capacitor. The steady state solutions to the resulting coupled differential equations are evaluated, which allows us to derive the device impedance. Impedance matching solutions are described so as to efficiently couple power to and from the device. Proposed applications of this novel device for both binding sensors and radio frequency communications will be presented.

Single-Molecule Sensor Physics

In Appendix B, we derive the electrostatic energy of interaction between the probe dipole and molecule:

$$U(\vec{r}_m; \theta) = -\frac{1}{2} \alpha_{ik} E_i(\vec{r}_m; \theta) E_k(\vec{r}_m; \theta), \quad 4.1$$

where α_{ik} are the Cartesian components of the totally symmetric molecular polarizability tensor expressed in the laboratory coordinate system. Summation over the repeated indices i and k is implied. It should be noted that the α_{ik} are implicit functions of the instantaneous orientation of the molecule since, at any instant of time, the orthogonal transformation that relates the principal axes of the molecule to the laboratory axes

depends on the Euler angles that describe the molecular orientation. Also, $E_j(\vec{r}_m; \theta)$ is the component of the electric field of the probe dipole along the j th laboratory axis, which depends parametrically on θ and is to be evaluated at the instantaneous position of the molecule \vec{r}_m .

In what follows, we will need the electric field of the probe evaluated at the center of the molecule [3],

$$\vec{E}(\vec{r}_m; \theta) = \frac{1}{4\pi\epsilon_0 r_m^3} \left[3 \left[\vec{p}(\theta) \cdot \hat{r}_m \right] \hat{r}_m - \vec{p}(\theta) \right], \quad 4.2$$

with

$$\vec{p}(\theta) = |\vec{p}| (\hat{z} \cos \theta + \hat{x} \sin \theta). \quad 4.3$$

For small angular displacements, we may expand the components of the electric field in a Taylor series out to second order in θ :

$$E_j(\vec{r}; \theta) \approx E_j(\vec{r}; 0) + \left. \frac{\partial E_j}{\partial \theta} \right|_0 \theta + \frac{1}{2} \left. \frac{\partial^2 E_j}{\partial \theta^2} \right|_0 \theta^2. \quad 4.4$$

Inserting equation 4.4 into 4.1 and keeping terms only up to second order in θ we find

$$U(\vec{r}_m; \theta) \approx -\frac{1}{2} \alpha_{ik} \left[\begin{aligned} & E_i(\vec{r}_m; 0) E_k(\vec{r}_m; 0) + \left(E_i(\vec{r}_m; \theta) \frac{\partial E_k}{\partial \theta} + E_k(\vec{r}_m; \theta) \frac{\partial E_i}{\partial \theta} \right) \Big|_0 \theta \\ & + \frac{1}{2} \left(E_i(\vec{r}_m; \theta) \frac{\partial^2 E_k}{\partial \theta^2} + E_k(\vec{r}_m; \theta) \frac{\partial^2 E_i}{\partial \theta^2} + 2 \frac{\partial E_i}{\partial \theta} \frac{\partial E_k}{\partial \theta} \right) \Big|_0 \theta^2 \end{aligned} \right]. \quad 4.5$$

The first term in equation 4.5 is a constant with respect to the mechanical coordinate and contributes nothing to the dynamics of the resonator. The second term, being linear in θ , represents a constant torque on the resonator, which simply changes the equilibrium coordinate of the resonator. The final term, being proportional to θ^2 , changes the mechanical spring constant thereby shifting the resonance frequency.

We now consider detecting a biological molecule modeled as an isotropic sphere of radius R with dimensionless dielectric constant κ immersed in an aqueous solution with dielectric constant κ_w . The molecular polarizability is given by [4]

$$\alpha = 4\pi\epsilon_0 R^3 \kappa_w \left(\frac{\kappa - \kappa_w}{\kappa + 2\kappa_w} \right). \quad 4.6$$

Using equations 4.2 and 4.3 we may find an explicit expression for the term proportional to θ^2 in the interaction energy of equation 4.5, thus

$$U(\vec{r}_m; \theta) \approx \frac{3}{2} \alpha \left(\frac{|\vec{p}|}{4\pi\epsilon_0 z_m^3} \right)^2 \theta^2. \quad 4.7$$

The interaction energy of equation 4.7 is added to the mechanical potential energy U_M :

$$U_M = \frac{1}{2} k_t \theta^2, \quad 4.8$$

to give the total electromechanical energy:

$$U_{tot} = \frac{1}{2} \left[k_t + 3\alpha \left(\frac{|\vec{p}|}{4\pi\epsilon_0 z_m^3} \right)^2 \right] \theta^2, \quad 4.9$$

where k_t (J) is the unperturbed spring constant of the torsional resonator. We identify the term in brackets in equation 4.9 as the modified spring constant \tilde{k}_t (J) of the mechanical resonator, which arises from the electrostatic coupling to the molecule:

$$\tilde{k}_t = k_t + 3\alpha \left(\frac{|\vec{p}|}{4\pi\epsilon_0 z_m^3} \right)^2. \quad 4.10$$

Furthermore, the unperturbed mechanical resonance frequency is given by

$$\nu_h = \frac{1}{2\pi} \sqrt{\frac{k_t}{I}}, \quad 4.11$$

where I ($\text{kg}\cdot\text{m}^2$) is the moment of inertia of the beam. In analogy with equation 4.11, we find the shifted frequency $\tilde{\nu}_h$ of the torsional resonator:

$$\tilde{\nu}_h = \frac{1}{2\pi} \sqrt{\frac{k_t + 3\alpha \left(\frac{|\bar{p}|}{4\pi\epsilon_0 z_m^3} \right)^2}{I}}. \quad 4.12$$

As a numerical example, we take $\kappa_w = 78$ and consider a 10 nm diameter biological molecule with $\kappa = 2$. The ferroelectric particle is taken to be a 400 nm tall x 200 nm diameter cylinder of the ferroelectric material lead zirconate titanate (PZT) with a polarization of 0.35 C/m^2 . For a 1 micron long aluminum nitride beam of rectangular cross-section, 280 nm x 200 nm, the unperturbed mechanical frequency ν_h is 950.5 MHz. This frequency results from both the elastic restoring torque and the electrostatic coupling of the ferroelectric probe with the nearby conductors, which is treated below in the Lagrangian analysis of this device. For the molecule located 100 nm away from the top surface of the ferroelectric cylinder (center-to-center distance $z_m = 300 \text{ nm}$), the shift in the mechanical frequency is calculated to be -4.23 kHz . The minimum detectable frequency shift δ in a measurement bandwidth $\Delta\nu$ is given by [5]

$$\delta = \frac{\nu_h}{2k_t} \sqrt{\frac{\tilde{G}_T(\nu_h)}{\langle \theta^2 \rangle}} \Delta\nu, \quad 4.13$$

where $\tilde{G}_T(\nu_h)$ is the spectral density of torque fluctuations on the resonator, which is derived in Appendix A and $\langle \theta^2 \rangle$ is the mean square driven amplitude of the resonator. A mechanical Q of 10,000 is assumed which sets a measurement bandwidth $\Delta\nu = \nu_h/Q$ of 95

kHz. For a driven amplitude of 1° , we have that $\langle \theta^2 \rangle = \frac{1}{2} \left(\frac{\pi}{180} \right)^2$ (rads^2) and find the

minimum detectable frequency shift to be 11.4 Hz, which gives a SNR of 370 for detecting the 4.23 kHz frequency shift due to the presence of the polarizable molecule.

Lagrangian Analysis of the Device

Due to the electrostatic coupling between the probe dipole and drive/detection electrodes, this device is a system of two coupled degrees of freedom. The dynamical nature of this device may be fully understood using Lagrange's equations. Figure 4.1 shows a side view of the device where the angle θ of torsion about the axis of the beam and the charge q on one of the electrodes are taken as the generalized coordinates, which fully specify the electromechanical configuration of the device.

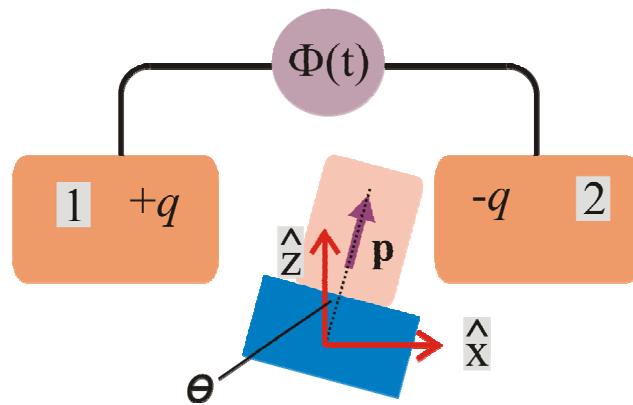


Figure 4.1: The instantaneous configuration of the device is specified by the torsional angle θ of the mechanical beam and the amount of charge q on one of the electrodes. The Lagrangian formulation for mechanical systems is then used to arrive at the two coupled differential equations for the system coordinates q and θ . The equations are solved in steady state for driving by the time harmonic voltage source $\Phi(t)$ of amplitude $\Phi(\omega)$. From this, the device impedance is found.

The Lagrangian, $\mathcal{L} = T - U$, is defined as the difference between the total kinetic energy T and total potential energy U . [6] The total potential energy is the sum of the

mechanical spring energy and the electric field energy. The electric field energy $U_E(\theta, q)$ is given by [3]

$$U_E(\theta, q) = \frac{\epsilon_0}{2} \int_{\text{all space}} d^3r \vec{E}(\vec{r}; \theta, q) \cdot \vec{E}(\vec{r}; \theta, q), \quad 4.14$$

where the electric field is a sum of three contributions:

$$\vec{E}(\vec{r}; \theta, q) = \vec{E}_q(\vec{r}; q) + \vec{E}_p(\vec{r}; \theta) + \vec{E}'(\vec{r}; \theta) \quad 4.15$$

In equation 4.15, $\vec{E}_p(\vec{r}; \theta)$ is the field of the isolated ferroelectric particle. Its functional form at large distance is the dipole field given by equation 4.2. Its value at the electrodes is evaluated numerically for a cylindrical particle using a model of uniform electric polarization. This field will induce charge redistribution on the surface of the electrodes so that the electric field is everywhere normal to the surfaces. The field generated by this induced charge is denoted $\vec{E}'(\vec{r}; \theta)$. With the dipole and conductors in electrostatic equilibrium for a given value of θ , we imagine placing an excess of charge $+q$ on one conductor and $-q$ on the other. This charge will distribute on the conductors in exactly the same configuration as if the dipole were absent, thus generating the purely capacitive field $\vec{E}_q(\vec{r}; q)$. Expanding these fields in a Taylor series out to second order in q and θ results in an electrostatic energy function of the form

$$U_E(\theta, q) = \alpha_0 + \alpha_1 q^2 + \alpha_2 q + \alpha_3 \theta q + \alpha_4 \theta + \alpha_5 \theta^2. \quad 4.16$$

The expansion coefficients will later be evaluated for a specific design using finite element simulations.

The potential and kinetic energies of the mechanical oscillator are, respectively, denoted U_M and T_M :

$$U_M = \frac{1}{2}k_t\theta^2, \quad T_M = \frac{1}{2}I\dot{\theta}^2, \quad 4.17$$

where the dot over a quantity denotes the time derivative. The effects of mechanical dissipation are included through the Rayleigh dissipation function defined as [6]

$$\mathcal{F} = \frac{1}{2}I\gamma\dot{\theta}^2, \quad 4.18$$

where $\gamma = \omega_h/Q$ is the decay rate of the total mechanical energy with ω_h the unperturbed mechanical resonance frequency and Q the quality factor. Here we have not included dissipation due to polarization currents in the conductors. This effect is modeled in Appendix C and found to be a negligible source of damping for the geometry considered.

The Lagrange equations of motion for both coordinates are [6]

$$\frac{d}{dt} \frac{\partial \mathcal{L}}{\partial \dot{\chi}} - \frac{\partial \mathcal{L}}{\partial \chi} + \frac{\partial \mathcal{F}}{\partial \dot{\chi}} = f_\chi(t), \quad 4.19$$

where $\chi = q, \theta$ and $f_q(t)$ is the externally applied voltage $\Phi(t)$, and $f_\theta(t)$ is the externally applied torque $\tau(t)$. Making use of equations 4.16, 4.17, and 4.18 we may evaluate the Lagrange equations yielding two coupled differential equations in the generalized coordinates

$$\begin{aligned} a) \quad & 2\alpha_1 q + \alpha_3 \theta + \alpha_2 = \Phi(t) \\ b) \quad & I\ddot{\theta} + I\gamma\dot{\theta} + (2\alpha_5 + k_t)\theta + \alpha_3 q + \alpha_4 = \tau(t). \end{aligned} \quad 4.20$$

For this device, the externally applied torque $\tau(t)$ is zero. Taking the voltage across the electrodes to be of the form

$$\Phi(t) = \frac{1}{2}(\Phi(\omega)e^{i\omega t} + \Phi_0 + c.c.), \quad 4.21$$

where $\Phi(\omega)$ is the amplitude of the applied voltage and Φ_0 the dc offset, the steady state solution to the differential equations above will have the form

$$\begin{aligned}
q(t) &= \frac{1}{2} \left(q(\omega) e^{i\omega t} + q_0 + c.c. \right) \\
\theta(t) &= \frac{1}{2} \left(\theta(\omega) e^{i\omega t} + \theta_0 + c.c. \right),
\end{aligned} \tag{4.22}$$

where $q(\omega)$, $\theta(\omega)$, q_0 , and θ_0 are complex numbers. Inserting these expressions into equations (4.20a and b) and setting the coefficients of like complex exponential functions equal we obtain the following four equations:

$$\begin{aligned}
a) \quad & 2\alpha_1 q(\omega) + \alpha_3 \theta(\omega) = \Phi(\omega) \\
b) \quad & \left(-I\omega^2 + iI\gamma\omega + (2\alpha_5 + k_t) \right) \theta(\omega) + \alpha_3 q(\omega) = 0 \\
c) \quad & 2\alpha_1 q_0 + \alpha_3 \theta_0 + \alpha_2 = \Phi_0 \\
d) \quad & (2\alpha_5 + k_t) \theta_0 + \alpha_3 q_0 + \alpha_4 = 0.
\end{aligned} \tag{4.23}$$

Solving equations 4.23 for the amplitudes $q(\omega)$ and $\theta(\omega)$ we find

$$\begin{aligned}
a) \quad q(\omega) &= \frac{\left[(2\alpha_5 + k_t) - I\omega^2 + iI\gamma\omega \right]}{\left[2\alpha_1 \left[(2\alpha_5 + k_t) - I\omega^2 + iI\gamma\omega \right] - \alpha_3^2 \right]} \Phi(\omega) \\
b) \quad \theta(\omega) &= \frac{-\alpha_3}{\left[2\alpha_1 \left[(2\alpha_5 + k_t) - I\omega^2 + iI\gamma\omega \right] - \alpha_3^2 \right]} \Phi(\omega).
\end{aligned} \tag{4.24}$$

We may also solve for q_0 and θ_0 , but they will be of no consequence in what follows. The electrical impedance of the device is defined as $Z(\omega) = \Phi(\omega) / \dot{q}(\omega)$ and from equation 4.22 we see that $\dot{q}(\omega) = i\omega q(\omega)$. Therefore we find

$$Z(\omega) = \frac{\alpha_3^2 \gamma}{I \left((\omega_a^2 - \omega^2)^2 + (\gamma\omega)^2 \right)} - i \frac{1}{\omega C} \frac{(\omega_r^2 - \omega^2)(\omega_a^2 - \omega^2) + (\gamma\omega)^2}{(\omega_a^2 - \omega^2)^2 + (\gamma\omega)^2}, \tag{4.25}$$

where $\omega_r = \sqrt{\frac{k_t' - C\alpha_3^2}{I}}$ and $\omega_a = \sqrt{\frac{k_t'}{I}}$ with $k_t' \equiv k_t + 2\alpha_5$ and $C = 1/(2\alpha_1)$ is the

capacitance of the electrodes. Later, we will see that at the frequency ω_r , the device impedance is minimized and at the frequency ω_a , it is maximized. In analogy to the

internal motion of piezoelectric crystals ω_r is called the resonance frequency and ω_a is the anti-resonance frequency.[7]

The impedance function derived above neglects the possible dielectric response of the ferroelectric particle. We will now give arguments for why this is a reasonable approximation. For simplicity, let us consider the electrodes to approximate a parallel plate capacitor so that the field \mathbf{E}_q is uniform and points along the \hat{x} direction in Figure 4.1. For a spherical ferroelectric particle with an isotropic dielectric tensor, the induced polarization will lie along the direction of \mathbf{E}_q and will be independent of θ . The torque on the particle is $\vec{p} \times \vec{E}_q$, where \vec{p} is the total dipole moment of the particle (ferroelectric + induced). Since the induced dipole is always parallel with \mathbf{E}_q the only contribution to the torque is from the ferroelectric dipole.

One effect of the dielectric response will be to increase the static capacitance and, from equation 4.25, this will simply decrease $\text{Im}[Z(\omega)]$ and lower the resonance frequency. For the case of a material with an anisotropic dielectric tensor or anisotropy due to a nonspherical shape, the first-order correction will be a capacitance that is a function of θ . Making a Taylor expansion in θ of the capacitance introduces higher order terms proportional to $q^2\theta$, $q^2\theta^2$, etc., ... in the energy function $U_E(\theta, q)$ and for small displacements, these terms will be negligible.

As a final reason for neglecting the dielectric response of the electret, bulk ferroelectric materials consist of a large number of regions called domains in which the polarization is uniform. The polarization from domain to domain is oriented in different directions resulting in a macroscopic, average dipole moment of zero. Upon application of an electric field, the polarization in each domain will feel a torque and tend to align

along the field direction resulting in a large dielectric response.[8] For the proposed device, however, the polarization of the ferroelectric nanoparticle is established by application of an intense electric field and, since the particle is of nanoscale dimensions, it may only contain one or a few domains. Therefore, the dielectric response at zero applied field will be much smaller than in a bulk ferroelectric.

Another effect in bulk ferroelectrics that becomes less problematic for nanoscale structures is that charge impurities in the lattice will migrate in the field of the static dipole and tend to cancel it out.[9] As an example, we consider a cylinder of ferroelectric material with radius r height h and fixed aspect ratio $\zeta = h/(2r)$. If the impurity density is denoted by η then the total number of impurity charges is $n_{impurity} = \pi r^2 h \eta = 2\pi r^3 \zeta \eta$. The total number of bound surface charges on the top face is $n_{bound} = P\pi r^2/e$ where P is the polarization of the cylinder and e the electron charge. The ratio $n_{impurity} / n_{bound} = 2e\zeta\eta r/P$ scales as r . Therefore, for some small enough sized cylinder the impurity charge will be negligible. For a 200 nm diameter by 400 nm tall PZT cylinder where $P = 0.35 \text{ C/m}^2$ there are 69,000 positive, bound charges on the top face of the cylinder. For an impurity density of $\eta = 10^{17}/\text{cm}^3$ (a relatively high impurity concentration), there will be about 1,300 impurity charges giving $n_{impurity} / n_{bound} = 0.02$. Therefore even for this high impurity level, the bound charges dominate the impurity charges at this size. This scaling argument shows why nanoscale devices can make use of the permanent electric dipole of ferroelectric crystals, a property that is not stable at larger scale, due to impurity motion. However, poling of the electrically neutral crystal to establish the static dipole must be done in vacuum and the device must remain in an evacuated environment to increase its

lifetime between poling operations, since charged particulates in the air will stick to the ferroelectric nanoparticle and cancel out the net dipole moment over time.

Finite-Element Device Simulations

The finite-element electrostatic simulation program *Maxwell 3D* [10] was used to simulate the device shown in Figure 4.2. The device geometry consists of a 200 nm in diameter x 400 nm tall PZT cylinder centered on a 1 micron long x 280 nm wide x 200 nm thick AlN beam. For this beam, $k_t = 5.77 \times 10^{-10}$ (J) and $I = 1.06 \times 10^{-29}$ (kg·m²), which gives an unperturbed mechanical resonance frequency of 1.18 GHz.

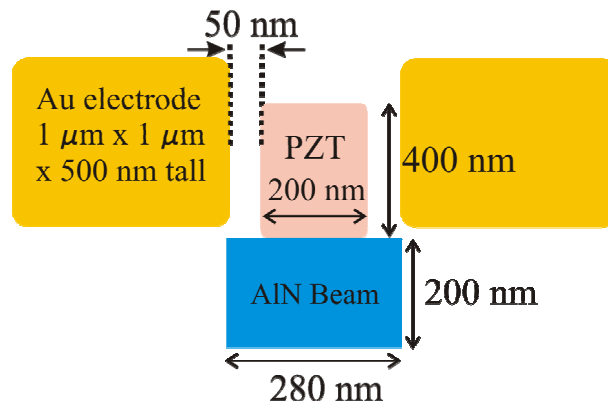


Figure 4.2: Dimensions of the device simulated by the finite element, electrostatics program *Maxwell 3D* [10]. The resonator is a 1 micron long AlN beam clamped at both ends to the substrate with a rectangular cross-section 280 nm wide x 200 nm tall. The ferroelectric cylinder measures 400 nm tall x 200 nm in diameter models polarized PZT. At mechanical equilibrium, there is a 50 nm gap between each gold electrode and the ferroelectric cylinder.

In what follows, we will assume the device to have a mechanical Q of 10,000 giving a damping rate of $\gamma = 7.39 \times 10^5$ (s⁻¹). The gold electrodes are 1 μm x 1 μm x 500 nm tall and are symmetrically arranged about the PZT cylinder. At $\theta = 0$ degrees, the electrode-to-PZT gap is 50 nm on each side. The PZT cylinder was modeled as two circular disks

of equal and opposite charge separated by 400 nm. The corresponding surface charge is $\pm 1.1 \times 10^{-14}$ C on the upper/lower surface of the cylinder respectively.

Because of the symmetrical nature of this geometry, it can be shown that the expansion coefficients, α_2 and α_4 of $U_E(\theta, q)$, are identically zero. The remaining coefficients were found via the numerical simulations. Since α_1 is simply related to the capacitance of the electrodes with the ferroelectric absent, we numerically solve for the field energy of the isolated electrodes with a charge of 1×10^{-14} C on one electrode and an equal but opposite amount of charge on the other. To find the other coefficients, we numerically solve for the field energy with different combinations of q and θ . The size of the boundary box where the electric potential is set to zero was made large enough so that negligible error was introduced into the numerical estimates of the coefficients.

Table 4.1 displays the numerical values of the field energy for different values of q and θ along with the least-squares fit for the expansion coefficients of the electric potential energy $U_E(\theta, q)$.

Simulation Conditions	Simulated Electrostatic Energy (J)
Electrodes with no PZT, $q = 1 \times 10^{-14}$ C	7.698×10^{-13}
$q = 0$ C, $\theta = 0$ degree	1.182×10^{-11}
$q = 0$ C, $\theta = 1$ degree	1.179×10^{-11}
$q = 1 \times 10^{-14}$ C, $\theta = 1$ degree	1.260×10^{-11}
$q = 1.5 \times 10^{-14}$ C, $\theta = 2$ degree	1.355×10^{-11}
Least-Squares Fit to Expansion Coefficients	
$\alpha_0 = 1.18 \times 10^{-11}$ J, $\alpha_1 = 7.70 \times 10^{-15}$ J/C ² , $\alpha_3 = 225$ J/C, $\alpha_5 = -9.84 \times 10^{-11}$ J	

Table 4.1: A compilation of the simulation conditions and the corresponding electrostatic energies found by finite-element calculations along with the least-squares fit to the expansion coefficients in equation 4.16.

Using the expansion coefficients of Table 4.1 in equations 4.24a and b we may plot the response of the system coordinates versus the driving frequency. In Figure 4.3a, the magnitudes of the electric current and amplitude of the mechanical resonator are plotted as functions of the driving frequency for $\Phi(\omega) = 1$ mV. A resonance in both the

current and torsional amplitude occurs at 950.5 MHz, which corresponds to the resonance frequency for this device.

The phases of the current and angular amplitude are plotted in Figure 4.3b. The torsional coordinate θ is in phase with the driving voltage below the resonance frequency and goes -90 degrees out of phase at ν_r , as expected for a harmonic oscillator. Due to the electromechanical coupling, however, the behavior of θ deviates from the harmonic oscillator where, slightly above ν_r , the phase undergoes an abrupt change to $+90$ degrees and approaches 0 degrees for frequencies well above resonance. In contrast, the phase for a harmonic oscillator is continuous as one sweeps through resonance and approaches -180 degrees for frequencies well above resonance.

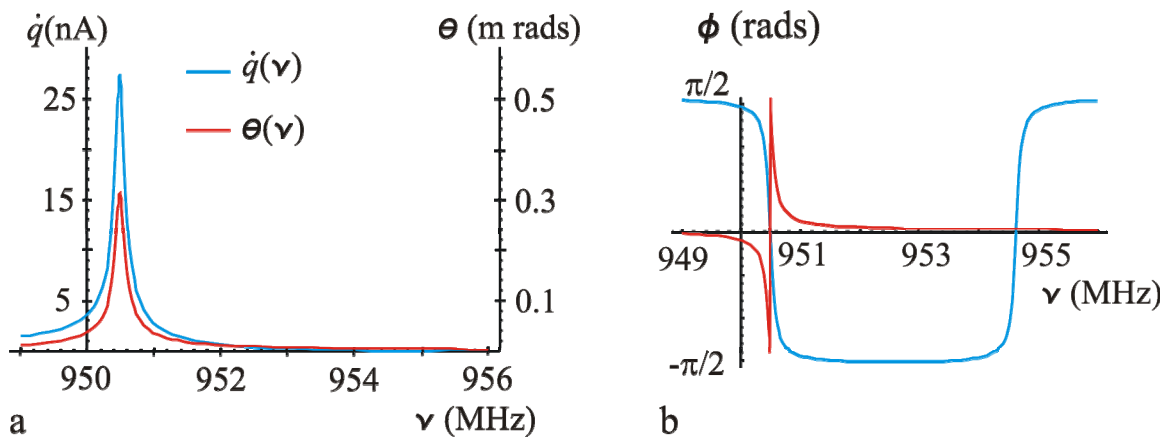


Figure 4.3: **a.** The magnitude of the electric current and angular amplitude for the simulated device plotted versus the frequency of the driving voltage. The driving voltage $\Phi(\omega)$ was set constant at 1 mV. Both the current and mechanical coordinate have a resonance at $\nu_r = 950.5$ MHz. **b.** The phase of the electric current and mechanical coordinate plotted versus the driving frequency.

In a similar manner, the current is 90 degrees out of phase with the driving voltage for frequencies below ν_r , which is characteristic of a capacitor. Above resonance, the phase of the current shifts 180 degrees and thus the device appears inductive. Finally, the current undergoes another 180 degree phase shift at approximately 954.6 MHz, which corresponds to the anti-resonance frequency for the device.

In Figure 4.4, the real and imaginary parts of the electrical impedance of the device are plotted. At the anti-resonance frequency, the impedance is maximum and undergoes an abrupt phase shift. For both the molecular sensor and radio frequency filter and oscillator applications, the device is operated near the resonance frequency where the magnitude of the impedance is minimized. The inset shows a magnified view of the impedance near resonance where, at resonance, the imaginary part is zero and the real part is 36.6 k Ω .

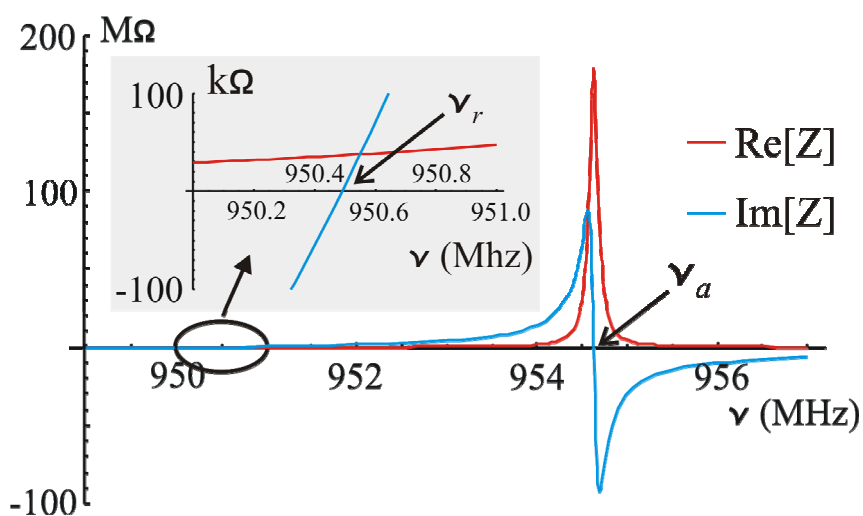


Figure 4.4: The real and imaginary parts of the electrical impedance Z for the simulated device as a function of driving frequency. At the resonance frequency, the imaginary part is zero and the real part is approximately 37 k Ω . The magnitude of the impedance is maximized at the anti-resonance frequency. For both the molecular sensor and electrical filter applications, the device is operated at the resonance frequency.

In addition to molecular sensing, this device has potential uses as a resonant element in radio frequency electronic transmitters and receivers. Due to the narrowband electrical response at ν_r , one may envision replacing bulky quartz oscillators and high-loss LC filters with this nanoscale device resulting in lower mass and lower power electronic modules ideal for portable communications and military and space applications. In order to function as a useful electronic element, the high device

impedance requires transformation into the characteristic impedance of the antenna or other waveguide structures to which it is connected. Also, as discussed in Figure 1.5, when used as a molecular sensor, impedance matching to the transmission line is necessary so as to efficiently couple power into and out of the device. We therefore turn to the important problem of matching the device impedance to a transmission line with characteristic impedance Z_0 . To effect this transformation we consider using the “T” network shown in Figure 4.5, which is adapted from reference [11].

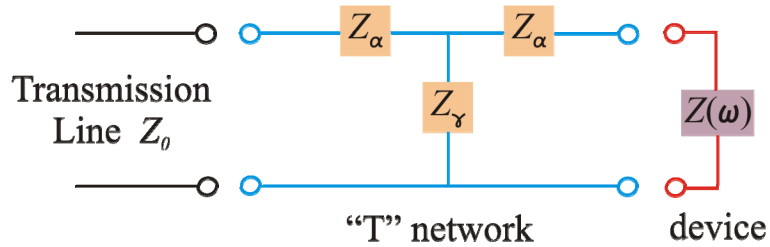


Figure 4.5: In order to efficiently couple electric power to and from the device requires transforming the device impedance into the characteristic impedance of the transmission line that drives it. To effect this transformation, we consider using the “T” network shown above. It consists of three purely reactive elements, two with impedance Z_α and the third with impedance Z_γ where $Z_\gamma = Z_\alpha^*$.

The impedance Z_{tot} seen from the transmission line is

$$Z_{tot}(\omega) = Z_\alpha + \frac{Z_\gamma [Z_\alpha + Z(\omega)]}{Z_\gamma + Z_\alpha + Z(\omega)}, \quad 4.26$$

where Z_α and Z_γ are purely reactive and $Z_\alpha = Z_\gamma^*$. To match to the characteristic impedance Z_0 of the line we must have $Z_{tot}(\omega_r) = Z_0$. Thus we find the condition at resonance to be

$$|Z_\gamma|^2 = Z_0 Z(\omega_r). \quad 4.27$$

We will take the solution $Z_\gamma = i\sqrt{Z_0 Z(\omega_r)}$ so that Z_γ corresponds to an inductor and Z_α corresponds to a capacitor. At resonance, the device impedance has the purely

resistive value of 36.6 k Ω and taking $Z_0 = 50$ ohms (e.g., standard BNC cable) we find that $Z_\gamma = i(1352) \Omega$. This corresponds to a 0.226 μ Henry inductor and a 0.124 pF capacitor at the resonance frequency of 950.5 MHz. For a commercially available surface mount inductor the resistance at 900 MHz is 56 Ω [12] and is included in series with the inductor. The “T” network expressed with lumped elements is shown in Figure 4.6.

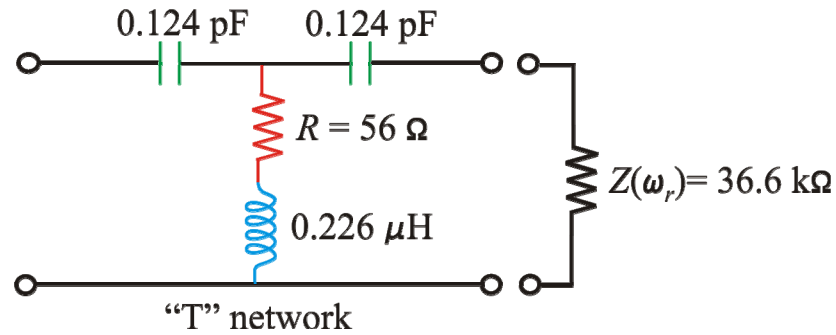


Figure 4.6: The components of the “T” network for matching the 36.6 k Ω device impedance at $\nu_r = 950.5$ MHz to a transmission line with a characteristic impedance of 50 Ω . The 56 Ω resistor accounts for the losses in the matching inductor at this frequency.

We now would like to evaluate the performance of this matching network in terms of power transfer efficiency to the device. From the differential equations describing transmission lines, the steady-state voltage $V(x,t)$ and current $I(x,t)$ at position x along the line at time t may be written

$$V(x,t) = \frac{\tilde{V}(x,\omega)e^{i\omega t} + c.c.}{2} \quad \text{and} \quad I(x,t) = \frac{\tilde{I}(x,\omega)e^{i\omega t} + c.c.}{2}, \quad 4.28$$

where

$$\tilde{V}(x,\omega) = V_+e^{-i\beta x} + V_-e^{i\beta x} \quad \text{and} \quad \tilde{I}(x,\omega) = \frac{V_+e^{-i\beta x} - V_-e^{i\beta x}}{Z_0}, \quad 4.29$$

and $\beta = \omega\sqrt{\bar{L}\bar{C}}$ where \bar{L} and \bar{C} are, respectively, the inductance and capacitance per unit length of the line.[13] The complex amplitudes V_+ and V_- describe voltage waves

traveling toward and away from the matching network, respectively, and are fixed by the boundary conditions at the two ends of the line. At $x = 0$, where the network is connected to the line, the familiar relation between voltage and current is $\tilde{V}(0, \omega) = Z_{tot}(\omega)\tilde{I}(0, \omega)$. Using equation 4.29 and defining the voltage reflection coefficient, $\Gamma(\omega) = V_-/V_+$, we find

$$\Gamma(\omega) = \frac{\bar{Z}_{tot}(\omega) - 1}{\bar{Z}_{tot}(\omega) + 1}, \quad 4.30$$

where $\bar{Z}_{tot}(\omega) = Z_{tot}(\omega)/Z_0$. Using Kirchoff's rules we find the complex power that flows from the transmission line as

$$P_{trans}(\omega) = \frac{\tilde{V}(0, \omega)\tilde{I}^*(0, \omega)}{2} = P_+ \left(1 - |\Gamma(\omega)|^2 + 2i \operatorname{Im}[\Gamma(\omega)] \right) \quad 4.31$$

and the complex power that flows into the device as

$$P_{device}(\omega) = P_+ \left| \frac{Z_\gamma(\omega)}{Z_\gamma(\omega) + Z_\alpha(\omega) + Z(\omega)} \right|^2 \left(1 + |\Gamma(\omega)|^2 - 2 \operatorname{Re}[\Gamma(\omega)] \right) \frac{Z(\omega)}{Z_0}, \quad 4.32$$

where P_+ , the total power propagated down the transmission line, is given in terms of the amplitude V_+ by

$$P_+ = \frac{|V_+|^2}{2Z_0}. \quad 4.33$$

Taking the real part of equations 4.31 and 4.32 gives the time-averaged electric power dissipated as heat, which is the relevant quantity when analyzing for the steady-state power transfer efficiency. The imaginary part indicates the time-averaged amount of stored electric vs. magnetic energy, which is not of interest here.[13]

For the network of Figure 4.6, we plot in Figure 4.7 the fraction of the incident power P_+ that is transmitted (equation 4.31) and the fraction that is transmitted to the device (equation 4.32). At the resonance frequency of 950.5 MHz, most of the incident power is transmitted with approximately 13% reflected back toward the excitation source. At resonance, approximately 40% of the incident power is delivered to (and dissipated in) the device. Off resonance the transmitted power is nearly 100% and is due to the fact that the 56 ohm resistance of the matching inductor nearly matches the characteristic impedance of the line.

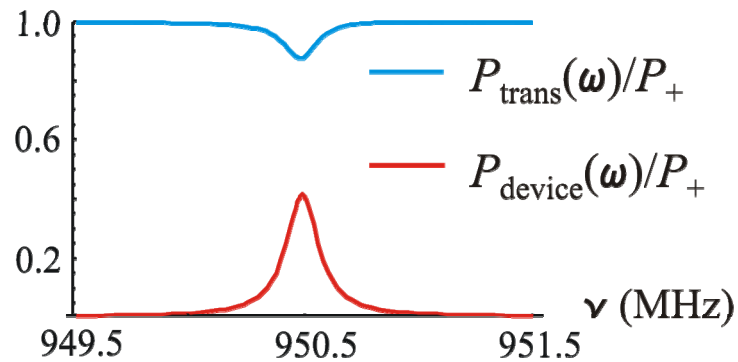


Figure 4.7: Power transfer efficiency for the matching network of Figure 4.6. At the resonance frequency of 950.5 MHz approximately 40% of the incident power P_+ is delivered to the device and 13% is reflected back toward the voltage source. The remaining 47% is dissipated in the 56 Ω resistor in series with the inductor.

For the molecular sensor application, the matching network of Figure 4.6 is used in both the excitation and detection of the motion of the mechanical resonator (see Figure 1.5). Therefore, we need to evaluate the power coupling efficiency from the device to the voltage amplifier at the other end of the line. To do this, one uses Kirchoff's laws to find the voltage and current at the input to the amplifier, which is assumed to have an input impedance of Z_0 . We will not reproduce the lengthy calculation here; however, it turns out that nearly 50% of the power generated by the device is delivered to the amplifier and the rest is absorbed by the resistance of the matching inductor. The power transfer is

better in the reverse direction because a reflected wave does not exist at the impedance-matched input to the amplifier.

In one implementation of this device as a band-pass filter in radio frequency communications, an array of devices each with a different resonance frequency would be used so as to span a particular communications band. Then, to access a particular channel in this band, the resonator corresponding to the frequency of the channel would be switched in line with the antenna and subsequent amplifiers. In order to reap the benefits of the ultrasmall mass of these devices, it is necessary to match as many of the elements in the array as possible with the same network. The network of Figure 4.6 is optimized for maximum power transfer to a device with a resonance frequency of 950.5 MHz. In Figure 4.8, the power transfer characteristics of this network are evaluated for devices with resonance frequencies lying in a 30 MHz band centered at 950 MHz. For a single device connected to the network, we evaluate at the resonance frequency the fractional power, $P_{trans}(\omega_r)/P_+$, transmitted from the line and the fractional power, $P_{device}(\omega_r)/P_+$, delivered to the device. These two quantities are plotted in Figure 4.8 as a function of the resonance frequency of the device. Over the 30 MHz band, the power transferred to the device is fairly flat and for a device with a 935 MHz resonance frequency, the power transfer is reduced by 11% relative to a device with a resonance frequency of 950.5 MHz. Additionally, at the extremes of this band, the power reflected from the network is only 8% higher relative to the power reflected for a device at 950.5 MHz.

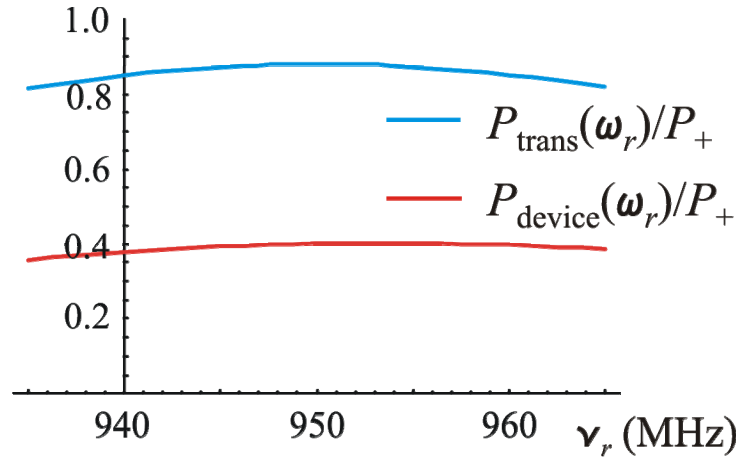


Figure 4.8: For a single device connected to the network of Figure 4.6, the fractional power transmitted (blue curve) and fractional power delivered to the device (red curve), evaluated at the resonance frequency of the device, are plotted versus ν_r .

In conclusion, we have proposed a novel, nanoscale, electromechanical device for noninvasive probing of single molecules in their native environments. One important use of this device is toward the study of the kinetics of the binding/unbinding of a single biological molecule to its corresponding receptor molecule as illustrated in Figure 1.4. The experimental observable is the shift in the mechanical resonance frequency due to the presence of the nearby polarizable molecule. For a fairly large biomolecule, 10 nm in diameter in aqueous solution, a frequency shift of 4.23 kHz is predicted for the molecule situated 100 nm from the top surface of the ferroelectric probe. Brownian noise sets a limit on how small of a frequency shift may be observed, and for the 950.5 MHz torsional resonator described above, the minimum detectable frequency shift is 11.4 Hz, where the measurement bandwidth is taken to be the natural bandwidth of the resonator. This yields an experimental signal-to-noise ratio of 370, which is more than adequate to detect individual binding events on the millisecond time scale typical of reversible recognition chemistry. Since the frequency shift scales with the volume, smaller proteins will also be accessible.

This device is a coupled electromechanical system, the dynamical nature of which may be understood using the Lagrange formulation of mechanical systems. Taking the coordinates to be q , the charge on a single electrode and θ , the angle of torsion of the mechanical resonator, we solve the resulting coupled differential equations for the behavior of these variables for steady-state driving at frequency ω . Finite element electrostatic simulations were performed for a concrete device geometry and at the resonance frequency of 950.5 MHz it is found that both the current and angular amplitude display resonant behavior. Additionally, the electrical impedance of this device is purely real at the resonance frequency and has a value of 36.6 k Ω . Due to its narrowband electrical response near resonance, this device may be used as an electrical filter/oscillator in radio frequency communications architectures. However, the large device impedance at resonance is far from the characteristic impedances of rf transmission lines and antennas, which lie in the range of $\sim 50\text{--}300 \Omega$. For maximum power transfer to and from the device, it is necessary to match the device impedance to the characteristic impedance of the waveguide or antenna to which it is attached. Impedance matching is also an issue for the device being used as a molecular sensor since power is delivered to and from it via a waveguide. A low loss “T” network consisting of two capacitors and one inductor allows for a reasonable power transfer of about 40% to the device from the waveguide. This network is capable of matching devices with resonance frequencies spread out over a bandwidth of 30 MHz centered at 950 MHz with at most 11% reduction in power transfer. This is useful for implementation in low-mass rf architectures where multiple resonators whose resonance frequencies span the band are matched to the line by the same network.

The strategy of coupling many active devices to a single transceiver is highly relevant in the context of binding sensor applications, allowing many distinct devices (possibly with different molecule-specific binding sites) to be simultaneously excited and detected with a single rf transceiver. In effect, the array associates with each binding site a unique, spectrally resolved rf channel. Accessing many channels with a single broadband transceiver reduces the parts count dramatically, while allowing simultaneous measurement of many devices. This is a fundamental advantage over proposals for electrical detection of binding by quasi-dc resistance or voltage changes induced by binding to electrical nanodevices. In contrast to the present proposal, these low frequency methods require separate detection electronics for each sensor being simultaneously observed.

As a final note, in the above analysis we considered a specific resonator with a 950.5 MHz resonance frequency; however, the equations in this chapter are general and may be applied to torsional resonators with arbitrary resonance frequencies.

References

1. Onufriev, A., D.A. Case, and D. Bashford, *Structural Details, Pathways, and Energetics of Unfolding Apomyoglobin*. *Journal of Molecular Biology*, 2003. **325**: p. 555–567.
2. Jamin, M., et al., *Submillisecond Unfolding Kinetics of Apomyoglobin and its pH 4 Intermediate*. *Journal of Molecular Biology*, 1999. **292**: p. 731–740.
3. Griffiths, D.J., *Introduction to Electrodynamics*. 2nd ed. 1989, Englewood Cliffs, NJ: Prentice Hall.
4. Bohren, C.F. and D.R. Huffman, *Absorption and Scattering of Light by Small Particles*. 1983, New York: John Wiley and Sons.
5. Sidles, J.A., et al., *Magnetic resonance force microscopy*. *Reviews of Modern Physics*, 1995. **67**(1): p. 249–265.

6. Goldstein, H., *Classical Mechanics*. 2nd ed. 1980, Menlo Park, California: Addison Wesley. 672.
7. Mason, W.P., *Piezoelectric crystals and their application to ultrasonics*. 1950, New York: Van Nostrand.
8. Zaky, A.A. and R. Hawley, *Dielectric Solids*. 1970, New York: Dover. 106.
9. Guinier, A. and R. Jullien, *The Solid State*. 1989, New York: Oxford University Press. 271.
10. Ansoft Corporation, *Maxwell 3D v.10* www.ansoft.com.
11. Collin, R.E., *Field Theory of Guided Waves*. 2nd ed. 1991, New York: IEEE Press.
12. Coilcraft Inc. www.coilcraft.com: Cary, IL.
13. Adler, R.B., L.J. Chu, and R.M. Fano, *Electromagnetic Energy Transmission and Radiation*. 1960, New York: John Wiley and Sons. 621.

Chapter 5. Experimental Apparatus

In this chapter we will discuss experimental work toward optical detection of nanoscale mechanical resonators using a home-built fiber-optic interferometer apparatus. Figure 5.1 shows a detailed picture of the instrument, which comprises a precision, motorized x-y translation stage that is bolted to a mechanically stiff, stainless steel frame. Directly above this, a z-translation stage, used for vertical positioning of the detection fiber-optic, is bolted to the top plate of the frame. A 1.5 in. x 1.5 in. square access hole is milled out of the top plate, allowing the fiber to reach the device chip and providing reasonable visual access of the fiber-sample region. Attached to the x-y stage is a rectangular, aluminum frame whose top surface is a thin plate. Fine vertical control of the sample position is effected by a piezoelectric actuator centered inside of this frame. The actuator fits snugly inside the frame, and when a voltage is applied to the piezoelectric, a force is generated on the thin plate, creating a slight mechanical deformation in the vertical direction. The device chip is glued to a second piezoelectric, which is attached to the top surface of this plate. This second actuator is used to excite the mechanical motion of the submicron resonators fabricated on the device chip. The stainless steel frame sits on the top of an aluminum baseplate. Several holes are drilled in the baseplate to accommodate O-ring sealed, vacuum feedthroughs. A 12 inch diameter, O-ring sealed, glass bell jar encloses the volume occupied by the steel frame and feedthroughs, so that the entire apparatus may be operated in an evacuated environment ranging from milli-torr down to microtorr pressures. The two surfaces of the baseplate are polished in the regions where O-ring seals exist in order to ensure leak-free operation.

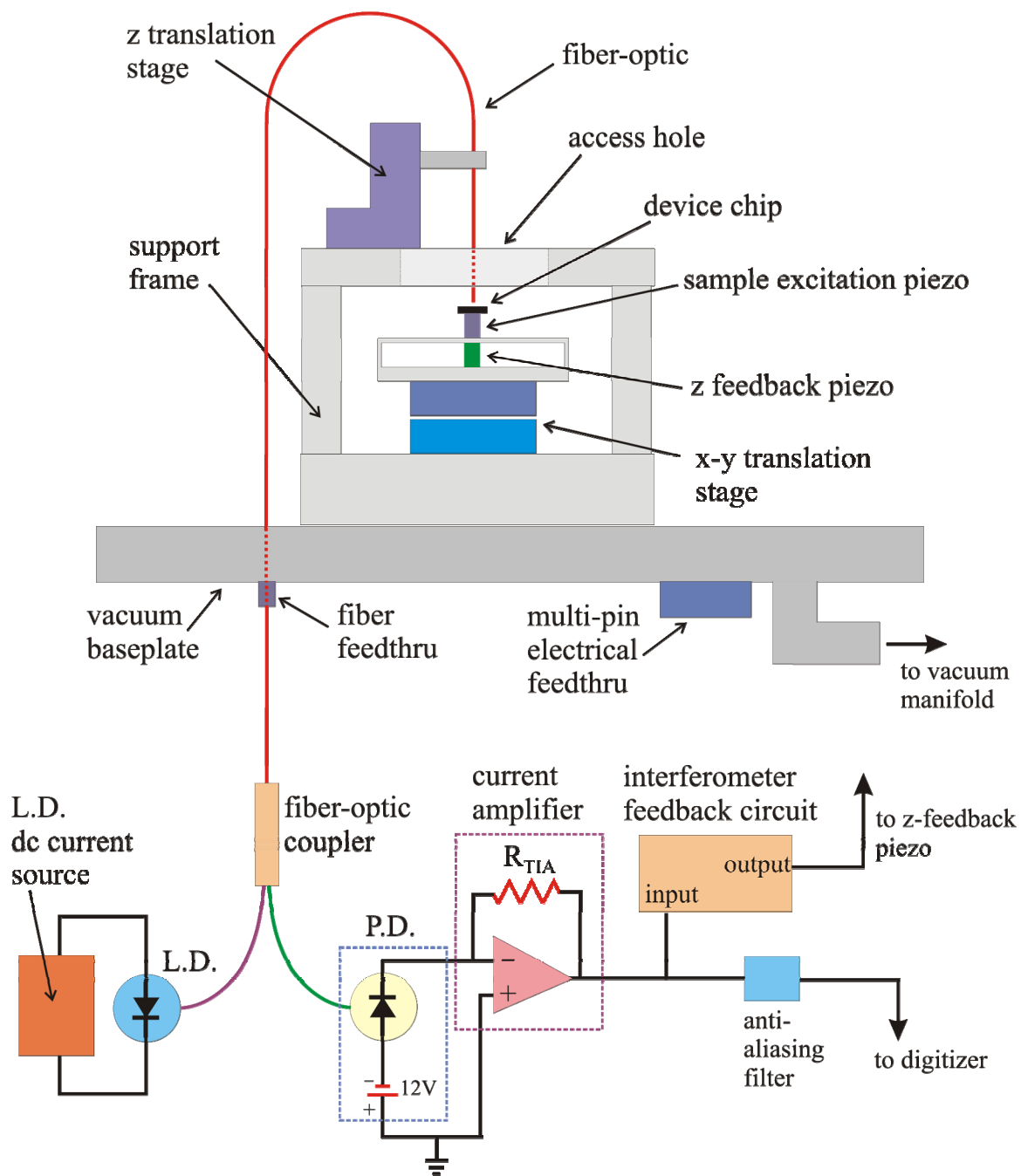


Figure 5.1: A block diagram of the home-built fiber-optic interferometer apparatus.

All vacuum O-rings are lightly coated with a thin layer of Apiezon high vacuum grease. In an effort to isolate the interferometer from mechanical vibrations in the laboratory, the entire vacuum baseplate is centered on a 2 foot x 1.5 foot x 1.5 inch thick aluminum plate that is suspended from a wooden frame by several bungee cords. The wood frame sits on top of a massive laser table with foam rubber spacers inserted between the feet of the frame and the surface of the table.

The optical radiation for the fiber-optic interferometer is supplied by a 1.4 mW laser diode (Thorlabs P/N LPS-SMF28-1310-FC) with an output wavelength of 1308 nm. Under normal operation, 16 mA of current is run through the laser diode by a home-built, battery powered current source. The laser light is launched into one arm of a 2 x 2 fiber-optic coupler (Thorlabs P/N 10202A-50-FC) where 50% of the incident power is coupled to the detection arm leading to the device chip. The other half of the power is sent to a beam dump (not shown in Figure 5.1) where it is absorbed. The light reflected by the sample is collected by the same fiber and travels to the photodetector where it interferes with the reference beam generated by the reflection from the glass/air interface at the end of the detection fiber.

The photodetector used is the Thorlabs D400FC and consists of an FC coupled InGaAs PIN photodiode with a responsivity \mathcal{R} of approximately 0.8 A/W at 1308 nm. The diode is reverse biased by a miniature 12 V battery and the entire detector is enclosed in an aluminum housing to shield it from stray electrical signals. The photocurrent output of the detector is an SMA electrical connector, which is connected directly to the BNC input of the current amplifier via an SMA to BNC adapter. The reason for connecting the photodetector directly to the input of the amplifier is that stray electrical pickup was

observed even when a short section of shielded cable was used. Direct connection to the amplifier solved this problem. The transimpedance (current) amplifier is the Melles-Griot model 13AMP005 whose characteristics are shown in Table 5.1. This amplifier has five user selectable gain settings where the gain is determined by the value of the feedback resistor R_{TIA} .

R_{TIA} (V/A)	3 db bandwidth	rms input noise current	noise spectral density ($\text{pA}/\sqrt{\text{Hz}}$)
10^3	5 MHz	100 nA	45
10^4	1.25 MHz	12 nA	11
10^5	300 kHz	1.5 nA	2.7
10^6	75 kHz	180 pA	0.66
10^7	15 kHz	32 pA	0.26

Table 5.1: Characteristics of the Melles-Griot 13AMP005 transimpedance amplifier used to amplify the photocurrent signal of the fiber-optic interferometer.

The output of the current amplifier is the voltage V_{amp} , which is proportional to the photodiode current I_{pd} by Ohm's law, $V_{\text{amp}} = R_{TIA}I_{\text{pd}}$. The voltage signal from the amplifier is "Tee-d" where one leg is fed to the input of the interferometer feedback circuit and the other leg is sent to the 50 ohm input of an anti-aliasing, low pass filter. The output waveform of the filter is then digitized by a computer.

Figure 5.2 shows a circuit diagram of the home-built, constant current source for the laser diode. Four, 12V car batteries are connected in series and provide voltage levels of 0V, $\pm 12\text{V}$, and $\pm 24\text{V}$. This circuit is powered by the $\pm 24\text{V}$ supplies where each supply voltage is connected to ground via a 100 μF electrolytic capacitor so as to filter out electrical noise pickup from the batteries and cables leading to the circuit.

We now detail the theory of operation of this current source. The resistors R_1 and R_2 form a voltage divider that determines the voltage V_A at the positive input of the op-amp

$$V_A = \left(\frac{R_2}{R_1 + R_2} \right) V_{cc}. \quad 5.1$$

Through negative feedback, the op-amp equalizes the voltages at the positive and negative inputs which sets the voltage to be V_A at the emitter of the pnp transistor. The current I_E that flows through the transistor is determined by the voltage drop across R_E :

$$I_E = \frac{V_{cc} - V_A}{R_E}. \quad 5.2$$

The transistor current flows through the laser diode and makes its way to ground through the 0–25 mA current meter. The current through the laser is adjusted by the variable resistor, R_1 , to the desired setting on the current meter (typically ~ 16 mA).

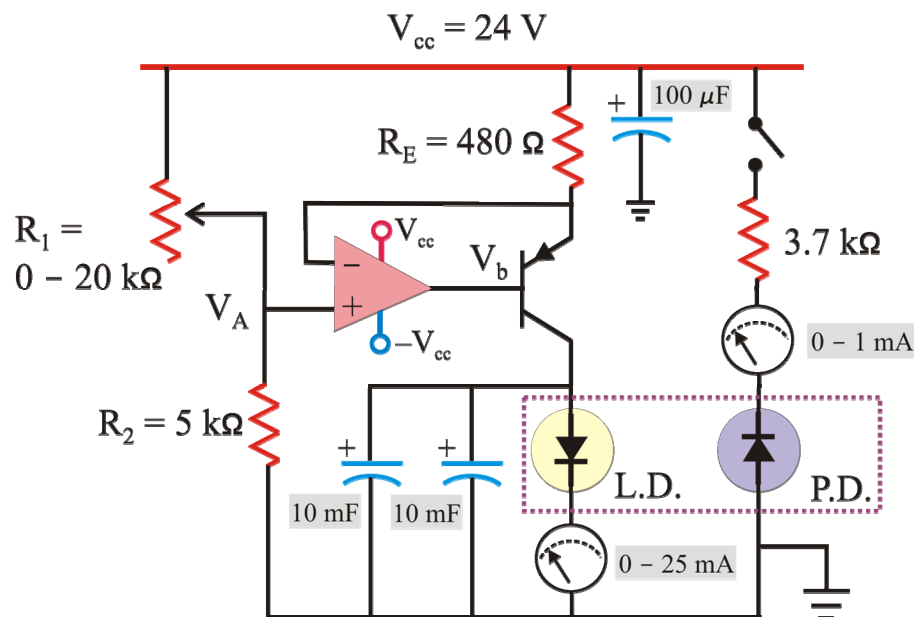


Figure 5.2: Circuit diagram of the constant current source for the laser diode.

In the laser housing is a photodiode that “sees” a small fraction of the output laser light. This photodiode monitors the optical power output of the laser and can be used in a feedback loop to reduce amplitude noise of the laser. In our experimental setup, we simply use it to monitor the optical power, where the photocurrent is read out on the 0–1

mA current meter placed in series with the photodiode. As a protective measure, two 10 mF electrolytic capacitors are connected in parallel with the laser diode to provide a low impedance path for fast current transients, which could otherwise destroy the laser diode.

For interferometric detection of the motion of micron and submicron mechanical resonators, the cleaved end of the detection fiber is positioned in the vertical direction to within 50 microns of the device chip. Due to the interference between the reference wave and the wave reflected by the device chip, the voltage signal at the output of the transimpedance amplifier has the form

$$V(d) = \frac{V_- + V_+}{2} + \frac{V_- - V_+}{2} \cos\left(\frac{4\pi d}{\lambda}\right) \quad 5.3$$

where d is the width of the gap between the end of the fiber and the surface of the device chip and λ is the wavelength of the laser light. This function is plotted in Figure 5.3 versus the dimensionless variable d/λ .

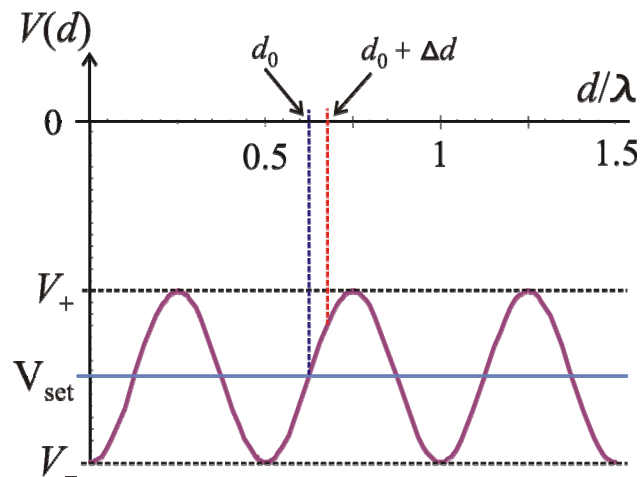


Figure 5.3: Interference waveform of the voltage output of the transimpedance amplifier as a function of d/λ .

For sensitive interferometry, it is essential to operate the interferometer at nominal gap widths where the slope of the voltage waveform plotted above is maximized. These

points occur for widths $d = m\lambda/8$, ($m = 1, 3, 5, 7, \dots$). Even if one were to carefully position the fiber with the vertical translation stage to one of these values, over time the width d would vary due to thermal expansions and/or contractions of the steel support frame and other structures. Active feedback is therefore needed to keep the width of the gap locked. The circuit of Figure 5.4 performs this task. All op-amps in this circuit are powered by $\pm 18\text{V}$ generated by six 6V lantern batteries connected in series. The ground of the lantern battery array is connected to the ground of the car battery array.

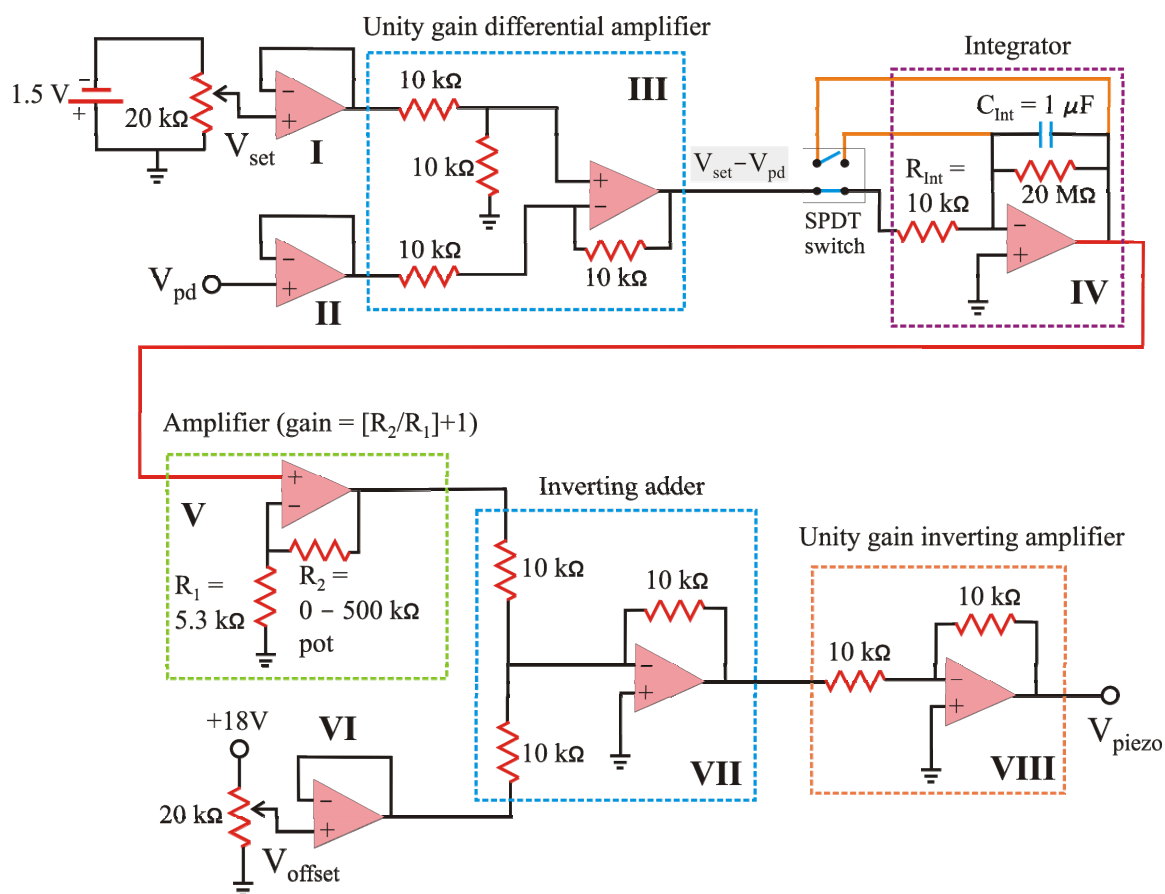


Figure 5.4: Feedback circuit for locking the interferometer to the sensitive portion of the interference waveform.

Referring to Figure 5.4, the set point voltage V_{set} is adjusted between 0 and -1.5V using the 20 kΩ potentiometer. For the best displacement sensitivity, V_{set} is adjusted to lie

halfway between V_+ and V_- as shown in Figure 5.3 and is sent to the input of voltage follower **I**. The photodiode voltage V_{pd} from the output of the transimpedance amplifier is sent to the input of voltage follower **II**. The outputs of **I** and **II** are then sent to the inputs of differential amplifier **III**, the output of which is the error signal ($V_{set} - V_{pd}$). The time integral of the error signal, scaled by the factor $-(R_{int}C_{int})^{-1}$, is generated by the integrator **IV** and gets amplified by **V** with a gain of $1 + R_2/R_1$. An offset voltage V_{offset} lying between 0 and 18V is input into voltage follower **VI** and is added to the amplified, integrated signal by **VII**. The sign change, introduced by the adder, is undone by inverting amplifier **VIII** whose output is the voltage sent to the z-feedback piezoelectric.

To understand how this interferometer feedback circuit stabilizes the width of the gap, consider Figure 5.3 where the desired gap is d_0 . At a later time the gap changes to $d_0 + \Delta d$, which generates an error signal with a negative polarity. The integrator introduces another negative sign creating a positive voltage that becomes amplified. The result is that V_{piezo} is positive thereby expanding the feedback piezoelectric, which decreases the gap back toward d_0 . Similarly, for a displacement of $-\Delta d$, the error signal would be positive, which becomes negative after the integrator. The voltage sent to the piezo in this case is negative, causing the piezo to contract, thereby increasing the gap back toward d_0 .

The single-pull double-throw (SPDT) switch is a safety feature that allows one to disable the output of the feedback circuit by simultaneously disconnecting the integrator input from the differential amplifier and shorting the capacitor C_{int} so that the output of the integrator is sent to 0V. Disabling the feedback circuit is safe electrical practice when the experimenter has to make manual adjustments of the gap or some other part of the apparatus. Also if the interferometer becomes “unlocked” due to a jarring of the

apparatus, the feedback circuit is disabled and the system is allowed to come to rest before the feedback is restored. Mode hopping of the laser diode creates intensity fluctuations that can also unlock the interferometer. For this case, the feedback is disabled and the FC coupler from the laser is serviced until mode hopping is eliminated.

The performance of the fiber-optic interferometer is evaluated in Figure 5.5, which plots the interferometer noise spectrum ($\text{pm}/\sqrt{\text{Hz}}$) versus frequency.

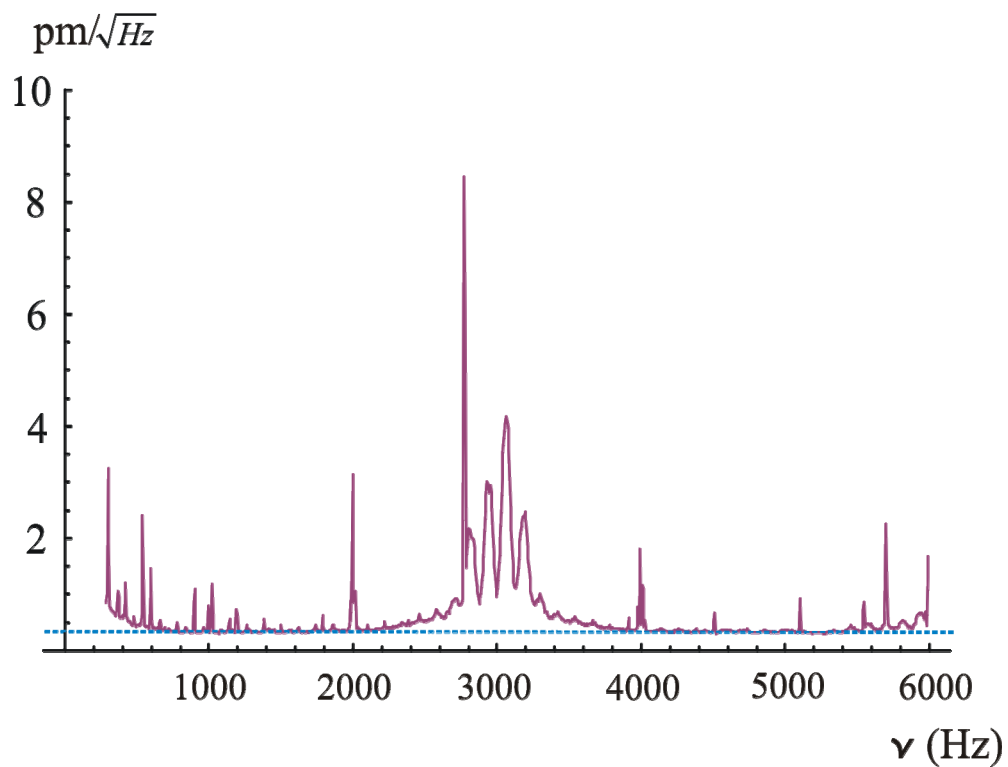


Figure 5.5: Experimentally measured noise spectrum for the feedback stabilized fiber-optic interferometer.

This noise spectrum was generated in the following way: The detection fiber was aimed at a silicon substrate with $V_+ = -0.155 \text{ V}$ and $V_- = -0.505 \text{ V}$. The set point voltage was adjusted to the midpoint of -0.330 V . The digitization rate was 12 kHz setting a Nyquist frequency of 6 kHz. The low pass filter before the digitizer was set to 6 kHz to suppress artifacts due to aliasing. A single time-domain scan of the feedback-locked voltage output

of the transimpedance amplifier consisted of 2048 points where 646 total scans were acquired. Each time-domain scan was Fourier transformed and the power spectrum computed. The 646 resulting power spectra were averaged to yield the noise spectrum in Figure 5.5. The spacing between adjacent frequency points in Figure 5.5 is $12\text{kHz}/2048 = 5.86\text{ Hz}$.

In Figure 5.5 it can be seen that many spikes exist in the noise spectrum. These are of unknown origin, however could be due to electrical pickup and laser intensity noise. At the time when this spectrum was acquired, neither the laser diode current circuit nor the interferometer feedback circuit had power supply filter capacitors so that electrical pickup is a very likely explanation for the appearance of these spikes. Additionally, these measurements were taken at atmospheric pressure where sound waves in this frequency range could be contributing to the noise. Operation of the interferometer in vacuo should decrease the intensity of some of these spikes. The sensitivity of the interferometer appears to have a baseline of $0.4\text{ pm}/\sqrt{\text{Hz}}$, shown as the dashed blue line in Figure 5.5. The interferometer is at its quietest in the frequency range from 4 kHz to 5.5 kHz.

Figure 5.6 shows the mechanical frequency spectrum of a triple-paddle resonator, fabricated at the Micro Devices Laboratory at the Jet Propulsion Laboratory (JPL) in Pasadena, CA. The inset is a drawing of the resonator (blue), which measures approximately 150 microns in length and consists of two large “wing” paddles and a “head” paddle at the end. The resonator structure is attached to the stationary base (gray) by a thin “neck” and freely hangs a few microns above the parent silicon substrate (yellow). The 7th mechanical mode of this structure has a frequency of approximately 1

MHz and a Q of $\sim 90,000$. For this mode, the wings oscillate 180° out of phase with each other about the axis perpendicular to the neck. Meanwhile, the head executes torsional oscillations about the axis of the neck. This mode is of interest because of its high value of Q .

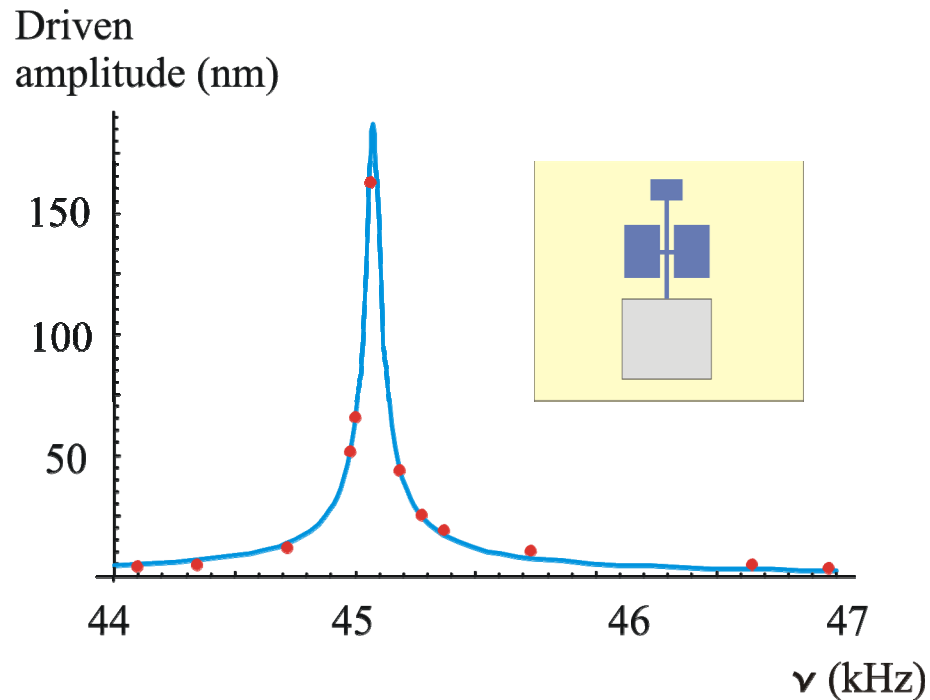


Figure 5.6: The frequency spectrum, measured by fiber-optic interferometry, of the lowest mechanical mode of a triple-paddle resonator fabricated at the Micro Devices Laboratory at JPL.

The fiber-optic interferometer apparatus described in this chapter was used to optically detect the lowest mode of this structure, namely, out-of-plane flapping. The device chip was glued to the excitation piezo and the measurements were taken with the entire interferometer apparatus in a vacuum of 150 mtorr. The excitation frequency was scanned and the output of the transimpedance amplifier was sent to a lock-in amplifier. The voltage amplitude data, taken from the lock-in, was appropriately transformed to the driven amplitude in nanometers. The experimental data are shown as the red points in Figure 5.6. This data set was fit to a harmonic oscillator resonance profile, shown as the

blue curve. From this fit, the resonance frequency is found to be 45.075 kHz and the mechanical Q is 844.

In this final chapter, we have described a scanning fiber-optic interferometer apparatus for optical detection of the motion of micron scale and nanoscale mechanical resonators. For controlled, low-noise operation of the interferometer, two battery powered op-amp circuits were constructed, a constant current source for the diode laser and an interferometer feedback circuit. The noise spectrum of the feedback stabilized interferometer was experimentally measured for frequencies from dc to 6 kHz and was found to contain a large number of spurious narrowband spikes. These noise signals are attributed to electrical pickup in the power cables leading to the control circuitry, acoustic room noise, and amplitude fluctuations in the output of the laser diode. To lessen these noise sources, power supply filter capacitors were included in the two circuits and interferometry experiments were done in vacuum, unfortunately the noise spectrum was not measured after these changes were implemented. Preliminary observations were made, with the fiber-optic interferometer, on the lowest mechanical mode of a 150 micron long, triple-paddle resonator in a vacuum of 150 mtorr. We were able to map out the resonance curve for this mode and found it to have a resonance frequency of 45.075 kHz and a Q of 844. These preliminary results hold promise for interferometric detection of submicron-scale mechanical resonators. Finally, the author wishes to thank Dr. Kyung-Ah Son and Dr. Thomas George at JPL for graciously providing the triple-paddle resonator samples.

Conclusions

In conclusion, we have presented three novel experiments to image and spectroscopically probe single molecules using micron- and submicron-scale mechanical resonators. Force Detected Optical Spectroscopy (FDOS) and Electric Dipole Difference Imaging (EDDI) experiments rely on detecting the motion of the mechanical resonator, driven by the time-dependent forces between the optically induced molecular dipole and probe dipole. Geometric optimizations of the mechanical resonator and metallic probe were examined in detail for FDOS. For an optimized probe geometry at a particular optical wavelength, the magnitude of the coherent dipole force is ultimately limited by laser absorption and heating of the probe. The dipole force is compared to the Brownian noise force on the resonator to arrive at the fundamentally best signal-to-noise ratio for these experiments. An example of FDOS detection of a single quantum dot yielded a peak SNR of 0.2 in a 1 Hz measurement bandwidth. The situation improves for EDDI, where the probe is an electret nanoparticle and the resonant mechanical motion is driven by the force between the electret probe and the modulated difference dipole of the single molecule. Much higher SNRs are realizable for EDDI, since the permanent dipole of the electret is several orders of magnitude larger than the optically induced probe dipoles in FDOS. As an example, EDDI detection of the 5.6 Debye difference dipole of a particular coumarin molecule gives a predicted SNR of 3,500 in a 1 Hz measurement bandwidth. Single-molecule vibrational spectroscopy using EDDI is also promising, since typical difference dipoles between molecular vibrational levels are of the order 0.01 D, giving SNRs of order 10 in a 1 Hz bandwidth.

Three novel optical scattering mechanisms were proposed to enhance fiber-optic interferometric detection of submicron resonators. The motion of the resonator modulates the phase, amplitude, or polarization of the optical scattering from plasmon nanoparticles bound to the resonator. For each mechanism, Brownian motion of the resonator becomes encoded as an optical noise source, which is compared to the shot noise of the reference field and amplifier noise. Calculations suggest that optical detection of linear modes of oscillation is nearly Brownian-motion limited for mechanical frequencies up to about 40 MHz. Mechanical frequencies up to 600 MHz may be detected near the Brownian limit for torsional modes of oscillation.

A novel, nanoscale device for detecting single biological molecules in solution was proposed, where electrostatic interactions between the electret probe and polarizable molecule create a shift of the mechanical frequency of the resonator. This shift is monitored over the course of the experiment to give information on the position and orientation of the molecule with microsecond time resolution. As an interesting application, the kinetics of binding and unbinding of a protein molecule to its corresponding receptor molecule may be studied with this device. Due to the coupling of the electrical and mechanical degrees of freedom, this device also has applications as a resonant element for low-mass radio frequency transceivers.

Finally, a scanning, fiber-optic interferometer apparatus was built for detecting the motion of micron- and submicron-sized mechanical resonators. Measurements were made of the noise of this instrument from dc to 6 kHz. Toward the goal of detecting nanoscale resonators, measurements were made with this instrument, on the lowest frequency mode of a 150 micron long, triple-paddle resonator.

Appendix A. Derivation of Harmonic Oscillator Noise Spectral Densities from the Correlation Function

Consider a one-dimensional harmonic oscillator described by the generalized coordinate ξ , which is measured relative to the equilibrium configuration. The coordinate ξ could be, for example, the familiar linear displacement of a mass on a spring or the angle of torsion about the axis of an elastic beam. As a concrete example we consider a linear harmonic oscillator comprised of a spring of force constant k (N/m) to which is attached a mass M (kg) with a linear position coordinate y (m) measured relative to the equilibrium position. The results of this appendix, however, will be equally valid for a generalized coordinate ξ describing the state of the oscillator with a generalized inertia M_ξ and generalized spring constant k_ξ . The equation of motion for the linear harmonic oscillator is [1]

$$\ddot{y}(t) + \gamma \dot{y}(t) + \omega_h^2 y(t) = \frac{F(t)}{M}, \quad \text{A.1}$$

where $\omega_h = \sqrt{k/M}$ (radians/s) is related to the natural frequency ν_h (Hz) of the harmonic oscillator by $\omega_h = 2\pi\nu_h$ and γ (s^{-1}) is the damping constant, which is related to the frequency and quality factor of the oscillator by $\gamma = \omega_h/Q$. On the right hand side of equation A.1, $F(t)$ is the net external force on the oscillator, which for our purposes is the sum of an imposed driving force and a random force due to microscopic thermal processes that bring the oscillator to thermal equilibrium at temperature T (K).

For the case where the driving force is zero the coordinate $y(t)$ will be a random variable due to the presence of the fluctuating thermal forces. To derive the statistics of y we consider the correlation function $G_y(\tau)$ [2]

$$G_y(\tau) = \lim_{t \rightarrow \infty} \frac{1}{2t} \int_{-t}^t y(t') y(t' + \tau) dt', \quad \text{A.2}$$

which gives a measure of how strongly future values of y depend on the present value.

We now proceed to find the spectral density $\tilde{G}_y(\nu)$ of the fluctuations of $y(t)$, which is the Fourier transform of the correlation function.[2] For stationary, ergodic processes $G_y(\tau)$ is a symmetric function of τ [2] so that the spectral density may be written [3]

$$\tilde{G}_y(\nu) = 4 \int_0^{\infty} G_y(\tau) \cos(2\pi\nu\tau) d\tau. \quad \text{A.3}$$

For a harmonic oscillator at absolute temperature T the correlation function is [3]

$$G_y(\tau) = \langle y^2 \rangle e^{-\frac{\gamma}{2}\tau} \left(\cos(\omega'\tau) + \frac{\gamma}{2\omega'} \sin(\omega'|\tau|) \right), \quad \text{A.4}$$

where $\langle y^2 \rangle$ is the mean-squared oscillator amplitude and $\omega' = \sqrt{\omega_h^2 - \gamma^2/4}$. Inserting

A.4 into A.3, we find

$$\tilde{G}_y(\nu) = \left(\frac{4\gamma \langle y^2 \rangle \omega_h^2}{(\omega^2 - \omega_h^2)^2 + \gamma^2 \omega^2} \right), \quad \text{A.5}$$

where $\omega = 2\pi\nu$.

From the Weiner-Khintchine theorem, the contribution $y^2(\nu_1, \Delta\nu)$ to the mean squared displacement $\langle y^2 \rangle$ in the frequency interval $[(\nu_1 - \Delta\nu/2), (\nu_1 + \Delta\nu/2)]$ is [2]

$$y^2(\nu_1, \Delta\nu) = \int_{\nu_1 - \frac{\Delta\nu}{2}}^{\nu_1 + \frac{\Delta\nu}{2}} \tilde{G}_y(\nu) d\nu, \quad \text{A.6}$$

where

$$\langle y^2 \rangle = \int_0^\infty \tilde{G}_y(\nu) d\nu. \quad \text{A.7}$$

Also, the equipartition theorem states that

$$\frac{1}{2} M \omega_h^2 \langle y^2 \rangle = \frac{1}{2} k_B T, \quad \text{A.8}$$

where k_B is Boltzman's constant. Using A.8 in A.5, the spectral density $\tilde{G}_y(\nu)$ may be written

$$\tilde{G}_y(\nu) = \frac{4\omega_h k_B T}{MQ} \left(\frac{1}{(\omega^2 - \omega_h^2)^2 + \omega_h^2 \omega^2 / Q^2} \right), \quad \text{A.9}$$

and at the mechanical resonance frequency this reduces to

$$\tilde{G}_y(\nu_h) = \frac{4k_B T Q}{M \omega_h^3}. \quad \text{A.10}$$

We may now find the spectral density of force fluctuations on the oscillator. Taking a Fourier transform of equation A.1, we find the transfer function $f(\omega)$ between the Fourier component of the force $\tilde{F}(\nu)$ and the Fourier component of the displacement $\tilde{y}(\nu)$ at frequency ν :

$$\tilde{F}(\nu) = M(\omega_h^2 - \omega^2 + i\gamma\omega)\tilde{y}(\nu) = f(\omega)\tilde{y}(\nu). \quad \text{A.11}$$

The spectral density of force fluctuations $\tilde{G}_F(\nu)$ is then related to $\tilde{G}_y(\nu)$ by [3]

$$\tilde{G}_F(\nu) = |f(\omega)|^2 \tilde{G}_y(\nu) = M^2 \left[(\omega_h^2 - \omega^2)^2 + \gamma^2 \omega^2 \right] \tilde{G}_y(\nu), \quad \text{A.12}$$

and at the mechanical resonance frequency we have

$$\tilde{G}_F(\nu_h) = \frac{4M\omega_h k_B T}{Q}. \quad \text{A.13}$$

We will also need the spectral densities for a torsional mechanical resonator with angular coordinate θ (radians), moment of inertia I ($\text{kg}\cdot\text{m}^2$), and torsional spring constant k_t ($\text{N}\cdot\text{m}$). In analogy with A.10 and A.13, at the mechanical resonance frequency we find:

$$\tilde{G}_\theta(\nu_h) = \frac{4k_B T Q}{I\omega_h^3} \quad \text{A.14}$$

and

$$\tilde{G}_T(\nu_h) = \frac{4I\omega_h k_B T}{Q}, \quad \text{A.15}$$

where the subscript T denotes torque.

References

1. Kleppner, D. and R.J. Kolenkow, *An Introduction to Mechanics*. 1973, San Francisco: McGraw-Hill, Inc.
2. Weissbluth, M., *Photon-Atom Interactions*. 1989, San Diego: Harcourt Brace Jovanovich.
3. McCombie, C.W., *Fluctuation Theory in Physical Measurements*. Rep. Prog. Phys., 1953. **16**: p. 266–320.

Appendix B. The Energy of a Polarizable Object in an External Electric Field

The force on a dipole $\vec{p}(\vec{r})$ located at position \vec{r} due to the electric field $\vec{E}(\vec{r};\theta)$ of the electret probe is

$$\vec{F}(\vec{r};\theta) = \vec{p}(\vec{r}) \cdot [\vec{\nabla} \vec{E}(\vec{r};\theta)]. \quad \text{B.1}$$

This is true regardless of the nature of the dipole (i.e., fixed or induced). In the following, we will show that this force is conservative for the case where the orientation of the polarizable particle and θ are held fixed with respect to the laboratory frame. For a conservative force, it is sufficient to show that it may be written as the gradient of a scalar function of position; this function is then identified as the negative of the potential energy of the particle.

Evaluating $\vec{\nabla} \vec{E}(\vec{r};\theta)$ in Cartesian coordinates yields the tensor expression

$$\vec{\nabla} \vec{E}(\vec{r};\theta) = \hat{e}_i \frac{\partial}{\partial x_i} [E_j(\vec{r};\theta) \hat{e}_j] = \hat{e}_i \hat{e}_j \frac{\partial E_j(\vec{r};\theta)}{\partial x_i}, \quad \text{B.2}$$

where summation over the repeated indices i and j is assumed. Evaluating equation B.1 gives

$$\begin{aligned} \vec{F}(\vec{r};\theta) &= [p_k(\vec{r}) \hat{e}_k] \cdot \hat{e}_i \hat{e}_j \frac{\partial E_j(\vec{r};\theta)}{\partial x_i} \\ &= p_k(\vec{r}) \delta_{ki} \hat{e}_j \frac{\partial E_j(\vec{r};\theta)}{\partial x_i} \\ &= \left(p_i(\vec{r}) \frac{\partial E_j(\vec{r};\theta)}{\partial x_i} \right) \hat{e}_j. \end{aligned} \quad \text{B.3}$$

Since $\vec{E}(\vec{r};\theta)$ is an electrostatic field, it may be written as the gradient of a potential function $\Phi(\vec{r};\theta)$:

$$\vec{E}(\vec{r};\theta) = -\hat{e}_m \frac{\partial \Phi(\vec{r};\theta)}{\partial x_m}. \quad \text{B.4}$$

From this it follows that $\frac{\partial E_j(\vec{r};\theta)}{\partial x_i} = -\frac{\partial^2 \Phi(\vec{r};\theta)}{\partial x_i \partial x_j}$ and since $\Phi(\vec{r};\theta)$ is a “regular”

function we have the property

$$\frac{\partial^2 \Phi(\vec{r};\theta)}{\partial x_i \partial x_j} = \frac{\partial^2 \Phi(\vec{r};\theta)}{\partial x_j \partial x_i}, \quad \text{B.5}$$

which implies

$$\frac{\partial E_j(\vec{r};\theta)}{\partial x_i} = \frac{\partial E_i(\vec{r};\theta)}{\partial x_j}. \quad \text{B.6}$$

Using these facts, equation B.3 may now be written as

$$\vec{F}(\vec{r};\theta) = \left(p_i(\vec{r}) \frac{\partial E_i(\vec{r};\theta)}{\partial x_j} \right) \hat{e}_j. \quad \text{B.7}$$

In the following, for notational simplicity functions of \vec{r} and θ are implied and the arguments are suppressed. Note that the polarizability tensor does **NOT** depend on position. For a particle described by a linear, anisotropic polarizability tensor with Cartesian components α_{ik} , the components of the induced dipole are related to the electric field of the probe through

$$p_i = \alpha_{ik} E_k, \quad \text{B.8}$$

so that equation B.7 becomes

$$\vec{F} = \left(\alpha_{ik} E_k \frac{\partial E_i}{\partial x_j} \right) \hat{e}_j. \quad \text{B.9}$$

Now, using the fact that

$$\frac{\partial (E_k E_i)}{\partial x_j} = E_k \frac{\partial E_i}{\partial x_j} + E_i \frac{\partial E_k}{\partial x_j}, \quad \text{B.10}$$

we may rewrite equation B.9 as

$$\vec{F} = \alpha_{ik} \frac{\partial (E_k E_i)}{\partial x_j} \hat{e}_j - \alpha_{ik} E_i \frac{\partial E_k}{\partial x_j} \hat{e}_j. \quad \text{B.11}$$

Since the indices are summed over without restrictions, we may interchange their roles in

the second term of equation B.11 transforming it into $\alpha_{ki} E_k \frac{\partial E_i}{\partial x_j} \hat{e}_j$. Since the

polarizability is a symmetric tensor (i.e., $\alpha_{ki} = \alpha_{ik}$), this term becomes $\alpha_{ik} E_k \frac{\partial E_i}{\partial x_j} \hat{e}_j$ and,

upon adding equations B.9 and B.11, we find

$$2\vec{F} = \alpha_{ik} \frac{\partial (E_k E_i)}{\partial x_j} \hat{e}_j. \quad \text{B.12}$$

Also, the components of the polarizability tensor are independent of position and therefore may be factored inside the derivative giving

$$\begin{aligned} \vec{F}(\vec{r}; \theta) &= \hat{e}_j \frac{\partial}{\partial x_j} \left(\frac{1}{2} \alpha_{ik} E_i E_k \right) \\ &= -\vec{\nabla} \left(-\frac{1}{2} \alpha_{ik} E_i E_k \right). \end{aligned} \quad \text{B.13}$$

Equation B.13 expresses the fact that the force on a particle with a linear, anisotropic polarizability tensor is equal to minus the gradient of a scalar function of position (i.e.,

$\vec{F}(\vec{r};\theta) = -\vec{\nabla}U(\vec{r};\theta)$ and is therefore conservative. The function $U(\vec{r};\theta)$ is the potential energy of the particle, which from B.13 is

$$U(\vec{r};\theta) = -\frac{1}{2} \alpha_{ik} E_i(\vec{r};\theta) E_k(\vec{r};\theta). \quad \text{B.14}$$

Appendix C. Ohmic Dissipation of the Induced Polarization Currents in the Electrodes of the Single-Molecule Binding Sensor Device

In this appendix we estimate the Ohmic losses in the electrodes of the single molecule sensor of Figure 1.4, which arise from the finite penetration of the rf field of the electret probe. The damping due to this mechanism will then be compared to the familiar frictional damping of the mechanical resonator.

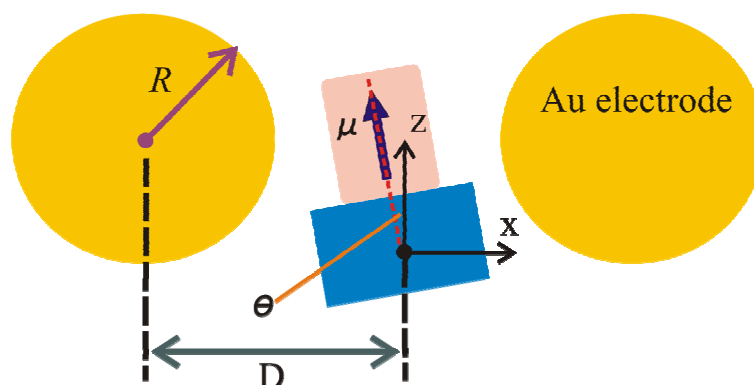


Figure C.1: A simplified model of the device in Figure 1.4 used in the estimation of Ohmic losses in the nanoscale electrodes. The electrodes are approximated to be gold spheres of radius R since the polarization for this shape is simply related to the internal electric field. Torsion of the mechanical resonator by angle θ gives rise to a component of the ferroelectric dipole and a corresponding rf electric field along the x direction, which drives electric currents in the metal electrodes and gives rise to Ohmic dissipation.

A simplified picture of the device of Figure 1.4 is shown in Figure C.1, where the drive/detection electrodes are taken to be gold spheres of radius R . Motion of the torsional resonator at the mechanical resonance frequency generates a component of the dipole moment along the x direction whose electric field drives currents in the nearby conductors generating Ohmic dissipation.

We first calculate the dissipated power due to viscous damping of the resonator. For the mechanical resonator characterized by the angular coordinate θ , the damping torque is

$$T_{mech} = I\gamma\dot{\theta}, \quad \text{C.1}$$

where I is the moment of inertia of the resonator, $\gamma = \omega_h / Q$ is the damping rate of the mechanical energy due to friction, and ω_h (radians/s) is the resonance frequency with Q the quality factor of the torsional mode. The mechanically dissipated power is then given as

$$P_{mech} = T_{mech}\dot{\theta} = I\gamma\dot{\theta}^2. \quad \text{C.2}$$

For harmonic time dependence of the angular coordinate

$$\theta(t) = \theta(\omega) \left(\frac{e^{i\omega t} + e^{-i\omega t}}{2} \right), \quad \text{C.3}$$

where the amplitude $\theta(\omega)$ is taken to be real, we evaluate the time derivative of $\theta(t)$:

$$\dot{\theta}(t) = i\omega\theta(\omega) \left(\frac{e^{i\omega t} - e^{-i\omega t}}{2} \right). \quad \text{C.4}$$

Inserting this into equation C.2 we obtain the mechanically dissipated power

$$P_{mech}(t) = \frac{I\gamma\omega^2 [\theta(\omega)]^2}{2} [1 - \cos(2\omega t)], \quad \text{C.5}$$

of which, only the dc part is of interest since this is equal to the time-averaged dissipated power denoted here by brackets $\langle \rangle$:

$$\langle P_{mech} \rangle = \frac{I\gamma\omega^2 [\theta(\omega)]^2}{2}. \quad \text{C.6}$$

We now calculate the electrical dissipation in the nearby conductors, where we make the approximation that the field of the electret is uniform over the volume of the electrodes and has the value equal to that of the field evaluated at the center of each electrode. This is an enormous simplification of the problem, but should give us an order-of-magnitude estimate of the electrical damping. With these approximations, the free current density \mathbf{J} , the polarization \mathbf{P} , and the total electric field \mathbf{E} inside the electrodes are uniform, which results from the assumed spherical shape of the electrodes. The continuity equation for electric charge is expressed as

$$\vec{J} \cdot \hat{n} = \frac{\partial}{\partial t} (\vec{P} \cdot \hat{n}), \quad \text{C.7}$$

where \hat{n} is the outward pointing unit vector at an arbitrary point on the surface of one of the electrodes and the surface charge density is $\vec{P} \cdot \hat{n}$. Since equation C.7 must hold at every point on the surface, we deduce the relationship between the free current density and the polarization within the volume of the electrode:

$$\vec{J} = \frac{\partial \vec{P}}{\partial t}. \quad \text{C.8}$$

The total electric field inside each electrode is given by

$$\vec{E} = \vec{E}_a(\theta) + \vec{E}_p, \quad \text{C.9}$$

where $\vec{E}_a(\theta)$ is the applied field of the electret and \vec{E}_p the electric field of the induced polarization, which for a spherical shape is

$$\vec{E}_p = -\frac{\vec{P}}{3\epsilon_0}. \quad \text{C.10}$$

Given the time dependence for $\theta(t)$ in equation C.3, the most general form for the polarization is

$$\vec{P}(t) = \frac{1}{2} \left(\vec{P}(\omega) e^{i\omega t} + \vec{P}(\omega)^* e^{-i\omega t} \right) + \vec{P}_0, \quad \text{C.11}$$

where $\vec{P}(\omega)$ is the complex amplitude and \vec{P}_0 the real dc polarization. Expanding the applied field out to first order in θ and making use of equation C.10 we find

$$\vec{E} \approx \vec{E}_a(0) + \frac{\partial \vec{E}_a}{\partial \theta_0} \theta - \frac{\vec{P}}{3\epsilon_0}, \quad \text{C.12}$$

and inserting equation C.11 into C.12 gives

$$\vec{E} \approx \left(\vec{E}_a(0) - \frac{\vec{P}_0}{3\epsilon_0} \right) - \frac{\vec{P}(\omega) e^{i\omega t} + c.c.}{6\epsilon_0} + \frac{\partial \vec{E}_a}{\partial \theta_0} \theta. \quad \text{C.13}$$

The term in parentheses in equation C.13 is the total dc electric field inside the conductor, which must be zero. Therefore we arrive at the relation between \vec{P}_0 and $\vec{E}_a(0)$

$$\vec{P}_0 = 3\epsilon_0 \vec{E}_a(0). \quad \text{C.14}$$

The constitutive relation between the free current density and total electric field is

$$\vec{J}(t) = \sigma \vec{E}(t), \quad \text{C.15}$$

where σ is taken to be the dc conductivity of the metal in $(\Omega \cdot \text{m})^{-1}$. Using equations C.8 and C.11 we have

$$\vec{J}(t) = \frac{i\omega}{2} \left(\vec{P}(\omega) e^{i\omega t} - \vec{P}(\omega)^* e^{-i\omega t} \right). \quad \text{C.16}$$

Using C.13 and C.16 in equation C.15 along with the time harmonic form (equation C.3) for the angular coordinate allows us to solve for $\vec{P}(\omega)$ in terms of $\theta(\omega)$:

$$\vec{P}(\omega) = \left(\frac{3\epsilon_0 \sigma}{\sigma + i(3\epsilon_0 \omega)} \right) \vec{E}_a' \theta(\omega), \quad \text{C.17}$$

where $\vec{E}_a' \equiv \frac{\partial \vec{E}_a}{\partial \theta_0}$.

The electrically dissipated power is

$$\begin{aligned} P_e &= 2 \int_V dV (\vec{J} \cdot \vec{E}) = \frac{2}{\sigma} \int_V dV (\vec{J} \cdot \vec{J}) \\ &= \frac{2V}{\sigma} \vec{J} \cdot \vec{J}, \end{aligned} \quad \text{C.18}$$

where the integration is done over the volume V of a single electrode. The factor of 2 comes about since there are two identical electrodes. Using C.16 we find

$$P_e(t) = -\frac{\omega^2}{4} \frac{2V}{\sigma} \left(\vec{P}(\omega) \cdot \vec{P}(\omega) e^{i2\omega t} + c.c. - 2\vec{P}(\omega)^* \cdot \vec{P}(\omega) \right), \quad \text{C.19}$$

and again, we are only interested in the dc power denoted with brackets $\langle \rangle$:

$$\langle P_e \rangle = \frac{V\omega^2}{\sigma} \vec{P}(\omega)^* \cdot \vec{P}(\omega). \quad \text{C.20}$$

Finally, using equation C.17, we obtain the desired expression for the power dissipated as Joule heating in the electrodes:

$$\langle P_e \rangle = \sigma V \left[\frac{(3\varepsilon_0\omega/\sigma)^2}{1+(3\varepsilon_0\omega/\sigma)^2} \right] \left| \vec{E}_a' \right|^2 [\theta(\omega)]^2. \quad \text{C.21}$$

The oscillating ferroelectric dipole generates the time-dependent part of the applied field, which to first order in θ is

$$\vec{E}_a(\theta) \approx \frac{2\mu\theta}{4\pi\varepsilon_0 D^3} \hat{x}, \quad \text{C.22}$$

from which we find

$$\vec{E}_a' = \frac{2\mu}{4\pi\varepsilon_0 D^3} \hat{x}. \quad \text{C.23}$$

We compare these two sources of dissipation for the simulated device of Chapter 4, which comprised a 200 nm diameter by 400 nm tall PZT cylinder ($\mu = 4.4 \times 10^{-21}$ C·m) centered on a 1 micron long x 280 nm wide x 200 nm tall aluminum nitride beam. The resonance frequency of this mechanical resonator is 950.5 MHz and a Q of 10,000 is assumed. For a 1 degree angular amplitude of motion, the mechanically dissipated power is calculated from equation C.6 to be 42 nW. The electrodes are taken to be gold spheres ($\sigma = 3.6 \times 10^7$ ($\Omega \cdot \text{m}$)⁻¹) with a radius of 250 nm. The distance of closest approach of the PZT cylinder to each electrode is taken to be 50 nm, so that $D = 400$ nm. Again, for a 1 degree angular amplitude of motion at 950 MHz, using equations C.21 and C.23 we find the power dissipated as Joule heating to be 21 fW. For this example we see that the dissipation due to friction is 2×10^6 times larger than the Ohmic losses. Therefore we find that Ohmic losses are completely negligible for this design. Also, examining equations C.6 and C.21 we see that the power dissipated by each of these mechanisms scales as the square of the driven mechanical amplitude, making their ratio independent of the amplitude of mechanical motion.